# JOURNAL
# SCIENTIFIC | TECHNOLOGY | ENGINEERING

## Bilim  ⊕  Teknoloji  ⊕  Mühendislik

*https://dergipark.org.tr/tr/pub/jster*

**EDİTÖR NOTU** / *Editor Note*

Journal of Scientific, Technology and Engineering Research, mühendislik uygulamalarının tüm akademik ve teknoloji odaklı taraflara ulaştırılması amacına yönelik olarak yayınlanan dergi ilk yılını tamamlamış olup, web sayfası 78 farklı ülkeden araştırmacı tarafından ziyaret edilmiş ve yakın ilgiye mazhar olduğunu göstermiştir.

JSTER, yerli ve yabancı araştırmacılara, bilim, teknoloji ve mühendislik alanlarındaki çalışmalarını ve emeklerini göstermeleri açısından kendilerini ifade etme şansı veren bir platfom olmuştur.

Bilim, Teknoloji ve Mühendislik Araştırmaları Dergisi, hedeflediği misyonu doğrultusunda kalitesinden ödün vermeden yoluna devam etmeyi sürdürecektir. Kendisine, ileride uluslararası alanda atıf alan, makaleleri gözlenen bir akademik dergi olmayı hedeflediği bu mecrada siz yazarların ve okuyucuların desteği ile büyümeye devam edecektir.

*Journal of Scientific, Technology and Engineering Research has completed its first year published for the purpose of delivering engineering applications to all academic and technology-oriented parties, and its website has been visited by researchers from 78 different countries and has shown that it has attracted close attention.*

*JSTER has been a platform that gives local and foreign researchers the chance to express themselves in terms of showing their work and efforts in the fields of science, technology and engineering.*

*Journal of Science, Technology and Engineering Studies will continue on its way without compromising its quality in line with its mission. It will continue to grow with the support of you, the authors and readers, in this medium, where it aims to be a academic journal that will receive international references and watch its articles in the future.*

Dr. Mehmet BULUT

## Kapsam / *Scope*

Dergide yayımlanan makaleler, izin alınmaksızın hiçbir şekilde başka bir yerde yayımlanamaz veya konferans, seminer, kongre gibi yerlerde bildiri olarak sunulamaz. Makalelerin bir kısmı veya tamamı, ancak dergimiz kaynak gösterilerek kullanılabilir.
*Articles published in the journal may not be published elsewhere without permission or can not be presented as a paper in conferences, seminars, congresses. Some or all of the articles can only be used by citing our journal.*

## Yayın Dili / *Publishing Language*

Dergide yayınlanacak makalelerin yayın dili olarak, Türkçe ve İngilizce dillerinde yazılmış makaleleri yayınlamaktadır.
*As the publication language of the articles published in the journal, it publishes articles written in Turkish and English.*

Umut olmadan, umulmayanı bulamayız.
**Roger Garaudy**

# İÇİNDEKİLER / *CONTENTS*

***Araştırma Makalesi*** / Research Article

RESEARCH ARTICLE

# Structural Analysis of Metallic Pressure Vessels With Weld Sinkage in the Circumferential Joint

*Chitaranjan PANY

Structural Engineering Entity, VSSC, Thiruvananthapuram, Kerala, INDIA
c_pany@yahoo.com, Orcid.org/0000-0001-8617-2134

## HIGHLIGHTS

- *Weld sinkage type discontinuity is considered here which is occured during fabrication process of pressure vessel. Literatures on the study area are not many and have importance in design of pressure vessel to various engineering field.*
- *Non-linear( geometric and material) FEA carried out in this article.*
- *The stress concetration factor due to cir-seam weld sinkage is reported.*
- *Unintentionally discontinuity stress introduced during fabrication/manufacturing process is studied.*

## Keywords:

- Circumferential joint,
- Finite element analysis,
- Nonlinear analysis,
- Pressure vessels,
- Weld sinkage

## *Correspondence:

Chitaranjan PANY
c_pany@yahoo.com

## GRAPHICAL ABSTRACT

*The presence of weld sinkage in cir-seam joint of pressure vessels (cylindrical and spherical) has been investigated in this work. The discontinuity considered here is named as weld sinkage. The corresponding discontinuity stress introduced during fabrication process is analysed. Here only geometric aspects are being considered and the discontinuities are assumed to be free of residual stress. Non-linear finite element analysis (NL-FEA) performed. The vessel material of HSLA 15CDV6 is considered. Graphically the deformations and stress distributions( meridional, hoop and effective) along axial distance are shown. The effective (von-Mises) stress is found at sinkage location around 2 and 4 times higher than nominal stress ( stress away from weld sinkage location) for cylindrical and spherical vessel respectively.The results are shown in Figure A.*
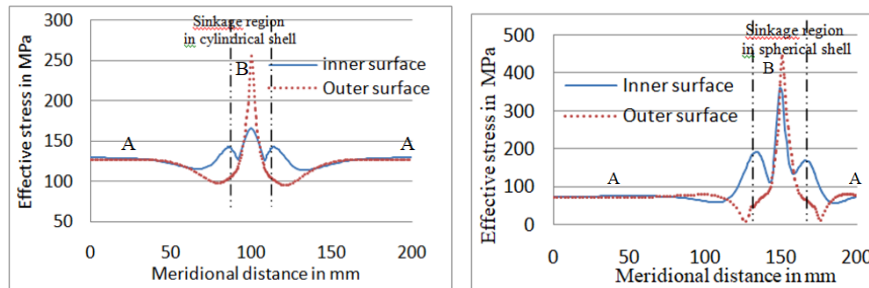
**Figure A.** The Effective stress distribution in (a) cylindrical and, (b) spherical shell

**Aim of Article :***To find the stress concentration factor due to discontinuity stress at weld sinkage location of a pressure vessel.*

**Theory and Methodology :** *The Non-linear (both material and geometric) finite element method has been used to study the problem.*

**Findings and Results:** *Results show that the stress concentartion factor is 2 to 4 times for cylindrical and sperical vessel at sinkage location as compared ti nominal stress region( away from discontinuity region).*

**Conclusion :** *NL-FEA (geometric and material) has been attempted in this work to predict the actual structural behavior of pressure vessel (cylindrical and spherical) segments of equal thickness in presence of sinkage type mismatch in the circumferential weld joint. The effective (von-Mises) stress is found at sinkage location approximately 2 and 4 times higher than nominal stress( stress away from sinkage location) for cylindrical and spherical pressure vessel respectively. This study ( weld sinkage) is having importance to pressure vessel design which is common in aerospace, mechanical and chemical engineering sector, which is occurred from manufacturing process. However, these results (stress concentration factor) will be further verified through different thickness of pressure vessel segments with different sinkage radius and its occurrence at cir-seam and long-seam location from fabrication process of pressure vessel. This work can be extended to find the burst pressure of pressure vessel in presence of weld sinkage to find its capacity.*

RESEARCH ARTICLE

# Structural Analysis of Metallic Pressure Vessels With Weld Sinkage in the Circumferential Joint

*ⓘD Chitaranjan PANY

Structural Engineering Entity, VSSC, Thiruvananthapuram, Kerala, INDIA
c_pany@yahoo.com, Orcid.org/0000-0001-8617-2134

## HIGHLIGHTS

- *Weld sinkage type discontinuity is considered here which is occured during fabrication process of pressure vessel.Literatures on the study area are not many and have importance in design of pressure vessel to various engineering field.*
- *Non-linear( geometric and material) finite element analysis carried out in this article*
- *The stress concentration factor due to cir-seam weld sinkage in pressure vessel is reported.*
- *Unintentionally discontinuity stress introduced during fabrication/manufacturing process is studied. The obtained results are important in design of pressure vessel with application to aerospace and chemical industry.*

**ABSTRACT**

*The presence of weld sinkage in cir-seam joint of pressure vessels (cylindrical and spherical) has been investigated in this work. The discontinuity considered here is named as weld sinkage. The corresponding discontinuity stress introduced during fabrication process is analysed. Here only geometric aspects are being considered and the discontinuities are assumed to be free of residual stress. Non-linear finite element analysis (NL-FEA) performed. The vessel material of HSLA 15CDV6 is considered. Graphically the deformations and stress distributions( meridional, hoop and effective) along axial distance are shown. The effective (von-Mises) stress is found at sinkage location around 2 and 4 times higher than nominal stress( stress away from sinkage location) for cylindrical and spherical vessel respectively.*

**Keywords:** *Circumferential joint, Finite element analysis, Nonlinear analysis, Pressure vessels, Weld sinkage*

## I.  INTRODUCTION

In the aerospace, nuclear power, oil, chemical, and many other industries pressure vessels are widely used. In fabrication, various segments are joined together by welds or some other means to form complete pressure vessels. Certain regions of pressure vessels were exist, where structural continuity cannot be satisfied by the membrane forces alone. Such regions are called as discontinuity regions. The stress associated in these region is termed as discontinuity stress. Presence of discontinuities in thickness, radius and slope in the manufactured product causes additional bending stress. In the discontinuity region the stress distribution may change. It is desirable to reduce the number and magnitude of discontinuity to a minimum. In the context of effects of distortion at welded joints, the distortions considered are mismatch [1-8], weld sinkage [9] (peaking or angular mismatch), slope discontinuities and out of roundness in pressure vessels. Literature studies show that there is very limited work available. In the present work, to predict the structural behavior of pressure vessel segments of equal thickness with weld sinkage type discontinuity is considered and corresponding

discontinuity stress introduced during fabrication process is analysed. Further, here only geometric aspects are being studied and the discontinuities are assumed to be free of residual stress. NL-FEA[10] is carried out to model the pressure vessel with presence of sinkage type weld mismatch. The stress concentration factor due to weld sinkage is reported. These results are very much useful as a design guide lines for researchers and design engineers working in pressure vessel fields.

## II. WELD SINKAGE[9] (ANGULAR DISTORTION)

Weld sinkage [9] is the term used to describe the meridional slope discontinuity of the general shape. This is symmetric, around the circumference of the shell and also with respect to its lowest point. This type of discontinuity is frequently occurring during welding. The geometric aspect of the discontinuity is considered here and shown in Fig.1.The shell is considered stress free before the application of the first pressure loading. A cylinder subject to peaking distortion at the welded joint could be treated as a special case of a noncircular cylinder(Fig.1).
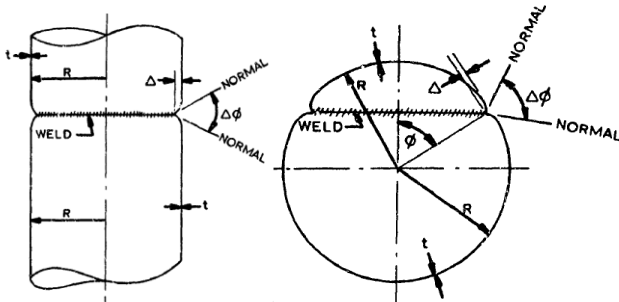


**Figure 1**. Typical weld sinkage in cylinder and sphere[9]

The main geometry parameters of sinkage [9] are sinkage length (L), sinkage depth (Δ) and angular change (Δφ) and shown in Fig. 2.
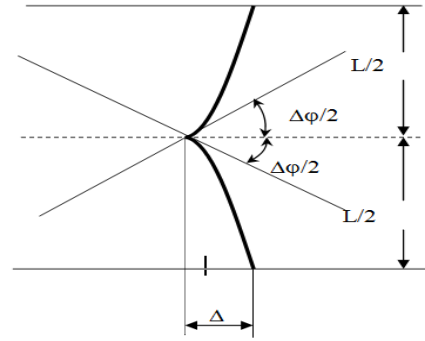


**Figure 2.** Sinkage geometry parameters

The two other parameters considered for the weld sinkage [9]are pressure nonlinearity parameter (ρ) and geometry factor (μ) and given in equ.(1) and equ.(2) respectively. The parameter is related to the structural geometry only as follows.

$$\mu = \frac{0.55}{\Delta}\sin\left(\frac{\Delta\emptyset}{2}\right)\sqrt{Rt} \tag{1}$$

$$\rho = \frac{P}{\frac{2}{\sqrt{3(1-\upsilon^2)}}E\left(\frac{t}{R}\right)^2} \tag{2}$$

## III. FINITE ELEMENT ANALYSIS

NL-FEA (material and geometric) has been carried out[3,4] on pressure vessels(cylindrical and spherical) having weld sinkage[9] in the cir-seam (circumferential direction) joint as shown in the Figure 3. R is the radius of cylinder and sphere. t is the thickness of shell. $R_T$ is the sinkage radius or toroidal meridional radius. The geometric details of the vessels used are given in Table I and Table II.

An axi-symmetric model with PLANE 42 element of Ansys[10] is used for FE idealization. The convergences of the results were verified by analyzing the models with different mesh density.

The material used for the vessel is HSLA 15CDV6 [3,4] having Young's modulus (E) 206010 MPa, Poisson's ratio of 0.3,yield strength 834 MPa and ultimate strength 0f 981 MPa.

Internal pressure is estimated by considering the pressure nonlinearity parameter as 0.05[9]. The length of vessel is considered here such that the discontinuity stress disappears and the membrane stress exists away from the junction (i.e. sinkage location). Further the stress away from discontinuity region becomes nominal stress (hoop=PR/t; meridional PR/2t for

cylindrical shell and hoop=meridional stress = PR/2t for spherical shell)[11].
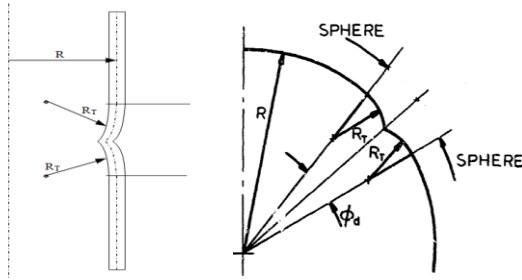


**Figure 3.** Geometry of cylindrical and spherical pressure vessel having weld sinkage[9]

The boundary conditions are applied on the shell as follows. One end of the longitudinal edge of cylindrical shell vessel is constrained in the axial direction to avoid rigid body motion and at the other edge end force corresponding to closed end condition is applied as a pressure load [3].

In spherical pressure vessel symmetric boundary conditions are applied at symmetry plane. The loading in vessel is internal pressure load which is applied on inner surface. NL-FEA (material and geometric) is performed.

**Table I**. Geometric detail of cylindrical pressure vessels having weld sinkage[9]

| $t_a/t_b$ | R | t | L | Δ | Δφ | ρ | μ |
|---|---|---|---|---|---|---|---|
| 1 | 216 | 2.5 | 30 | 1.626 | 24.7 | 0.05 | 1.68 |

**Table II**. Geometric detail of spherical pressure vessel having weld sinkage

| $t_a/t_b$ | R | t | L | Δ | Δφ | ρ | μ |
|---|---|---|---|---|---|---|---|
| 1 | 216 | 2.5 | 17.2 | 8.0 | 55.2 | 0.05 | 0.74 |



(a)  Cylindrical
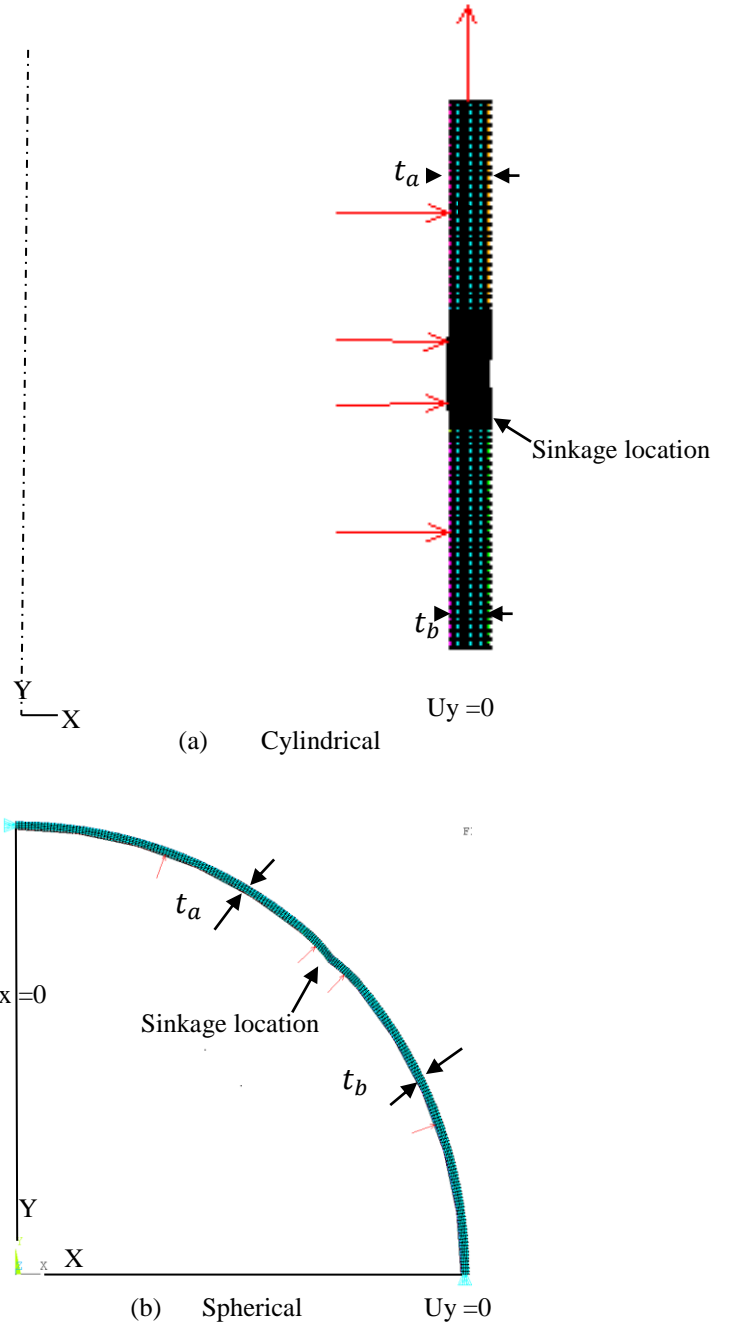


(b)  Spherical

**Figure 4.** Finite element model showing weld sinkage in (a) cylindrical and (b) spherical vessel at cir-seam joint

## III. RESULT AND DISCUSSIONS

Stress distributions and deformations were plotted along axial distance for both vessels with sinkage at cir-seam joint. Figures 5 and 6 show the distribution of meridional stress, hoop stress and effective stress in a cylindrical vessel. The stress distributions are found to be symmetric with peaks at the weld. The discontinuity stresses are diminishes and membrane

stress exists away from the joint. The deformations in axial and radial direction are also given for cylindrical pressure vessels in Figure 7.

## A. *Cylindrical Pressure Vessel*
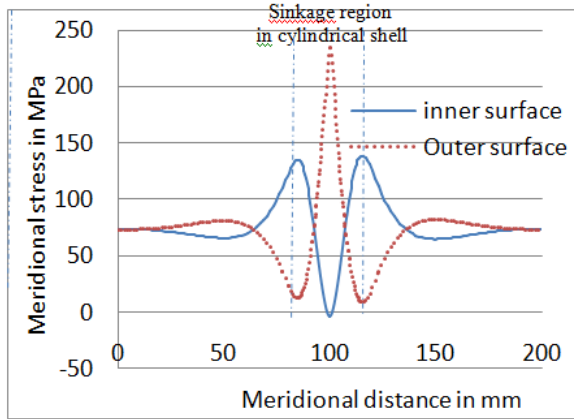


(a)
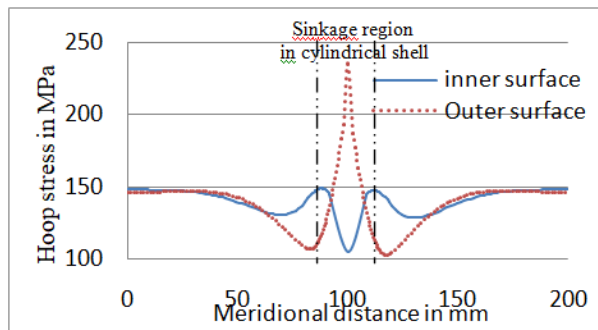


(b)

**Figure 5.**(a) Meridional stress and (b) Hoop stress distribution for cylindrical pressure vessel
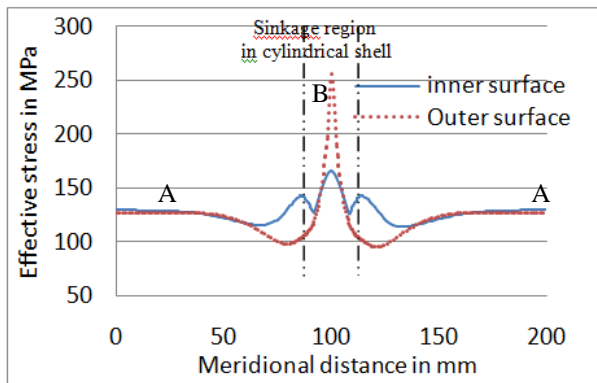


**Figure 6.** Effective stress distribution for cylindrical pressure vessel
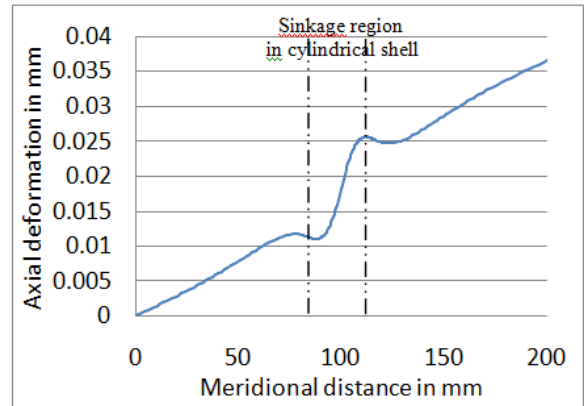


(a)
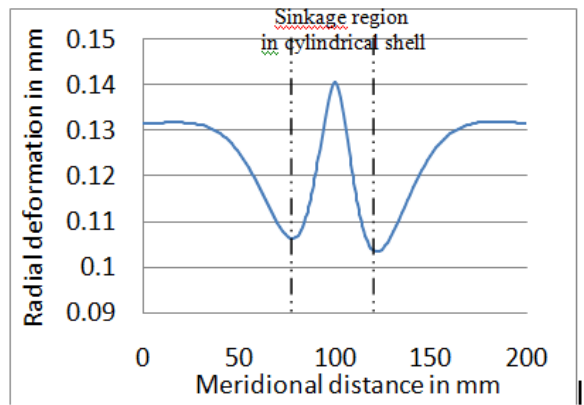


(b)

**Figure 7.**(a) Axial and (b) radial deformations of cylindrical pressure vessel

## B. *Spherical Pressure Vessel*
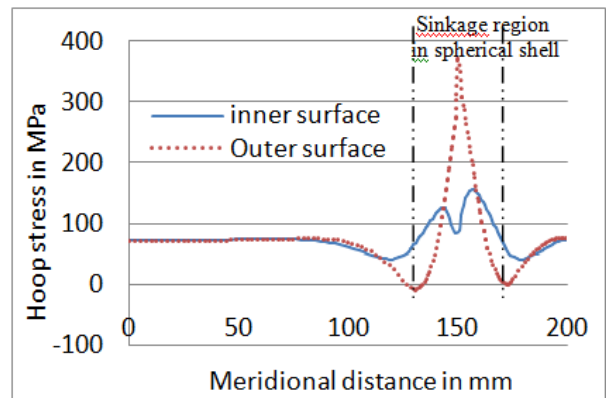


(a)
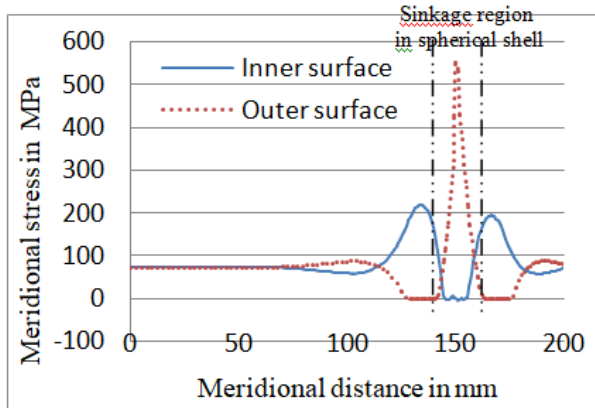
(b)

**Figure 8.**(a) Hoop and  (b) Meridional stress distribution for spherical vessel

Figures 8-9 give the meridional, hoop, effective stress distributions at the joint of spherical pressure vessel having sinkage. It is seen from that stress distribution curves of similar trend as that of the cylindrical vessel. The peak effective stress at sinkage location (B) is around 2 times of nominal stress region (A) in cylindrical shell is found as shown in Figure 6.
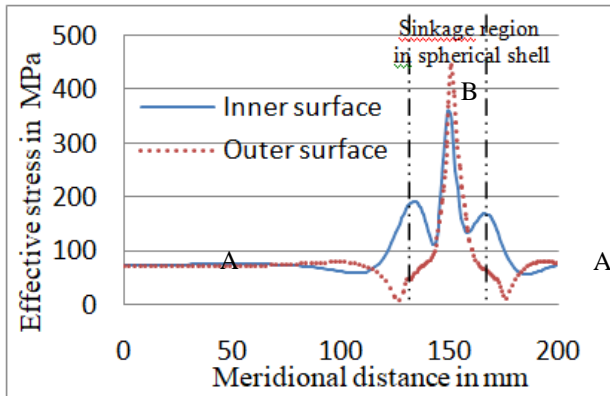


**Figure 9.** Effective stress distribution in spherical shell
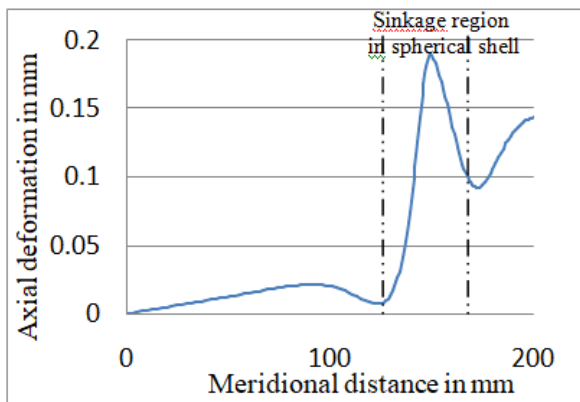


**Figure 10.** Axial deformation distribution for spherical shell

The peak effective stress at sinkage location (B) is approximately 4 times of nominal stress region (A) in spherical shell is found as shown in Figure 9. The axial deformation is shown in Figure 10.

## IV. CONCLUSION

NL-FEA (geometric and material) has been attempted in this work to predict the actual structural behavior of pressure vessel (cylindrical and spherical) segments of equal thickness in presence of sinkage type mismatch in the circumferential weld joint. This type of weld sinkage is unexpectedly occurred from fabrication process. Non-linear finite element results were verified by analyzing the models with different mesh density through the convergences study. The location of the peak stress is found through FEA and found the effective stress at sinkage location is 2 and 4 times approximately higher than nominal stress for cylindrical and spherical shell respectively. The trend of stress distribution along the axial distance of spherical pressure vessel is similar to that of cylindrical pressure vessel. The discontinuity stresses are found to be symmetric on either side of the weld sinkage joint of both vessel (cylindrical and spherical).

However, these results (stress concentration factor ) will be further verified through different thickness of pressure vessel segments with different sinkage radius and its occurrence in cir-seam and long-seam location from fabrication process of pressure vessel. This work can be extended to find the burst pressure of pressure vessel in presence of weld sinkage to find its capacity.

### REFERENCES

[1] P.T. Bizon, "Elastic stresses at a mismatched circumferential joint in a pressurized cylinder including thickness changes and meridional load coupling," Lewis Research Center, Cleveland, Ohio, USA, Technical Note TN-D-3609 (1-45), 1966.

[2] A. Subhananda Rao, G. Venkata Rao and B. Nageswara Rao, "Effect of long seam mismatch on the burst pressure of maraging steel rocket motor case," *Eng. Fail. Anal.*, vol. 12, pp. 325-336, 2005.

[3] Sreelakshmi MG, C.Pany, "Stress analysis of metallic pressure vessels with circumferential mismatch using finite element method," *Int. J. of Sci. and Eng.Res.*,vol.7(4),pp.479-484,2016.

[4] C.Pany, M.K. Sundaresan, B. Nageswara Rao,B. Sivasubramonian, and N. Jayachandran Nair, "On the bursting of an HSLA steel rocket motor case duringproof pressure testing," *Steel Grips (J. of Steel and related Mater.) App.*, vol. 10, pp. 434-438, 2012.

[5] T. AseerBrabin, T. Christopher and B. Nageswara Rao, "Finite element analysis of cylindrical pressure vessels having a misalignment in a circumferential joint," *Int. J. of Press. Vessels and pip.*, vol. 87, pp. 197-201, 2010.

[6] R.H. Johns and T.W.Orange, "Theoretical elastic stress distributions arising from discontinuities and edge loads in several shell-type structures," Lewis Research Center, Cleveland, Ohio, USA, Technical Report TR-R-103 (1-34), 1961.

[7] W.C. Morgan and P.T. Bizon, "Comparison of experimental and theoretical stresses at a mismatch in a circumferential joint in a cylindrical pressure vessel," Lewis Research Center, Cleveland, Ohio, USA, Technical Note TN-D-3608 (1-17), 1966.

[8] C. R Steele and J Skogh, "Slope discontinuities in pressure vessels", J. of app. Mech., 37(3) pp. 587-598, 1970. https://doi.org/10.1115/1.3408584

[9] J. Skoghand A.M.C. Holmes, "Elastic and plastic stresses at weld sinkages and other discontinuities in pressure vessels," Palo Alto research laboratory,palo Alto, California, LMSC-4-05-69-7, Oct. 1969.

[10] Ansys 13.0, Ansys Manual, ANSYS In.

[11] John F. Harvey."Theory and design of pressure vessels",Van Nostrand Reinhold Company Inc. New York,USA:ISBN No. 0-442-23248-9,1985.

RESEARCH ARTICLE

# A Mobile Robot Application for Constructing Semantic and Metric Maps of Search and Rescue Arenas with Point-Based Deep Learning

[1] Muhammed KOCAOĞLU, [2] Yunus Emre IŞIKDEMİR, [3] Muhammed Ali UZUN, [4] Kaya TURGUT

[5] Muhammed OĞUZ TAŞ, and [6,*] Burak KALECİ

[1,2,3,4,5,6] Eskisehir Osmangazi University, Electrical and Electronics Engineering, Eskisehir, Turkey.

[6] burakaleci@gmail.com, 0000-0002-2001-3381
[1] mdkocaoglu@gmail.com, 0000-0003-0956-1210
[2] yemreisikdemir@gmail.com, 0000-0001-7022-2854
[3] mdaliuzun@gmail.com, 0000-0002-2679-3980
[4] kayaturgut@hotmail.com, 0000-0003-3345-9339
[5] motas@ogu.edu.tr, 0000-0001-5689-8786

## HIGHLIGHTS

- *The semantic and metric maps are generated that first-responders can easily read in post-disaster indoor environments.*
- *A point-based deep learning architecture is employed to produce the semantic map.*
- *Octree-based 3D metric map composes voxels not only occupied and free but also walls, terrain, and ramps.*
- *The experimental results show that the proposed method can produce accurate maps.*

## Keywords :

- Search and Rescue,
- Mobile Robot,
- 3D Semantic Map,
- 3D Metric Map,
- Point Cloud,
- Point-Based Deep Learning

## Article Info :

**\*Correspondence:**

Burak KALECİ,
burakaleci@gmail.com,
+90 555 7375966.

## GRAPHICAL ABSTRACT

This study aims to create semantic and metric maps of a post-disaster indoor environment similar to standard the National Institute of Standards and Technology (NIST) search and rescue test arenas that first-responders can easily read. We prefer to use point cloud data acquired with an RGB-D camera since it does not be affected by post-disaster environments' dusty and dull nature. Besides, each point cloud data is processed separately so that the semantic and metric maps grow incrementally. The Dynamic Graph Convolutional Neural Network (DGCNN) is used to classify points as sematic categories such as walls, terrain, and inclined and straight ramps. RTAB-Map and the semantic map are utilized to generate the octree-based 3D metric map. The experiments are conducted in a simulated environment modelled with Gazebo similar to NIST test arenas to show the effectiveness of the proposed method.
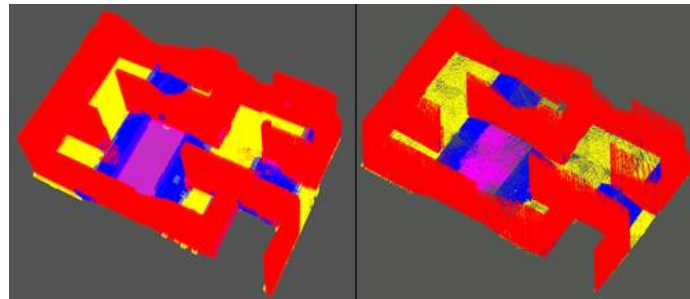
**Figure A.** The metric(left) and semantic(right) maps of the environment

**Aim of Article:** *This study aims to construct semantic and metric maps of a search and rescue test arena with a mobile robot.*

**Theory and Methodology:** *The point cloud data is used to generate semantic and metric maps. DGCNN architecture is applied to determine the semantic class of points. The RTAB-Map and semantic map are utilized to generate an octree-based 3D metric map.*

**Findings and Results:** *Figure A shows our experimental results. As seen from the figure, the proposed method produced accurate semantic and metric maps.*

**Conclusion :** *The proposed method process each point cloud data separately and grows the semantic and metric maps incrementally so that it decreases computational complexity.*

RESEARCH ARTICLE / ARAŞTIRMA MAKALESİ

# Arama Kurtarma Alanlarında Metrik ve Anlamsal Harita Üretmek için Nokta Tabanlı Derin Öğrenme ile Bir Gezgin Robot Uygulaması

[1] Muhammed KOCAOĞLU, [2] Yunus Emre IŞIKDEMİR, [3] Muhammed Ali UZUN, [4] Kaya TURGUT, [5] Muhammed OĞUZ TAŞ, [*] Burak KALECİ

[1,2,3,4,5,6] Eskişehir Osmangazi Üniversitesi, Elektrik-Elektronik Mühendisliği, Eskişehir, Turkiye.
[6] burakaleci@gmail.com, 0000-0002-2001-3381
[1] mdkocaoglu@gmail.com, 0000-0003-0956-1210
[2] yemreisikdemir@gmail.com, 0000-0001-7022-2854
[3] mdaliuzun@gmail.com, 0000-0002-2679-3980
[4] kayaturgut@hotmail.com, 0000-0003-3345-9339
[5] motas@ogu.edu.tr, 0000-0001-5689-8786

## HIGHLIGHTS / ÖNE ÇIKANLAR

- *Afet sonrası bina içi ortamlarda ilk yardım ekiplerinin kolaylıkla kullanabileceği anlamsal ve metik harita üretilmiştir.*
- *Anlamsal haritanın çıkarılması için nokta tabanlı derin öğrenme mimarisinden faydalanılmıştır.*
- *8-li ağaç yapısında 3B metrik haritada sadece dolu ve boş vokseller değil duvar, zemin ve rampalara ait olan vokseller de yer almaktadır.*
- *Test sonuçları önerilen yöntemin doğruluğu yüksek haritalar üretebileceğini göstermiştir.*

## Article Info / Makale Bilgi

## ABSTRACT / ÖZET

Bina içi ortamlarda zehirli madde yayılımı, sel, yangın ve deprem gibi afetlerden sonra robotlar kullanılarak arama ve kurtarma yapılmasına yönelik çalışmalar son yıllarda hız kazanmıştır. Bu çalışmanın ana motivasyonu, ilk yardım ekiplerinin kolaylıkla kullanabileceği afet sonrası bina içi ortamın metrik ve anlamsal haritalarını oluşturmaktır. Bu çalışmada, afet ortamında karşılaşılabilecek toz, duman ve yetersiz ışıklandırma gibi faktörlerden etkilenmeyen ve nesnelerin geometrik yapısını yüksek doğrulukta temsil edebilen nokta bulutu verilerinin kullanılmasına karar verilmiştir. Her bir adımda alınan nokta bulutu ayrı ayrı işlenerek önerilen yöntemin hesaplama karmaşıklığının düşürülmesi amaçlanmıştır. Anlamsal haritanın üretilmesi aşamasında geçmiş çalışmalardan farklı olarak nokta tabanlı derin öğrenme mimarisi DGCNN kullanılmıştır. Böylece nokta bulutunda yer alan her noktanın anlamsal sınıfı (duvar, zemin, eğimli ve düz rampa) belirlenmiştir. 3B metrik haritanın oluşturulması için RTAB-Map ve anlamsal harita birlikte kullanılarak 8-li ağaç yapısında bir gösterim elde edilmiştir. Bu haritada önceki çalışmalardan farklı olarak sadece dolu ve boş vokseller değil, aynı zamanda duvar, zemin ve rampa sınıflarına ait olan vokseller de yer almaktadır. Önerilen yöntemin test edilmesi için Gazebo benzetim ortamında NIST ortamlarına benzer bir test alanı modellenmiş ve bir Pionner 3-AT gezgin robot teleoperasyon yöntemi ile gezdirilmiştir. Test sonuçları önerilen yöntemin başarılı bir şekilde anlamsal ve metrik harita üretebildiğini göstermiştir.

**Anahtar Kelimeler:** *Arama ve Kurtarma, Gezgin Robot, 3B Anlamsal Harita, 3B Metrik Harita, Nokta Bulutu, Nokta Tabanlı Derin Öğrenme*

# I. INTRODUCTION

After disasters such as fire, earthquakes, floods, and toxic substances, post-disaster indoor environments could be hazardous for search and rescue teams that include humans and animals. The main risks in these environments are the possibility of spreading dangerous matters and collapsing due to the structural breaking down. For these reasons, the studies that addressed search and rescue tasks exploiting robots in these environments have been gained popularity. Although using robots in search and rescue tasks could appear an appropriate solution to avoid risks for humans and animals, post-disaster environments would be challenging even for robots to achieve the tasks they are expected to perform. The primary difficulties in post-disaster environments that the robot must cope with are uneven terrain and poorly lightened circumstances due to these environments' dusty and dull nature. To deal with these challenges, the robots that operate in post-disaster environments must have advanced capabilities such as interpreting raw data, producing semantic information, and being aware of circumstances. Thanks to the improvements in perception technologies and corresponding algorithms and software, robots approach to reach these abilities. However, it is necessary to observe steadily positive and negative aspects of improved methods for giving direction to future works. Unfortunately, the researchers generally may not have the opportunity to test their works since post-disaster indoor environments are rarely faced, and building these environments is complicated and expensive. In order to overcome that problem, DARPA and RoboCup organizations regularly constituted competitions for search and rescue missions.

The RoboCup rescue competitions have been conducted since 2001. The main goal of these competitions is to increase the performance of the robots in search and rescue missions. After the first competition, Kitano and Tadokoro [1] revealed challenges about these missions and introduced the first standards and evaluation metrics. Then, Jacoff et al. proposed reference test arenas for autonomous mobile robots developed by NIST [2]. An example reference test arena is shown in Fig. 1. Also, they defined objective performance evaluation criteria such as the number of locating victims and producing accurate maps that first-responders can easily read. In 2006, the RoboCup rescue competitions were separated into two categories: Agent and the virtual robot competitions. While the agent competitions aimed to coordinate multi-agents systems that include police officers, firefighters, and first-responders to handle

disasters in urban scenarios, virtual robot competitions focused on navigation, mapping, and victim detection [3]. After the first virtual robot competition, Balakirsky et al. [4] assessed the performance of the participant teams under specific standards and criteria. In order to evaluate the maps, they used metrics such as attributions that indicate crucial points such as victims and obstacles, accuracy, skeleton and metric quality, and utility that provides cleared regions, locations that the victims are trapped for first responders. The participant teams generally preferred to generate topological maps with 2D lasers. Over the years, the researchers developed new methods to improve the mapping capabilities of the robots. For example, in 2009, teams preferred to use image processing approaches to produce the environments' metric map [5]. These improvements promoted the administration of the competitions to introduce more challenging environments for robots. In 2010, active elements such as smoke, elevator, and the ferry was integrated into the environments. The champion team at RoboCup 2012 used the simultaneous localization and mapping (SLAM) approach to generate geometric map of the environment. The SLAM approach segmented the laser scans into lines depending on the distance between successive points. Besides, the produced line segments were used to construct a semantic map that separates the environment into spaces such as small rooms, large rooms, and corridors divided by doorways. This was the first attempt to construct semantic maps in the search and rescue domain [6]. Sheh et al. [7] overviewed the 16 years of Robocup rescue competitions. The authors emphasized the robots' progress in terms of mobility, autonomy, perception, and adaptation to inhospitable environments such as poor lighting and piles of rubbles. Then, they announced novelties in the competition for the coming years. Probably, the most important one was using Robot Operating System (ROS) together with Gazebo simulation environment. ROS [8] is a commonly used framework to perform robotic applications. It contains libraries (in other words, packages) for a variety of purposes, from mapping to manipulation of a robot arm. ROS generally operates with Gazebo [9] simulation environment, which provides high-performance physics engines and 2D/3D sensors.

**Figure. 1.** An example reference test arena [5].

After ROS and Gazebo's introducing, participants of the virtual robot competition began to use ROS packages together with Gazebo. For example, in 2017, Chukyo Rescue A Team [10] employed GMapping [11] and Hector SLAM [12] packages for mapping. GMapping [11] is a well-known mapping approach since it was introduced because it could be employed in both indoor and outdoor applications. The main advantage of that method is the ability to create accurate maps with low computational complexity. However, GMapping approach accepts raw 2D laser range data and odometry to generate a 2D occupancy grid map. Similarly, the Hector SLAM [12] approach was applied to produce 2D metric maps. The Hector SLAM's positive aspects are it does not need to use odometry data and has a high update rate. YILDIZ Team [13] utilized Octomap [14] to describe 3D environments. OctoMap was proposed to build a representation (in other words, map) of 3D environments based on octree data structure [14]. First, the data is represented with only one voxel that contains all points. Then, it splits into eight voxels of the same size. The process is repeated until the predefined depth, or voxel size is accomplished. The main contribution of OctoMap representations is using a probabilistic occupancy estimation approach to determine free, occupied, and even unknown voxels. Besides, OctoMap is a memory-efficient representation when it is compared to previous approaches. However, the computational complexity of OctoMap is not appropriate to produce fine-detailed maps. For example, as the voxel size decreases, especially less than 0.05 meters, to describe details of scenes, OctoMap requires significant durations for generating maps. Also, it does not take into account the semantic clues of the scenes. In 2018, SOS RS Team [15] exploited FastSLAM algorithm [16] for mapping. FastSLAM algorithm uses the 2D laser range data as input and generates the geometric map of the

environment. This algorithm decreases computational complexity of SLAM approaches significantly. In the same year, AutonOHM Team [17] employed one of the ROS packages, which is called ohm_tsd_slam [18] to generate a 2D map of the environment. The main advantage of this package is to integrate data gathered by RGB-D cameras and 2D/3D laser range finders within the same representation. Similar to the OctoMap approach, ohm_tsd_slam package cannot interpret the scenes in terms of semantic information. In 2019, ATR Team [19] utilized Real-Time Appearance-Based Mapping (RTAB-Map) [20] to create a 2D occupancy grid of the rescue environment. Besides, RTAB-Map also provides 3D point cloud data. RTAB-Map ROS package is integrated with OctoMap so that it can generate the voxel representation of the environment and separate voxels as occupied, free, and unknown [21]. Besides, RTAB-Map contains many feature extractor algorithms such as SIFT, SURF, BRIEF, FAST etc. to recognize some objects such as walls, terrain, and other everyday objects from the visual data. Therefore, it can produce semantic information. Unfortunately, RTAB-Map cannot identify ramps that placed NIST's test arenas since it did not design for search and rescue missions.

As mentioned above, the participant teams of virtual robot competitions generally focused on mapping approaches that generate metric, topologic, and geometric maps. Extracting semantic information or producing semantic maps were considered from only a few teams. However, some previous studies that interested in the semantic classification of walls, terrain, and ramps were proposed. These studies are generally cast into two groups. In the first group, the well-known segmentation methods such as region growing [22] and RANSAC [23] are applied to obtain planar surfaces. Region growing uses a predetermined number of neighbors or search radius to determine the points that belong to the same planar surface. Therefore, it may not be appropriate for real-time applications due to its high computational complexity. On the other hand, RANSAC is a fast and accurate segmentation method aiming to determine a mathematical model for planes. However, it can clusters points that have a similar mathematical model into a plane. This could be problematic since RANSAC does not take into account the neighboring relationship. After planar surfaces are specified, segmented planes are classified depending on geometric features of planes such as normals of points. In the second group, learning approaches are employed for semantic segmentation. These studies generally prefer to apply the Convolutional Neural Networks (CNN) approach to visual data. A recent study proposed by Deng et al. [24] uses CNN to

determine point-wise semantic labels with RGB and depth images in NIST test arenas. On the other hand, Turgut and Kaleci [25] concentrated on directly using point cloud data instead of visual data. For that reason, they examined point-based deep learning architectures and they made a comprehensive comparison for PointNet [26], PointNet++ [27], PointCNN [28], and DGCNN [29] architectures that are classified walls, terrain, and ramps in a simulated environment similar to NIST test arenas.

In this study, we aim to produce the 3D metric and semantic maps of a simulated environment similar to NIST reference test arenas with a mobile robot. In this way, we can provide an accurate semantic map, which describes walls, terrain, and ramps, that first-responders can easily read. It is important to note that generating accurate maps is one of the crucial evaluation criteria in virtual robot competitions because an accurate map can significantly decrease searching victim duration and protect first-responders from accidents. Besides, producing a semantic map can contribute robot's autonomous navigation capability. For example, the robot can navigate more reliable by adjusting its velocity when it knows the slope of a ramp. Also, the robot can generate suitable waypoints while traversing ramps to keep its balance. In fact, the robot can consider ramps to enhance its path plan.

The previous studies that address the semantic classification of walls, terrain, and ramps are rare, and they used generally visual and 2D range data. However, the visual data may not be appropriate for dusty, dull, and poorly lightened post-disaster environments. On the other hand, 2D range data cannot be affected by these situations. Nevertheless, its capability to describe the 3D characteristics of the scene is insufficient. At that point, using point cloud data can be a favorable solution to cope with the drawbacks of visual and 2D range data. Therefore, we placed an RGB-D camera on a P3-AT robot and utilized RTAB-Map ROS package to gather point cloud data of a scene. One of the contributions of this study is processing a single scene, which is captured after each predetermined time interval while the robot navigates in the environment by teleoperation. In this way, the semantic and metric maps grow step-by-step, and the computational complexity of the proposed method is decreased. The second contribution is applying a point-based deep learning architecture DGCNN, which receives a single scene and determines point-wise semantic classes, instead of using visual data. The weight of DGNN model generated by Turgut and Kaleci [25] with data acquired in a different simulated environment is used to classify each point. The last contribution is

creating a 3D metric map that the robot needs to navigate. Apart from the previous studies, we utilize RTAB-Map and the semantic map while producing the octree-based 3D metric map. In the map, each voxel has a semantic label so that robot can plan its path more reliable.

The rest of the paper is organized as follows: In Section 2, the proposed method is explained in detail. The experimental setup and experiments are presented in Section 3. The conclusion and future works are given in Section 4.

## II. METHOD

The proposed method consists of three stages. In the first stage, RTAB-Map is employed to gather point cloud data. Besides, we made some modifications to obtain point cloud data for each scene. In the second stage, we construct a semantic map of each separate scene with the aid of point-based deep learning architecture DGCNN. Then, we merge the current map with the global semantic map. Lastly, similar to the semantic map, we build a metric map (in other words, octree map) of the current scene and merge it with the previously generated metric map. In this stage, we obtain free and occupied voxels from RTAB-Map, and then we utilize the semantic map to classify voxels in terms of wall, terrain, inclined and straight ramps.

### A. Gathering Point Cloud Data

We used the RTAB-Map ROS package to gather point cloud data. RTAB-Map receives raw point cloud data acquired with the RGB-D sensor of the robot (Fig. 2(a)). It is important to note that the raw point cloud data is obtained according to the robot's local coordinate system (Fig. 2(b)). Hence, RTAB-Map automatically transforms the raw point cloud data into the global coordinate system of Gazebo simulation environment with the aid of the robot's position and orientation. Then, RTAB-Map applies the voxel filter depending on the GridCellSize parameter to downsample the transformed point cloud data (Fig. 2(c)). In this way, computational complexity decreases because the number of samples is reduced without losing the general characteristics of the data. Another crucial issue about the gathering point cloud data is that RTAB-Map accumulates point cloud data during the map producing process as a default property. After this process is completed, it reveals an entire map of the environment. However, this default property is not appropriate for constructing the semantic and metric maps of a search and rescue environment. The main

| (a) | (b) | (c) |
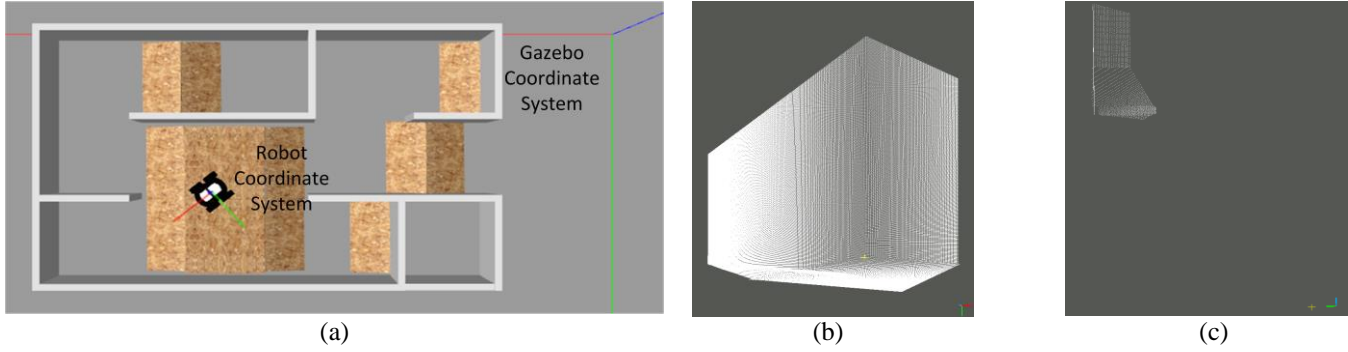
**Figure. 2.** Gathering point cloud data. (a) The red, green, and blue lines at the upper-right corner of the image indicate Gazebo's global coordinate system. The same colored lines on the robot show robot's local coordinate system. (b) The raw point cloud data according to the robot's local coordinate system. (c) The downsampled point cloud data according to the Gazebo's global coordinate system.

reason for that is decreasing computational complexity while processing point cloud data separately for each scene. In order to achieve this, we adjusted the MaxNodes parameter.

### B. Constructing Semantic Map

After we obtain point cloud data for a scene, the duplicated points are removed from the point cloud data to diminish the computational complexity of the approach. Then, the DGCNN architecture is used to classify points as sematic categories such as wall, terrain inclined, and straight ramps. It is a graph-based architecture that creates local regions for each point in the point cloud. In these local regions, K neighbors of a point ($P_c$) are found. In order to determine these K neighbors of $P_c$, if the point features are exist, the distance in feature space is used, otherwise spatial distance is used. DGCNN builds a graph for each local region, and the points ($P_c$ and its K neighbors) that belong to the local region are considered nodes of the graph. The edges of the graph are defined only between $P_c$ and its K neighbors. The weights of the edges are x, y, and z coordinates of neighbors relative to $P_c$ in the first layer. In the successive layers, the weights of edges are features of points relative to the previous layer. After local regions and corresponding graphs are constructed, Multi-Layer Perceptron (MLP) is applied to edges for extracting features of points. The features of a local region are extracted by applying the maximum pooling method to the features of all points situated in the local region. In other words, points are evaluated by considering K neighbors in local regions instead of evaluating each point independently. The process steps mentioned above are called EdgeConv operator, and the operator can easily integrate into any architecture. The DGCNN architecture was created by combining the PointNet architecture and EdgeConv operator. In contrast to architectures that process edges of the graph of local

regions, the neighborhood relationship between points is dynamically updated according to feature space. Besides, the local regions are not expanded hierarchically, unlike other architectures.



(a)



(b)



(c)
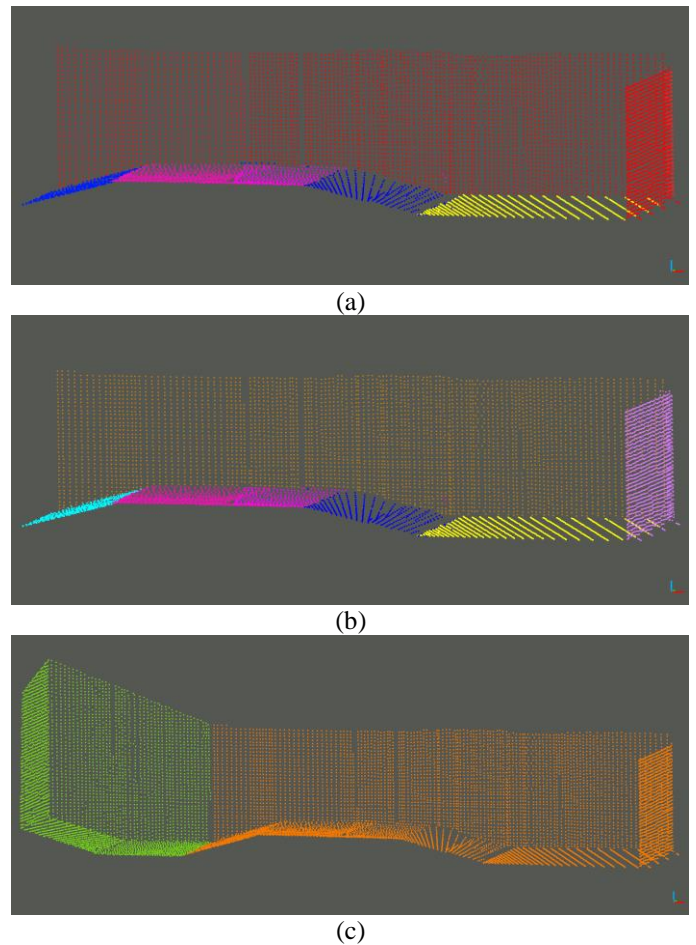
**Figure. 3.** An example for construction of semantic map. (a) Clustering of point depending on class labels. (b) Segmentation of planar surfaces of class. (c) Merging current map with global one.

The DGCNN architecture determines the semantic label of each point in the point cloud data. After that point, we cluster the points in terms of their labels. An example point cloud is shown in Fig. 3(a). In this figure, red, yellow, blue, and purple indicate wall, terrain, inclined, and straight ramps classes, respectively. As seen from the figure, each class could contain different planar surfaces, just like walls orthogonal to each other. Therefore, we apply RANSAC [30] segmentation method to segment a class' points that belong to different planar surfaces. This process is repeated for each class so that each planar surface in the scene is determined. The result of the segmentation process is given in Fig. 3(b). We show each planar surface with different colors in the figure. Lastly, segmented planar surfaces are merged with the global semantic map depending on the position and orientation of the planar surfaces of the current and global map. The resultant semantic map is represented in Fig. 3(c). In the figure, green and orange describe the global and current semantic maps, respectively.

## C. Constructing Metric Map

Robots generally require an appropriate representation of the environment to achieve the tasks they are expected to perform. One of these representations is the metric map. In previous studies, occupancy grids were frequently applied to obtain 2D metric maps. Occupancy grids describe the environment with a grid composes of equal-size cells. Each cell has a probabilistic value between 0 and 1, depending on its amount of occupancy. Besides, each cell must belong to one of the three states: free, occupied, and unknown. In the beginning, all cells are initialized with 0.5 to indicate the unknown state. Then, as the robot gathers information from the environment, the cells' probabilistic value is updated [31]. In a similar manner, the octree data structure is commonly employed to generate 3D metric maps [14, 21]. An example for the octree data structure is given in Fig. 4. First, the data is represented with only one voxel that contains all points. This is generally called level 0 or root node. Then, it splits into eight voxels of the same size (level 1). Simultaneously, voxels of octree are classified as empty (free) and non-empty (occupied), whether consisting of at least one point or not. The process is repeated until the predefined depth or voxel size (VSIZE) is accomplished.

In this study, we utilized RTAB-Map ROS package to construct an octree. RTAB-Map can also determine the state of the voxels as free and occupied since it integrates with OctoMap. As a default, RTAB-Map ROS package only provides occupied voxels. However, it has RayTracing ability that fills the unknown spaces between
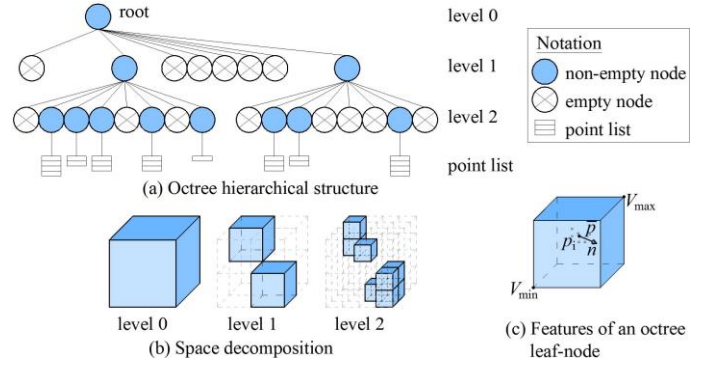


**Figure. 4.** An example for the octree data structure [32].

the sensor and occupied voxels. Therefore, we enabled RayTracing ability to obtain free voxels. An example for constructing the metric map is shown in Fig. 5. In this example, we used the same scene that is given in Fig. 3. The white and black colors in Fig. 5(a) depict free and occupied points taken from the RTAB-Map. The corresponding metric map is shown in Fig. 5(b). At that point, we used the semantic map to classify occupied voxels into walls, terrain, inclined, and straight ramps. To achieve this, we first identified the points that belong to a voxel. Then, the semantic class of each point in that voxel was specified with the aid of the semantic map. Lastly, we calculated a histogram to count the number of points for each class and determined the dominant semantic class, which has the maximum number of points, of that voxel through the histogram. The semantic map and the corresponding metric map of the scene are illustrated in Fig. 5(c) and Fig. 5(d), respectively. In order to merge the current and global metric maps, we first determined the boundary voxels of both maps. Then, we considered the positions and orientations of boundary voxels. Lastly, we found neighbor voxels and merged the maps.

## III. EXPERIMENTAL WORKS

### A. Experimental Setup

We used ROS and Gazebo to conduct the experiments. First, we modeled ESOGU Artificial Intelligence & Robotic Laboratory Search and Rescue Test Arena in Gazebo simulation environment (Fig. 6(a)). The dimensions of environment are 6 x 4 meters. Then, we utilized hector_nist_arenas_gazebo ROS package [33] to insert ramps in the environment (Fig. 6(b)). A Pioneer 3-AT mobile robot was launched in the modeled environment with an Asus XTion Pro RGB-D sensor to capture point cloud data. We used teleop_twist_keyboard ROS package [34] for the teleoperation of the mobile robot.

(a)

(b)

(c)

(d)
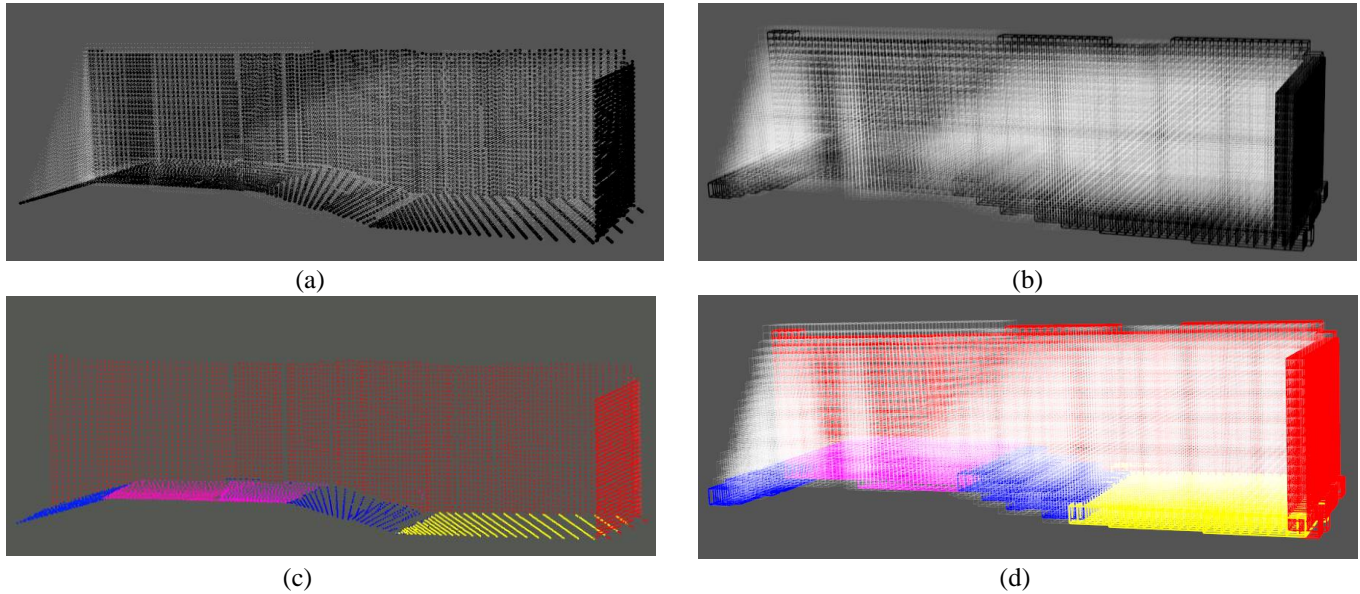
**Figure. 5.** An example for construction of metric map. (a) Free (white) and occupied (black) points taken from the RTAB-Map. (b) Corresponding metric map of (a). (c) Semantic map of the scene. (d) Corresponding metric map of (c).

After each predetermined time interval (TimeInterval), point cloud data was gathered with RTAB-Map ROS package while the robot operates in the simulation environment. The TimeInterval parameter is selected 1 second in this experiment. Also, GridCellSize and MaxNodes parameters of RTAB-Map ROS package are determined as 0.025 and 1, respectively. A preprocessing step must be applied to the point cloud data for the scene classification problem of point-based deep learning architectures. Therefore, the scene is divided into blocks instead of using the entire scene to avoid losing data and detect local features. As a result, we separated a point cloud data into 1 $m^2$ blocks in the xy plane independent from the points' z coordinates. Deep learning architectures accept a fixed number of points. In this study, we specified the number of points in a block as 4096. We applied random upsampling or downsampling to the blocks that contain less than or greater than 4096 points, respectively. Besides, we removed the blocks that have less than 500 points. DGCNN architecture can receive coordinates, normalized coordinates, and color information of points as an input. In this study, we did not use color information, and points were presented with 6D features (x, y, and z coordinates and normalized x, y, and z coordinates). We used the default parameters for scene segmentation of DGCNN architecture.



(a)
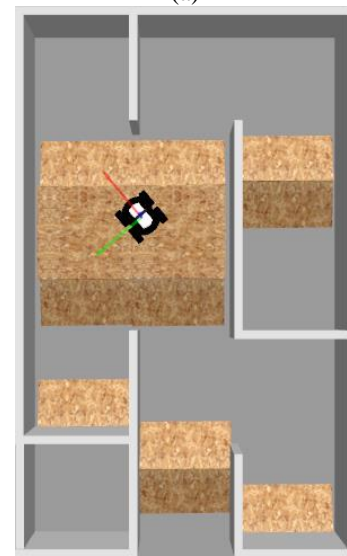


(b)

**Figure. 6.** (a) ESOGU AIRLAB search and rescue test arena, (b) Gazebo model of the test arena.

The DGCNN architecture is implemented in Python programming language using TensorFlow library [35]. However, the remaining parts of the method are realized with C++ programming language. For that reason, we used pybind11 wrapper [36]. After the points belong to each class were determined, we clustered the points depending on the class labels. Besides, we applied RANSAC segmentation method to segment different planar surfaces. The DistanceThreshold parameter of RANSAC is selected 0.02 meters. We used octree_viewer module [37] of the Point Cloud Library (PCL) [38] to visualize the metric map. In this step, VSIZE parameter is chosen 0.05 meters. In order to generate semantic and metric maps of the environment given in Fig. 6(b), the robot navigated for 160 seconds. Therefore, 160 scenes were captured during that process. The experiments were carried out on a PC with Intel i7 processor with 2.8 Ghz, 16 GB RAM, and operating system Ubuntu 20.04.

### B. Experimental Results

The experimental results are shown in Fig. 7. In the figure, the left and right columns illustrate the metric and semantic map of the environment, respectively. The rows of the figure represent the results at some steps. The mapping process was completed at 160 steps, and we preferred to give results at 40, 80, 120, and 160 steps. In the figure, red, yellow, purple, and blue colors represent the wall, terrain, straight, and inclined ramp classes, respectively. We did not visualize points and voxels belong to the free semantic class to clarify figures. As seen from the results, our semantic and metric maps grow incrementally. In this way, the computational complexity of the proposed method was decreased.

The results for semantic maps indicate that the proposed method successfully classifies walls, terrain, and ramps for each scene although the DGCNN model was trained with data gathered in a different simulated environment. Besides, the proposed method calculates and stores properties such as orientation, maximum, and minimum coordinates of each planar surface even though we did not visualize these properties. Then, the method utilizes these properties to merge the current scene and the global semantic map. The experimental results indicate that our method successfully merges the maps to generate an accurate semantic map. In our method, the success of producing a metric map of a scene highly relies on the

semantic map's accuracy. As seen from the figures, the metric map of the environment is generated successfully since the semantic map is accurately created. Then, the current and global maps are integrated carefully with determining boundary voxels. The experimental results for metric maps show that the proposed method merges the maps successfully.

## IV. CONCLUSIONS AND FUTURE WORKS

This study aims to create semantic and metric maps of an environment similar to standard NIST search and rescue test arenas. To do that, we utilized RTAB-Map ROS package and DGCNN architecture. The proposed method grows semantic and metric maps incrementally to decrease the computational complexity. Besides, we prefer to use point cloud data instead of visual data, which many previous studies employed, since point cloud data is more suitable for post-disaster environments. In contrast to previous studies that address producing 3D metric maps, we classified voxels not only occupied and free but also walls, terrain, and ramps. The experimental results indicate that our method successfully generates accurate semantic and metric maps. For future works, we plan to develop a new metric map approach and determine free and occupied voxels without using RTAB-Map since the computational complexity of OctoMap that integrated into RTAP-Map is not appropriate to produce fine-detailed maps. Besides, we aim to create a topological map utilizing the metric map. Thus, the robot can efficiently navigate the environment by preparing the shortest path plan using the topological map.

### CONFLICTS OF INTEREST

There is no conflict of interest.

### RESEARCH AND PUBLICATION ETHICS

The authors declare that this article does not require ethics committee approval or any special permission.

(a) Metric map step 40                                   (b) Semantic map step 40

(c) Metric map step 80                                   (d) Semantic map step 80

(e) Metric map step 120                                  (f) Semantic map step 120

(g) Metric map step 160                                  (h) Semantic map step 160
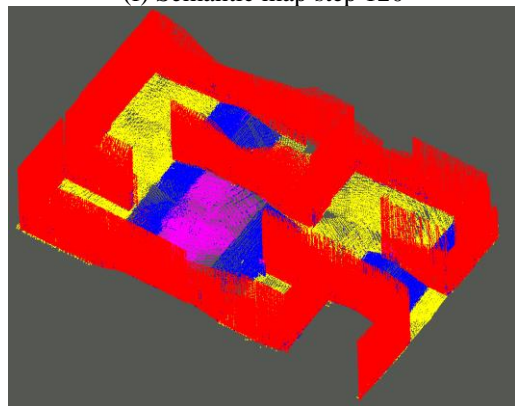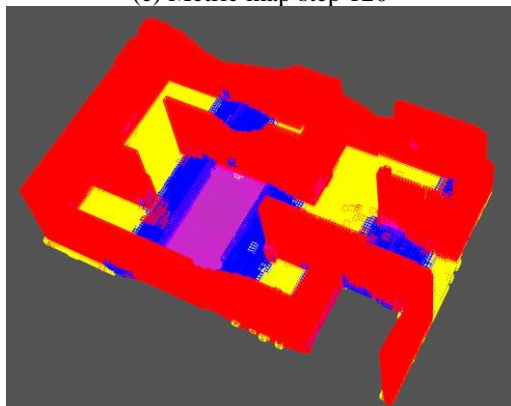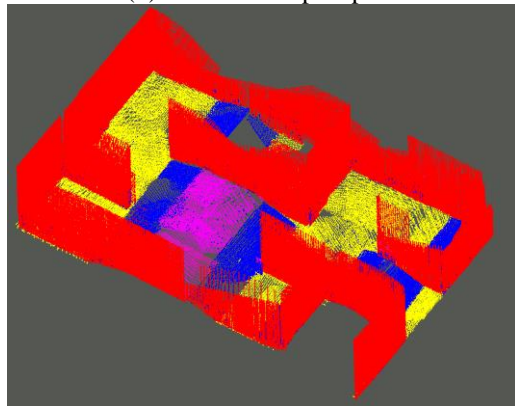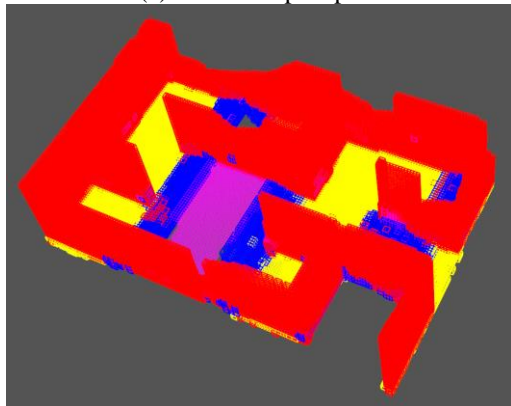
**Figure. 7.** Experimental results.

## REFERENCES

[1] H. Kitano and S. Tadokoro, "RoboCup Rescue: A Grand Challenge for Multiagent and Intelligent Systems," *AI Magazine*, vol. 22, no. 1, pp. 39-52, 2001.

[2] A. Jacoff, E. Messina, B. A. Weiss, S. Tadokoro, and Y. Nakagawa, "Test arenas and performance metrics for urban search and rescue robots," *IEEE/RSJ International Conference on Intelligent Robots and Systems (IROS)*, Las Vegas, NV, USA, 2003.

[3] H. L. Akin, N. Ito, A. Jacoff, A. Kleiner, J. Pellenz, and A. Visser, "Robocup rescue robot and simulation leagues". *AI magazine*, vol. 34, no. 1, pp. 78-86, 2013.

[4] S. Balakirsky, S. Carpin, A. Kleiner, M. Lewis, A. Visser, J. Wang, and V. A. Ziparo, "Towards heterogeneous robot teams for disaster mitigation: Results and performance metrics from robocup rescue", *Journal of Field Robotics*, vol. 24, no. 11, pp. 943-967, 2007.

[5] S. Balakirsky, S. Carpin, and A. Visser, "Evaluating the robocup 2009 virtual robot rescue competition.", *In Proceedings of the 9th Workshop on Performance Metrics for Intelligent Systems,* pp. 109-114, 2009.

[6] F. Amigoni, A. Visser, and M. Tsushima, "RoboCup 2012 Rescue Simulation League Winners.", *In Robocup 2012: Robot Soccer World Cup XVI,Lecture Notes in Artificial Intelligence*, Berlin, Springer, 2013.

[7] R. Sheh, S. Schwertfeger, A. Visser, "16 Years of RoboCup Rescue," *Künstliche Intelligenz*, vol. 30, no.3, pp. 267-277, 2016.

[8] ROS, Available: https://www.ros.org/, Accessed Time: 15.02.2021

[9] GazeboSim, Available: http://gazebosim.org/, Accessed Time: 15.02.2021

[10] K. Ito, K. Yokochi, and Y. Tanaka, "Chukyo Rescue A Team Description Paper for Robocup 2017 Virtual Robot League.", 2017.

[11] G. Grisetti, C. Stachniss, and W. Burgard, "Improved techniques for grid mapping with rao-blackwellized particle filters.", *IEEE transactions on Robotics*, vol. 23 no. 1, pp. 34-46, 2007.

[12] S. Kohlbrecher, O. Von Stryk, J. Meyer, and U. Klingauf, "A flexible and scalable SLAM system with full 3D motion estimation.", *IEEE international symposium on safety, security, and rescue robotics,* pp.155-160, 2011.

[13] S. Yavuz, M. F. Amasyalı, E. Uslu, F. Cakmak, N. Altuntas, S. Marangoz, M. B. Dilaver, A. E. Kırlı, "YILDIZ Team Description Paper for Rescue Simulation League Virtual Robots Competition 2017", 2017.

[14] A. Hornung, K. M. Wurm, M. Bennewitz, C. Stachniss, and W. Burgard, "OctoMap: An efficient probabilistic 3D mapping framework based on octrees.", *Autonomous robots*, vol. 34 no. 3, pp. 189-206, 2013.

[15] S. M. Ahmadi, M. H. G. Nejad, and A. Torabian, "SOS RS Team Description Paper RoboCup 2018 Rescue Virtual Robot League", 2018.

[16] M. Montemerlo, S. Thrun, D. Koller and B.Wegbreit, "FastSLAM: A Factored Solution to the Simultaneous Localization and Mapping Problem", *Association for the Advancement of Artificial Intelligence (AAAI) Conference*, pp. 593-598, 2002.

[17] J. Ziegler, J. Gleichhauf and C. Pfitzner, "RoboCup Rescue 2018 Team Description Paper AutonOHM", 2018.

[18] S. May, P. Koch, R. Koch, C. Merkl, C. Pfitzner, and A. Nuechter, "A Generalized 2D and 3D Multi-Sensor Data Integration Approach based on Signed Distance Functions for Multi-Modal Robotic Mapping.", *In Vision, Modeling, and Visualization (VMV)*, pp. 95-102, 2014.

[19] J. H. Kim, X. Lin, N. Kanyok, A. Shaker, P. Poudel, I. Cardenas, N. Karina, C. Cabrera, H. Jeong, and G. P. Sharma, "RoboCup Rescue 2019 TDP Virtual Robot Simulation." 2019.

[20] M. Labbé and F. Michaud, "Memory management for real-time appearance-based loop closure detection.", *IEEE/RSJ international conference on intelligent robots and systems*, pp. 1271-1276, 2011.
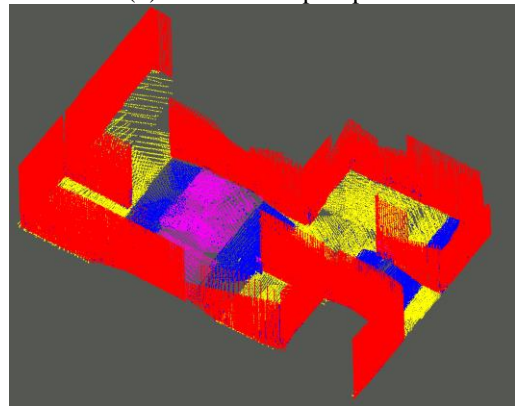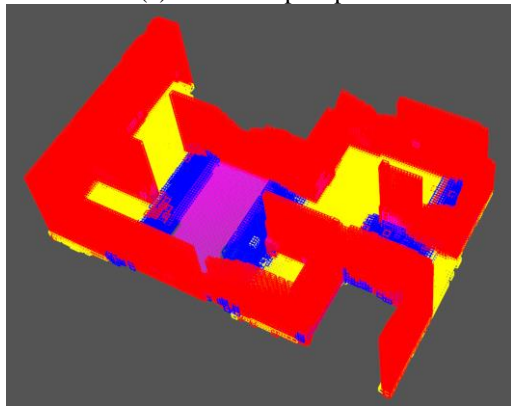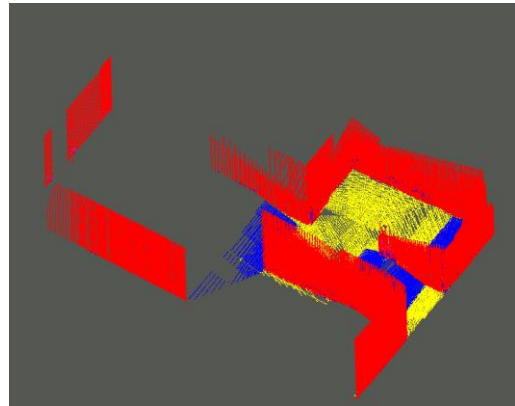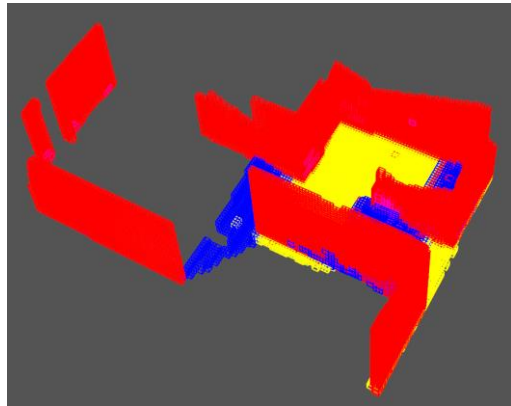
[21] rtabmap_ros, Available: http://wiki.ros.org/rtabmap_ros. Accessed Time: 15.02.2021.

[22] T. Rabbani, F. A. Van Den Heuvel, G. Vosselman, "Segmentation of point clouds using smoothness constraints," ISPRS commission V symposium: image engineering and vision metrology. *International Society for Photogrammetry and Remote Sensing (ISPRS)*, Dresden, Germany, 2006.

[23] M. A. Fischler, R. C. Bolles, "Random sample consensus: a paradigm for model fitting with applications to image analysis and automated cartography," *Communications of the ACM*, vol. 24, no. 6, pp. 381-395, 1981.

[24] W. Deng, K. Huang, X. Chen, Z. Zhou, C. Shi, R. Guo, and H. Zhang,)., "Semantic RGB-D SLAM for Rescue Robot Navigation.", *IEEE Access*, vol. 8, pp.221320-221329, 2020.

[25] K. Turgut and B. Kaleci, "Comparison of Deep Learning Techniques for Semantic Classification of Ramps in Search and Rescue Arenas," *2020 Innovations in Intelligent Systems and Applications Conference (ASYU)*, Istanbul, Turkey, pp. 1-6, 2020.

[26] C. R. Qi, H. Su, M. Kaichun, L. J. Guibas, ''PointNet: Deep learning on point sets for 3D classification and segmentation,'' *in Proc. IEEE Conf. Comput. Vision. Pattern Recognit. (CVPR)*, Honolulu, HI, USA, 2017.

[27] C. R. Qi, L. Yi, H. Su, L. J. Guibas, ''PointNet++: Deep hierarchical feature learning on point sets in a metric space,'' *Conference on Neural Information Processing Systems (NIPS)*, Long Beach, CA, USA, 2017.

[28] Y. Li, R. Bu, M. Sun, W. Wu, X. Di, B. Chen, "PointCNN: Convolution on x-transformed points," *Conference on Neural Information Processing Systems (NIPS)*, Montreal, Canada, 2018.

[29] Y. Wang, Y. Sun, Z. Liu, S. E. Sarma, M. M. Bronstein, J. M. Solomon, "Dynamic graph CNN for learning on point clouds," *ACM Transactions on Graphics*, vol. 38, no. 5, Article 146, 12 pages, 2019.

[30] Point Cloud Library Plane Segmentation Code. Available: https://pointclouds.org/documentation/tutorials/random_sample_consensus.html, Access date: 15.02.2021.

[31] S. Thrun, "Learning Occupancy Grid Maps with Forward Sensor Models". *Autonomous Robots*, vol. 15, pp. 111–127, 2003.

[32] A. Vo, L. Truong-Hong, D. F. Laefer, and M. Bertolotto, "Octree-based region growing for point cloud segmentation", *ISPRS Journal of Photogrammetry and Remote Sensing*, vol. 104, pp. 88-100, 2015.

[33] Hector_nist_arenas_gazebo, Available: http://wiki.ros.org/hector_nist_arenas_gazebo, Accessed Time: 15.02.2021

[34] teleop_twist_keyboard, Available: http://wiki.ros.org/teleop_twist_keyboard, Accessed Time: 15.02.2021

[35] Tensorflow, Available: https://www.tensorflow.org/, Accessed Time: 15.02.2021

[36] pybind11, Available: https://github.com/pybind/pybind11, Accessed Time: 15.02.2021

[37] octree_viewer, Available: https://github.com/PointCloudLibrary/pcl/blob/master/tools/octree_viewer.cpp, Accessed Time: 15.02.2021

[38] R. B. Rusu, S. Cousins, "3D is here: Point Cloud Library (PCL)," *IEEE International Conference on Robotics and Automation (ICRA)*, Shanghai, China, 2011.

RESEARCH ARTICLE

# A Single-Stage Smart Driver with Automatic Dimming Capability for Multiple LED Strings Biased from a Single Point

* Fırat Aydemir, [1] M. Ali Ebeoğlu

* Dumlupinar University, Computer Eng., Kutahya, Turkey, firat.aydemir@dpu.edu.tr, orcid.0000-0002-8965-1429,
[1] Dumlupinar University, Electrical Electronics Eng., Kutahya, Turkey, mali.ebeoglu@dpu.edu.tr, orcid.0000-0003-3045-3003

## HIGHLIGHTS

- *A LED driver that can operate at different LED loads which are commercially available on the market has been designed*
- *The purpose of the designed smart driver is to try to extend the lifetime of the LEDs*
- *The requirement for different LED driver designs for different LED loads is eliminated.*

**\*Correspondence:**

Fırat Aydemir
firat.aydemir@dpu.edu.tr Phone: +90 274 443 4254.

## GRAPHICAL ABSTRACT

A driver system for high-power light-emitting diodes (LEDs) is presented. The proposed driver system is based on flyback converter topology, and it uses single-stage power factor correction with microcontroller support. The driver has two main parts; a source for an LED array, and a control unit including sensors. Instead of using conventional constant voltage or constant current driver topologies, the proposed system adjusts the output voltage by considering the LED parameters, the number of serial and parallel LEDs on the load array, and the data from sensors. Via the current sensor, the output current is measured at specific periods and limited by the microcontroller according to the LED load. Moreover, the microcontroller can detect an open circuit condition on the LED array by following current changes. A temperature sensor and a light-dependent resistor (LDR) are used to increase the lifetime of LEDs.

**Figure A.** The designed LED driver

**Aim of Article :** *This study aims to design a smart LED driver for different LED loads.*

**Theory and Methodology :** *The designed system is a microcontroller-based smart LED driver. The proposed driver adjusts the output voltage and current according to the LED parameters on the load and the data read from the sensors.*

**Findings and Results:** *With the designed prototype driver shown in Figure a, measurements were made for different LED loads, and it has been determined that the driver system worked in harmony with different LED loads and changed the output current and voltage values according to the data received from the sensors.*

**Conclusion :** *With the proposed solution, a smart driver design has been created for commercially available LED PCBs on the market.*

RESEARCH ARTICLE

# A Single-Stage Smart Driver with Automatic Dimming Capability for Multiple LED Strings Biased from a Single Point

\* 🆔 Fırat Aydemir, [1] 🆔 M. Ali Ebeoğlu

\* Dumlupinar University, Computer Eng., Kutahya, Turkey, firat.aydemir@dpu.edu.tr, orcid.0000-0002-8965-1429,
[1] Dumlupinar University, Electrical Electronics Eng., Kutahya, Turkey, mali.ebeoglu@dpu.edu.tr, orcid.0000-0003-3045-3003

**H I G H L I G H T S**

- *A LED driver that can operate at different LED loads which are commercially available on the market has been designed.*
- *The purpose of the designed smart driver is to try to extend the lifetime of the LEDs.*
- *The requirement for different LED driver designs for different LED loads is eliminated.*

**ABSTRACT**

*In this study, a driver system for high-power light-emitting diodes (LEDs) is presented. The proposed driver system is based on flyback converter topology, and it uses single-stage power factor correction with microcontroller support. The driver has two main parts; a source for an LED array, and a control unit including sensors. Instead of using conventional constant voltage or constant current driver topologies, the proposed system adjusts the output voltage by considering the LED parameters, the number of serial and parallel LEDs on the load array, and the data from sensors. Via the current sensor, the output current is measured at specific periods and limited by the microcontroller according to the LED load. Moreover, the microcontroller can detect an open circuit condition on the LED array by following current changes. A temperature sensor and a light-dependent resistor (LDR) are used to increase the lifetime of LEDs.*

**Keywords:** *Light-emitting-diode (LED), LED Driver, Smart Driver, LED life, LED array*

## I. INTRODUCTION

The LED lighting systems gradually began to replace traditional lighting systems thanks to their high brightness, long life, and high-efficiency features [1]. If this conversion was completed all around the world, the total energy saving would be around 1000 TWh/year [2].

The linear power supply units have around 60% efficiency whereas switch-mode power supplies (SMPS) have more than 80% efficiency. Therefore, most of the LED driver circuits based on the switching mode power supply [3]. In addition to being energy efficient, the expectation from LED driver circuits is increasing day by day. They should have a compact structure, be smart, be dimmable, and support equipment that should allow remote control or connection to the IoT platforms. Moreover, the driver circuits are also expected to meet standards in terms of power factor. The single-stage power factor correction (PFC) technique is widely used to reduce the cost, improve efficiency, and extend the current conduction angle of the LED drivers [4]-[9].

Although manufacturers are capable of driving LEDs at higher currents, 1W power LEDs driven at 350mA are commonly used [10],[11]. In many applications, several series and parallel (n*m) LED strings exist to obtain some design requirements such as voltage, current, and power [8],[12]. However, each LED has different forward voltage drops because of its tolerance, which leads to a huge current difference in parallel strings. Therefore, different current balancing methods have been proposed [13]-[17]. Although these techniques are shown improvements in current balancing, they are currently not suitable for commercially available LED printed circuit boards (PCB), because quite a lot of them consist of several LED strings connected in parallel to a single bias point.

In LED lighting applications, the forward voltage drop on each LED decreases with increasing junction temperature of LED [18],[19]. The reasons for the heating at the p-n junction are the ambient temperature and the ohmic heating at the bandgap which is the most important factor affecting the LED life [20]. The LED life can be defined as the duration that LED can produce sufficient light for the specific application which determines the operating time of lighting armature in hours that the output light regresses 70% of its starting light intensity [21]. Therefore, while adjusting the driver output current, the temperature value should also be taken into account as a parameter.

In this study, a LED driver is proposed which can work at different LED PCBs which are commercially available on the market. Moreover, when an open circuit occurs at an individual string on the LED array, the proposed driver can detect this situation, and adjust the output power according to the new load. With the necessary sensors, temperature and environment light intensity are used as parameters in the calculation of the output power of the driver as well.

## II. PRINCIPLE OF OPERATION

Providing the longest LED life and efficiency are the two most important features of the LED driver. It is a big challenge for LED drivers to manage output current and output voltage. Many LED driver circuits use either constant current topology or constant voltage topology. They both are not suitable for the load which is mentioned in the previous section. A threshold

voltage of a diode depends on temperature. Equation 1 shows the diode voltage which depends on temperature [22]:

$$V(T) = \frac{kT}{e} \ln\frac{I}{I_s^*} + \frac{E_g(T)}{e} \qquad (1)$$

The first summand shows the Fermi level and the second summand depends on the changes in bandgap energy which generally has a higher effect from the first summand. As the temperature increases, the energy gap decreases; therefore, applying a constant voltage to LEDs, while the temperature increasing, causes a significant current change. Applying a constant current to LEDs, irrespective of temperature results not only in decreasing the emission intensity of LEDs but also for long-term periods decreasing the lifetime of LEDs. Moreover, a simple constant current driver gets no data from the load; if the load is thought of as a combination of LED strings, and the output current of the driver sets to some value which depends on the operating current of one LED times the number of strings, the driver supplies the same amount of current regardless of the recent situation of the load. Any damage on one or more LED strings causes extra current stress on the remaining strings; as a result, the remaining LEDs cannot stand much longer. Because of these drawbacks, the proposed design uses the combination of these two topologies which is to adjust output voltage depending on the LEDs operating voltage and also adjust the maximum output current that the LED array can get and detect any damage on the load.

The temperature of the p-n junction has to be kept under critical values to be able to obtain the longest LED life [20], [23],[24]. There is no chance to measure the exact temperature of the p-n junction; however, measuring the temperature at the closest point to the p-n junction, the T-point of LED [20], would give an idea about the operating temperature. The temperature can be measured periodically by placing a sensor on the aluminum PCB so that the measured value can be included as a parameter to the equation in setting the output power.

Using the LED armature when it is needed has a significant effect on the lifetime of LEDs. By measuring the daylight intensity, the unwanted operating periods can be minimized. The proposed driver uses automatic analog diming which is the

simplest and cheapest technique is based on changing output voltage value [25].

The proposed system (see Fig.1) is formed from two main parts; the first part is the power circuit (see Fig.2), the second one is the control circuit (see Fig.4).
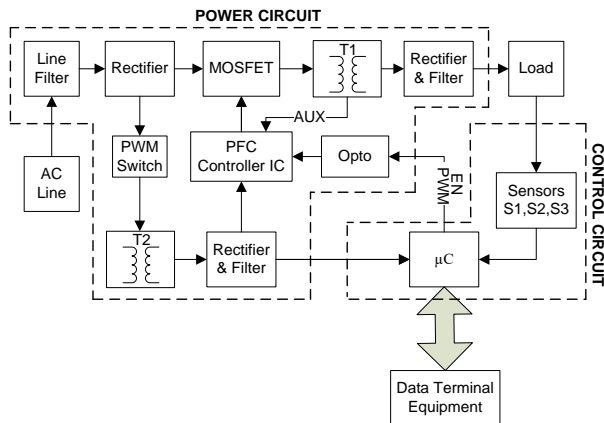


**Figure. 1.** Proposed Driver System

### A. The Power Circuit

The power circuit comprises a line filter, a flyback converter which is the most common converter in low-power LED driver applications because of its simplicity and low cost, and a low-power SMPS which is used to power up the control circuit, and the PFC circuit.
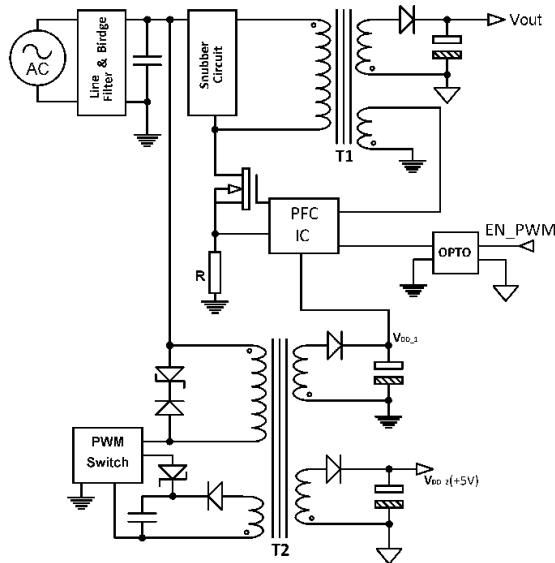


**Figure. 2.** The Power Circuit

The PFC integrated circuit is designed to work in critical conduction mode (CRM). However, in the proposed driver system because of variable output

voltage levels according to LED load, working only at CRM couldn't be enough to get a high-power factor. The driver may not work at full load condition, so the PFC controller has to be controlled as well according to the output voltage. The microcontroller measures the output voltage value continuously and sends a pulse width modulation (PWM) signal to the PFC controller which enables and disables the controller. PWM signal has a fixed frequency but the duty cycle of this signal changes with the required output voltage value, as shown in Fig. 3. If higher voltage values are needed, the duty cycle increases. And with variable on-time & off-time gate signal, the peak inductor current is proportional to the rectified AC line voltage. In this way, the input current waveform follows the input voltage.

By using the second low-power SMPS, the microcontroller can operate independently from the main power supply. Moreover, it also provides a continuous voltage to the PFC IC instead of biasing with a serial resistor from high input voltage after rectifier; thus, an efficient way is chosen which increases the overall efficiency of the driver circuit.
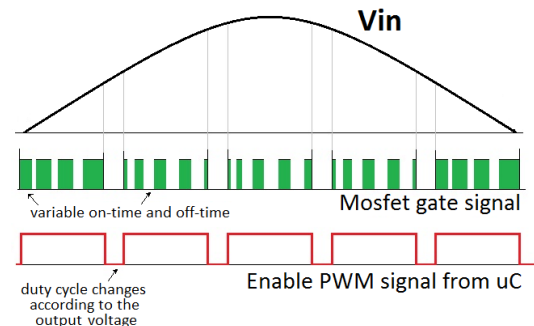


**Figure. 3.** The Switching frequency variations

If any damage happens at the main power supply such as unwanted voltage rising, the microcontroller turns off the main power supply and protects LEDs. Instead of changing the whole armature including LEDs, changing only the driver is more effective in terms of cost. If any damage occurs at the low power SMPS side, there will be no voltage at the load bias output since the microcontroller cannot operate.

### B. The Control Circuit

The block diagram of the control circuit is shown in Fig. 4. The microcontroller is located at the center of this unit and determines the output voltage and current according to the data which are obtained from sensors. The data terminal equipment (DTE) (see Fig.5), which

is used to provide the parameters such as operating & turn-off voltage, operating current of each LED, number of serial LEDs and number of parallel strings in the array, the maximum and critical operating temperatures of LEDs, is another microcontroller-based system.
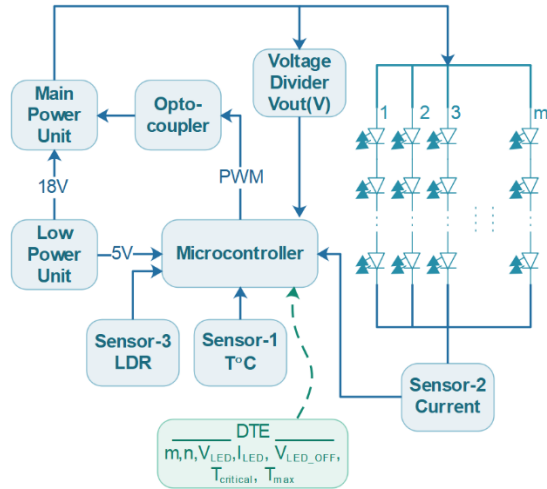


**Figure. 4.** The Control Circuit

These parameters can be set according to the LED load; thus, the same driver can be used for different arrays, as a result, different driver design requirements for different LED loads could be eliminated.



**Figure. 5.** Data Terminal Equipment (DTE)

On the other hand, this concept has some limitations; for example, the maximum number of serial LEDs cannot exceed 14 and cannot be under 7, the parallel number of strings cannot exceed 7 and cannot be under 3; these limitations obtained from experiments are used to maximize the efficiency of the driver circuit.
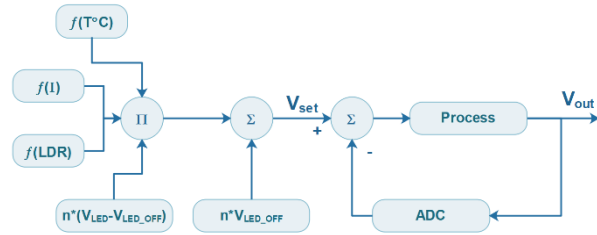


**Figure. 6.** The set output voltage calculation

According to all these parameters set by the DTE, and the data from sensors, the microcontroller sets the output voltage for the load. The set output voltage, $V_{set}$, is calculated with the following procedure which is shown in Fig. 6.

$$V_{set} = n * V_{LED\_OFF} + \left( n * (V_{LED} - V_{LED\_OFF}) \right) * f(sensors) \quad (2)$$

$$f(sensors) = \frac{f(\text{LDR})}{100} * \frac{f(\text{I})}{100} * \frac{f(\text{T°C})}{100} \quad (3)$$

where $n$ is the number of LED in one string in the LED array, $V_{LED\_OFF}$ is the minimum operating voltage for one LED, $V_{LED}$ is the proper operating voltage for one LED, $f(\text{I})$, $f(\text{T°C})$, and $f(\text{LDR})$ are the functions of current, temperature, light intensity of the environment affecting the output voltage respectively.

The output voltage is continuously measured by using a voltage divider and a zener diode that is used to protect the input port of the microcontroller for any high voltage ripples. The theoretical value calculated from equations 2 and 3, $V_{set}$, is compared with the measured value, $V_{out}$. According to the difference between these two values, the duty cycle of the PWM signal applied to the PFC controller is changed between 0 and 90%.

To maximize the lifetime of LEDs, unnecessary usage of the armature has to be prevented. By using LDR, the turn-on time is spread into five different steps. The factor of LDR on the output voltage is shown with $f(\text{LDR})$ and for the highest environment light intensity, it takes the lowest ratio, for the lowest intensity vice versa; so, the driver gets automatic dimming capability. Another important feature of the driver is that the output voltage starts increasing gradually thanks to the automatic dimming capability, so the instantaneous start-ups which can damage the LEDs can be prevented.

A fully integrated, hall effect-based linear current sensor, ACS712, is used to measure the overall array current. The maximum output current is defined as follow;

$$I_{out(max)} = m * I_{LED} \quad (4)$$

and corresponding output voltage value, $V_I$, from the current sensor is [26];

$$V_I = m * I_{LED} * 0.185 + 2.5 \quad (5)$$

where $m$ is the number of parallel strings at the LED array, $I_{LED}$ is the current value for one LED. The sensitivity of the ACS712 current sensor is 0.185V/A.

The microcontroller calculates the maximum output current which the load is capable of drawing with equation 4 and checks the real current continuously. If the output current exceeds this maximum value because of any reason, it starts to decrease the set output voltage by the factor of $f(I)$ to protect the LED array. The relationship between measured current ($I_{out}$) and calculated possible maximum output current ($I_{out\_max}$) is shown below in Fig.7.
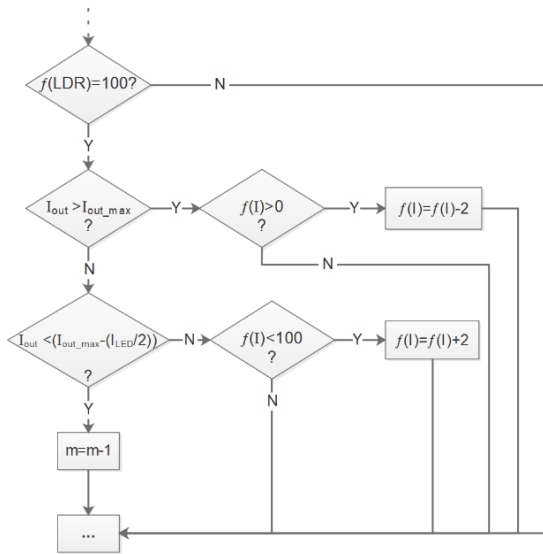


**Figure. 7.** Current Measurement Algorithm

The proposed driver system can detect any open circuit condition on one or more parallel LED strings. When the load has $m$ strings, and then suddenly the measured current is decreased at least by the half of one string current at the highest $f(LDR)$ and $f(T°C)$, the microcontroller reduces the number of parallel strings ($m$) and recalculates the maximum output current that the load can handle. For example; if the load has 4 parallel strings, and one of the LED has 0.35A operating current, so the maximum output current

($I_{out\_max}$) would be 1.4 A. When one of the LED on the string has become an open circuit, the output current would decrease to 1.05 A, which means that $I_{out} < \left(I_{out\_max} - \frac{I_{LED}}{2}\right)$ the condition becomes true. So, the driver decides that one of the parallel strings at the load has been damaged, then it decreases "m" by one. The maximum output current of the new load is set, and the microcontroller prepares an error code to send to the DTE if it is required.

One-wire digital thermometer IC, DS18B20, is used as a temperature sensor to measure the temperature on the aluminum PCB where LEDs are placed. When the temperature exceeds the critical value, which is set via the DTE according to the LED characteristics, the output voltage decreases by the ratio of temperature function. The function is calculated from equation 6:

$$f(T°C) = 100 - \left[(T - T_{critical}) * \left(\frac{100}{T_{max} - T_{critical}}\right)\right] \quad (6)$$

where $T$ is the measured temperature value, $T_{critical}$ is the temperature value that the driver makes an effort to start to decrease, and $T_{max}$ is the maximum temperature value which is not harmful to LEDs. If $T_{max}$ is exceeded, the main power supply is turned off. If the measured temperature is under $T_{critical}$, $f(T°C)$ is set to one hundred.

In addition to the parameter setting functionality of the DTE, it can be also used to read error codes from the driver. These error codes are used to inform the user about the driver to decrease repair time. Error codes:

1. Error Code 0x01: It shows that temperature sensor error. It can happen because of the fault of the temperature sensor or the absence of it.
2. Error Code 0x02: It shows that one or more parallel strings have become open circuits on the LED array.
3. Error Code 0x03: It shows output voltage error.

## III. DESIGN EXAMPLE
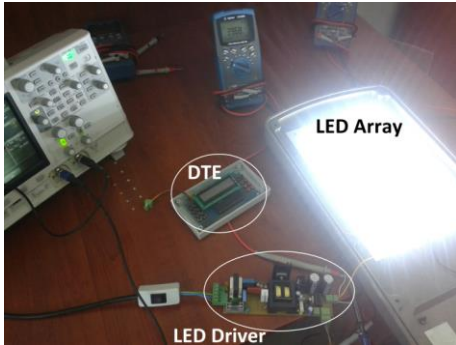


**Figure. 8.** Application Circuit

To verify the feasibility of the proposed LED driver, the prototype driver is tested. For the first measurement, different LED arrays were used as a load to show efficiency, power factor, and cosφ values. The $T_{critical}$, $T_{max}$, $V_{LED}$, $V_{LED_{off}}$, and $I_{LED}$ parameters were set by using DTE to 70°C, 85°C, 3.3V, 2.5V, and 350mA respectively. The input voltage was 220VAC, 50 Hz. The driver was worked at room temperature and the temperature on the LED PCB was under $T_{critical}$ value, so the $f$(T°C) was at maximum value. The light sensor was covered with black paper to avoid environmental lights. For different n and m values, the operating parameters of the driver are shown in Table 1.

**Table I.**
Driver parameters for different LED loads

| n | m | $V_{out}$ (V) | $I_{out}$ (A) | $P_{out}$ (W) | $P_{in}$ (W) | %μ | cosφ | PF |
|---|---|---|---|---|---|---|---|---|
| 8 | 5 | 26.33 | 1.74 | 45.81 | 50 | 91.6 | 0.93 | 0.93 |
| 10 | 6 | 32.69 | 2.094 | 68.45 | 75 | 91.2 | 0.96 | 0.96 |
| 11 | 5 | 36.34 | 1.74 | 63.23 | 71 | 89 | 0.96 | 0.96 |
| 13 | 6 | 43.39 | 2.125 | 92.2 | 104 | 88.6 | 0.98 | 0.98 |
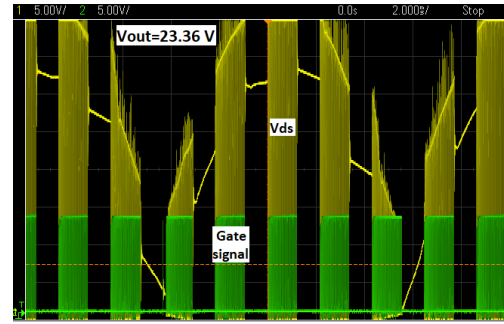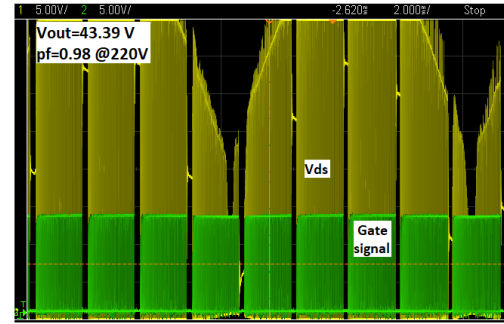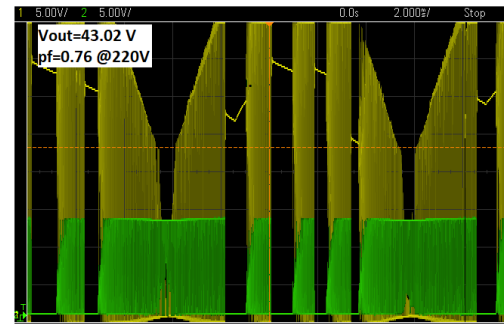


**Figure. 9. a)** The load is n=7, m=3. **b)** The load is n=13, m=6 with PWM enable signal. **c)** The load is n=13, m=6 without PWM enable signal.

In Fig. 9 a. and b., the differences between MOSFET drain voltage and gate signals are shown for two different output voltage levels; at the lower output voltage level, on-time periods of MOSFET are narrow. The effect of using the PWM signal to activate the PFC controller instead of just sending an on-off signal according to the output voltage values is shown in Fig. 9 b. and c. At graphic b. PWM signal makes the MOSFET conduct in particular periods so the input current which is drawn from the AC line can follow voltage. At the graphic c., the on-off signal without any time control decreases the power factor.

The effect of temperature was shown at the second measurement. The light sensor was covered with black paper. By increasing the ambient temperature, the

working temperature of the LEDs was forced to increase. In this way, the output power changes could be monitored (see Fig.10). After the critical temperature value, the output voltage started to decrease so the output power. When the temperature reached the maximum value, the main power supply was turned off by the control unit.
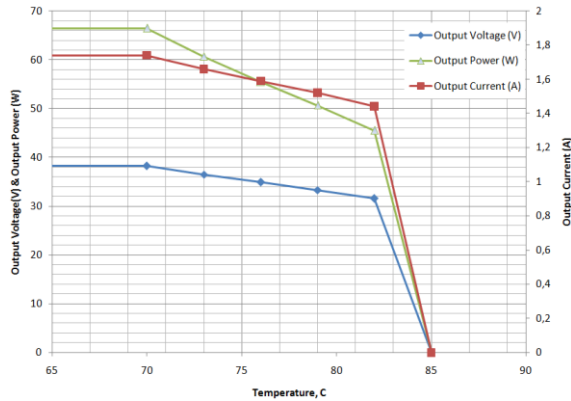


**Figure. 10.** Temperature vs. Output Power, Voltage & Current

The output voltage starts increasing gradually to prevent instantaneous start-up damages on the LEDs; this situation is shown in Fig. 11.
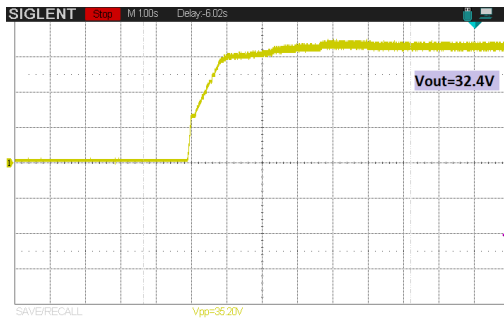


**Figure. 11.** The driver soft start-up

When the output voltage is 32.4V, the output voltage ripple is 2.8V peak-to-peak which is about 8.6% (see Fig. 12).
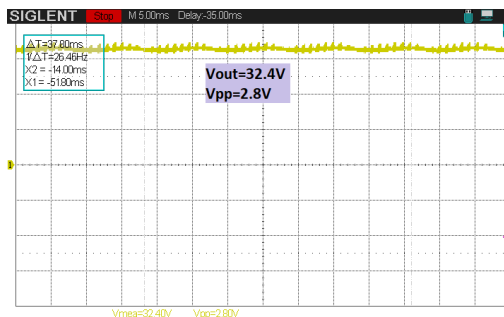


**Figure. 12.** The output voltage ripple

## IV. CONCLUSION

An efficient and smart LED driver system is presented. By controlling the LEDs' temperature, the light intensity, the output current, and the voltage the lifetime of LEDs could be increased. Keeping the operating temperature of LEDs at nominal values is very important to increase the lifetime; therefore, the microcontroller adjusts the output power according to temperature on the LED PCB. Unnecessary usage of LEDs is minimized with LDR to increase efficiency, and the driver gets an automatic dimming capability. The output current is measured continuously and limited as mentioned in LED characteristics. By detecting unexpected current decreases because of an open circuit situation on one or more LEDs, the new maximum output current which load can handle is calculated by the microcontroller, and the new current limit is updated; so any current stress on the remaining LEDs is prevented. However, any short circuit situation on LEDs cannot be detected in this system. The output voltage of the driver is set according to the characteristics of one LED and the parameters of the whole LED strings. By using the DTE which is connected to the driver, the key parameters about LEDs are loaded into the microcontroller so the driver becomes suitable for any load which is in the efficiency limitations of the driver. The DTE also informs the user about the errors which happen at load or the driver itself to minimize repairing time. The next study will be focused on integrating PFC into the microcontroller, adding remote control and data collection properties.

### CONFLICTS OF INTEREST

There is no conflict of interest.

### RESEARCH AND PUBLICATION ETHICS

The authors declare that this article does not require ethics committee approval or any special permission.

### REFERENCES

[1] Y. Wang, J. M. Alonso and X. Ruan, "A Review of LED Drivers and Related Technologies," in *IEEE Transactions on Industrial Electronics*, vol. 64, no. 7, pp. 5754-5765, July 2017.

[2] M. R. Krames, O. B. Shchekin, R. Mueller-Mach, G. O. Mueller, L. Zhou, G. Harbers, and M. G. Craford, "Status and Future of High-Power Light-Emitting Diodes for Solid-State Lighting," Display Technology, Journal of, vol.3, no.2, pp.160,175, June 2007.

[3] Yan-Cun Li; Chen, Chern-Lin, "A Novel Single-Stage High-Power-Factor AC-to-DC LED Driving Circuit

With Leakage Inductance Energy Recycling," IEEE Trans. Industrial Electronics, vol.59, no.2, pp.793,802, Feb. 2012.

[4] Moschopoulos, G.; Jain, P., "Single-phase single-stage power-factor-corrected converter topologies," IEEE Trans. Industrial Electronics, vol.52, no.1, pp.23 -35, Feb. 2005.

[5] J. Lee, J. Kwon, E. Kim, W. Choi and B. Kwon, "Single-Stage Single-Switch PFC Flyback Converter Using a Synchronous Rectifier," in IEEE Transactions on Industrial Electronics, vol. 55, no. 3, pp. 1352-1365, March 2008.

[6] Y. Wang, J. Huang, G. Shi, W. Wang and D. Xu, "A Single-Stage Single-Switch LED Driver Based on the Integrated SEPIC Circuit and Class-E Converter," in IEEE Transactions on Power Electronics, vol. 31, no. 8, pp. 5814-5824, Aug. 2016.

[7] B. Poorali and E. Adib, "Analysis of the Integrated SEPIC-Flyback Converter as a Single-Stage Single-Switch Power-Factor-Correction LED Driver," in IEEE Transactions on Industrial Electronics, vol. 63, no. 6, pp. 3562-3570, June 2016.

[8] X. Liu, Q. Yang, Q. Zhou, J. Xu and G. Zhou, "Single-Stage Single-Switch Four-Output Resonant LED Driver With High Power Factor and Passive Current Balancing," in IEEE Transactions on Power Electronics, vol. 32, no. 6, pp. 4566-4576, June 2017.

[9] B. Poorali, E. Adib and H. Farzanehfard, "A Single-Stage Single-Switch Soft-Switching Power-Factor-Correction LED Driver," in IEEE Transactions on Power Electronics, vol. 32, no. 10, pp. 7932-7940, Oct. 2017.

[10] C. Moo, Y. Chen, S. Member, and W. Yang, "An Efficient Driver for Dimmable LED Lighting," IEEE Trans. Power Electron., vol. 27, no. 11, pp. 4613–4618, 2012.

[11] S. Li, S. Tan, C. K. Lee, E. Waffenschmidt, S. Y. Hui and C. K. Tse, "A survey, classification, and critical review of light-emitting diode drivers," in IEEE Transactions on Power Electronics, vol. 31, no. 2, pp. 1503-1516, Feb. 2016.

[12] R. Zhang; H. Chung; "Transformer-Isolated Resonant Driver for Parallel Strings with Robust Balancing and Stabilization of Individual LED Current," IEEE Trans. Power Electron., vol.29, no.7, pp.3694-3708, Jul. 2014.

[13] S. N. Li, W. X. Zhong, W. Chen and S. Y. R. Hui, "Novel Self-Configurable Current-Mirror Techniques for Reducing Current Imbalance in Parallel Light-Emitting Diode (LED) Strings," in IEEE Transactions on Power Electronics, vol. 27, no. 4, pp. 2153-2162, April 2012.

[14] S. Li and S. Y. Ron Hui, "Self-Configurable Current-Mirror Circuit With Short-Circuit and Open-Circuit Fault Tolerance for Balancing Parallel Light-Emitting Diode (LED) String Currents," in IEEE Transactions on Power Electronics, vol. 29, no. 10, pp. 5498-5507, Oct. 2014.

[15] Y. Yu, F. Zhang and J. Ni, "Capacitor clamped current sharing circuit for multi-string LEDs," 2012 IEEE Energy Conversion Congress and Exposition (ECCE), Raleigh, NC, 2012, pp. 3568-3574.

[16] Y. Hu and M. M. Jovanovic, "LED Driver With Self-Adaptive Drive Voltage," in IEEE Transactions on Power Electronics, vol. 23, no. 6, pp. 3116-3125, Nov. 2008.

[17] X. Liu, Q. Yang, Q. Zhou, J. Xu and G. Zhou, "Single-Stage Single-Switch Four-Output Resonant LED Driver with High Power Factor and Passive Current Balancing," in IEEE Transactions on Power Electronics, vol. 32, no. 6, pp. 4566-4576, June 2017.

[18] J. Yeon, D. Kim, K. Cho, and H. Kim, "A single stage flyback power supply unit for LED lighting applications," Electrical and Electronics Engineering, 2009. ELECO 2009. International Conference on, vol., no., pp.I-288, I-292, 5-8 Nov. 2009.

[19] P. S. Almeida, V. C. Bender, H. A. C. Braga, M. A. Dalla Costa, T. B. Marchesan and J. M. Alonso, "Static and Dynamic Photoelectrothermal Modeling of LED Lamps Including Low-Frequency Current Ripple Effects," in IEEE Transactions on Power Electronics, vol. 30, no. 7, pp. 3841-3851, July 2015.

[20] Narendran, N.; Gu, Y., "Life of LED-based white light sources," Journal of Display Technology, vol.1, no.1, pp.167,171, Sept. 2005.

[21] Alliance for Solid-State Illumination Systems and Technologies (ASSIST), ASSIST Recommends: LED Life for General Lighting, Lighting Research Center, vol.1, no.1, February 2005.

[22] E.Fred Schubert, "Light-Emitting Diodes", pp. 104-107, Cambridge University Press, 2003.

[23] Garcia, J.; Dalla-Costa, M.A.; Cardesin, J.; Alonso, J.M.; Rico-Secades, M., "Dimming of High-Brightness LEDs by Means of Luminous Flux Thermal Estimation," IEEE Trans. Power Electron., vol.24, no.4, pp.1107-1114, April 2009.

[24] X. Perpiñà et al., "Thermal Analysis of LED Lamps for Optimal Driver Integration," in IEEE Transactions on Power Electronics, vol. 30, no. 7, pp. 3876-3891, July 2015.

[25] Gacio, D.; Alonso, J.M.; Garcia, J.; Campa, L.; Crespo, M.J.; Rico-Secades, M., "PWM Series Dimming for Slow-Dynamics HPF LED Drivers: The High-Frequency Approach," IEEE Trans. Industrial Electronics, vol.59, no.4, pp.1717,1727, April 2012.

[26] Fully Integrated, Hall Effect-Based Linear Current Sensor IC with 2.1 kVRMS Isolation and a Low-Resistance Current Conductor, Allegro microsystems, ACS712 product datasheet, rev.14, pp. 5-9, 2011.

RESEARCH ARTICLE

# DSTATCOM Based on Artificial Neural Networks and Particle Swarm Optimization for Voltage Profile Improvement

[1,*] iD Fouad Rashed Zaro

[*,1] Palestine Polytechnic University, Hebron, Palestine, fzaro@ppu.edu, Orcid: 0000-0003-3107-0661

## HIGHLIGHTS

- *The distribution static synchronous compensator (DSTATCOM) is used with a developed control strategy*
- *DSTATCOM control is developed based on artificial intelligent (AI) using the artificial neural network (ANN)*
- *DSTATCOM is used to improve voltage profile with acceptable voltage harmonic distortion.*

**\*Correspondence:**
Fouad Rashed Zaro
fzaro@ppu.edu
Phone: +

## GRAPHICAL ABSTRACT

The configuration parameters of DSTATCOM connected on power grid is shown in Figure A. the real and reactive power of DSTATCOM controlled by the inverter voltage magnitude $V_c$ and the angle α difference between the bus voltage and the output voltage of the inverter. The controller of DSTATCOM is designed due to the dynamic equations of the system and according to the consideration that the system is linear system.

**Figure A.** DSTATCOM Configuration connected on power system

- **Aim of Article:** *This study aims to design a DSTATCOM controller based on artificial intelligent (AI) techniques.*

**Theory and Methodology:** *The designed system is a controller based on artificial intelligent techniques. The proposed controller improves the voltage profile and eliminate the harmonic in the system as well as enhance the power quality.*

**Findings and Results:** *With the designed controller shown in Figure A, the efficient of using AI technique for tuning PI controller of DSTATCOM in order to improve the voltage profile on distribution system. The DSTATCOM with developed controller validated the importance of AI methods.*

**Conclusion :** *Using the proposed controller increase stability and reliability of power system and hence the network converts to smart network. The simulation results proved the efficient of suggested method for controlling DSTATCOM in order to improve voltage profile on distribution system.*

RESEARCH ARTICLE

# DSTATCOM Based on Artificial Neural Networks and Particle Swarm Optimization for Voltage Profile Improvement

[1,*] iD Fouad Rashed Zaro

[*,1] Palestine Polytechnic University, Hebron, Palestine, fzaro@ppu.edu, Orcid: 0000-0003-3107-0661

## HIGHLIGHTS

- *The distribution static synchronous compensator (DSTATCOM) is used with a developed control strategy*
- *DSTATCOM control is developed based on artificial intelligent (AI) using the artificial neural network (ANN)*
- *DSTATCOM is used to improve voltage profile with acceptable voltage harmonic distortion.*

**ABSTRACT**

*Recently the demand for electric power is increased due to increasing the residential and industrial facilities which may contain sensitive nonlinear loads that needed high power quality (PQ) on the distribution system to avoid malfunction operation. One main PQ issue is voltage profile improvement with acceptable voltage harmonic distortion. It should be regulated to be within acceptable standard levels. In order to improve the voltage profile, the distribution static synchronous compensator (DSTATCOM) is used with a developed control strategy. In this research, DSTATCOM control is developed based on artificial intelligent (AI) using the artificial neural network (ANN), which depends on optimum values obtained by using particle swarm optimization (PSO). The results of the simulation proved the superiority and robustness of the proposed control strategy of DSTATCOM for improving the voltage profile on the distribution system. The validation of results has been done by MATLAB/Simulink software package.*

**Keywords:** *DSTATCOM, Artificial Neural Networks, PI controller, Power Quality, Voltage Profile*

## I. INTRODUCTION

The rapid increase in electrical power demand leads emerging use of renewable energy sources (RES) and distributed generations (DGs) in electrical grid. Emerging new resources of energy into the grid and connecting different types of loads such as nonlinear loads create different problems appears in current, voltage and/or frequency which causes error and malfunction of instrument and generally consider as power quality (PQ) problems [1].

Several studies are done regarding PQ issues using the benefits of huge developments in power electronics technologies, hence the network change from traditional network to smart network. Also, PQ may define as electrical constraints that allows an equipment function properly with high performance. According to these definitions of PQ, poor PQ will affect badly on the reliability and stability of electrical network as well as on sensitive loads connected to the end user of distribution bus. PQ is relating to the three main factors: voltage, current and frequency, all these factors should be remaining within their standard limits [2].

The problems of PQ in the network caused by different reasons such as connecting nonlinear loads especially large motors in industrial applications, power electronics devices, switching capacitor banks and connected new electrical resources to the grid. Indeed, these disturbances effect on the performance and functionality of both distribution system and sensitive equipment. The smart grid (SG) technology opens a wide range for solving PQ problems. Family related to power electronics technologies called flexible alternating current transmission systems (FACTs) support SG system and provide solutions for PQ challenges. One application of FACTs family is called distribution static synchronous compensator (DSTATCOM), which is a shunt device connected with distribution bus. One of the main aspects of power system is voltage var control, so the voltage var optimization (VVO) is the main SG application that enhances both security and economy of power system. Nowadays, the artificial intelligence (AI) development plays main role in optimizations power system issues mainly in SG [3].

Several research of PQ issues has focused on enhancing and improving the reliability and stability of electrical grid. These researches pay attention in issues like regulation of improving voltage profile in power system, unbalance conditions in the systems that caused by unbalanced loading and change the load and symmetrical and unsymmetrical faults, real and reactive power losses according to presence harmonic distortion low power factor (PF). Several FACTs devices are used to mitigate these PQ issues. Different control strategies used in DSTATCOM are sensitive to non-ideal supply conditions and load variation which needed careful design tuning controller for each specific insulation. Also, the cost of the system increases due to use special devices such as LCL filter. Other control strategies of DSTATCOM in literature needed complex control facilities and controllers, also needed additional supplementary components such as active filter. In addition, the controller may need additional delay time due the conversion from analogue to digital [4-5].

On the other side new proposed control strategies for DSTATCOM are implemented such as adaline based algorithm and direct method which depends mainly on position and magnitude control of output voltage. Although these methods are validated as efficient methods for controlling DSTATCOM, they are complex and expensive comparing with traditional methods. Different mathematical theories and physical

models are used in analysis and implementing different control strategies of DSTATCOM. Instantaneous power theory, rotating reference frame (dq0), stationary reference frame, instantaneous reactive power (IRP) and Park's transformation are used to simplify the dynamic system equations [6-7].

Significant research has been concerned with FACTs devices and smart control compatible with renewable energy resources. Existing RES and DGs in power system create different challenges especially when these resources with high penetration levels. To deal with these challenges a SG technology is vital to manage the power flow generated by grid. Power generated from RES and the compensation power generated or absorbed by FACTs devices. Using SG technology leads to increase the reliability and stability of power system regardless of high perpetration level of RES connected to distribution bus. Many studies accomplished regarding optimization methods for different PQ issues in power system. These studies include a comparative of meta-heuristic approach such as GA, PSO, differential evolution (DE), harmony search (HS) and seeker optimization algorithm (SOA) [8-13]. From the literature review, therefore great challenges regarding using AI techniques for tuning PI controller of DSTATCOM. This work will suggest using ANNs as a technique for tuning controller of DSTATCOM, which its controller constants is selected optimally using PSO [14-17].

This paper introduces an AI technique specifically PSO and ANN used for design controller of DSTATCOM to enhance the profile of voltage on distribution electrical power system. section II introduces DSTATCOM configuration and design. Mathematical model of the proposed system is presented in Section III. In section IV the developed AI techniques and proposed optimization method are presented in details for constructing the developed controller for DSTATCOM. Section V presents the methodology which include the description of real distribution system as a case study. The simulation results of the proposed scenarios in this study and detailed discussion of all results for voltage events like sag and swell are showed in Section VI. Finally, the performance and efficiency and superiority of the proposed approach are summarized in section VII.

## II. DSTATCOM CONFIGURATION AND DESIGN

### A. Principle and Operation of DSTATCOM

The circuit diagram of the equivalent model of DSTATCOM is shown in Fig.1 [6].
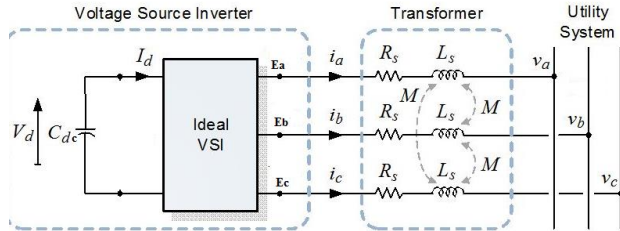


**Figure 1:** Equivalent model of DSTATCOM.

Where:

$R_s$ and $L_s$: are DSTATCOM transformer resistance and inductance respectively.

$E_{abc}$: are converter AC side phase voltages.

$V_{abc}$: are the ac system side phase voltages.

$i_{abc}$: are phase currents.

$I_d$: is capacitor current.

$C_{dc}$: is dc capacitor value.

The main electronic part of DSTATCOM is VSC, that converts dc voltage to ac voltage. The types of VSC are used in this study:

1. Square wave 48-step voltage waveform of four three level inverters is made using gate turn-off thyristor, on the other hand, to eliminate harmonics from the output voltage waveform special inter connection transformers are used.
2. PWM is used to convert DC input voltage to AC output voltage sinusoidal waveform, this inverter uses isolated gate bipolar transistor (IGBT).

   The converter is connected to high voltage side of power system through the coupling shunt transformer. Fig. 2 shows the single line diagram of the simplified equivalent circuit of STATCOM.
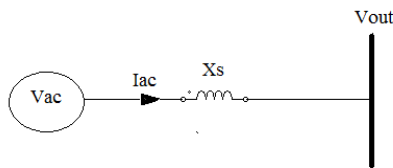


**Figure 2:** Equivalent circuit of DSTATCOM.

Where:

$V_{ac}$: ac voltage of the system

$V_{out}$: output voltage of the converter

$I_{ac}$: ac current flows through the reactance between the converter and ac system

The operation of DSTATCOM is summarized by three modes:

1. *Mode1*: when the output voltage $V_{out}$ amplitude is greater than of the voltage of utility bus $V_{ac}$, in this condition the current flows from the converter to AC side of power system through the reactance and the DSTATCOM injects reactive power into the AC side of power system.
2. *Mode2*: when the $V_{out}$ amplitude is less than of voltage at the utility bus, under this situation the current flows from the AC side of power system to the converter, DSTATCOM absorbs reactive power from AC power system.
3. *Mode3*: when the output voltage $V_{out}$ amplitude equals the voltage amplitude at AC side of power system, then there is no reactive power exchange between DSTATCOM and power system, in this case DSTATCOM is in floating state.

### B. Control Strategy of DSTATCOM

The PI controller is used to control the function of DSTATCOM to inject the required reactive current to the load. Fig. 3 shows the simplified scheme of control strategy of DSTATCOM [8].
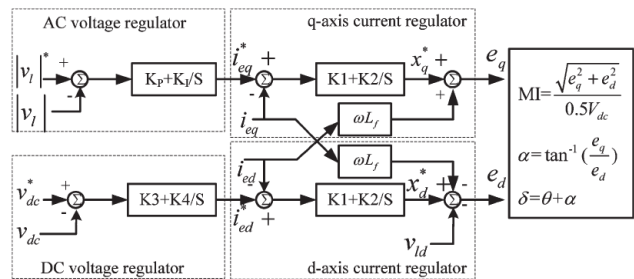


**Figure 3:** control strategy scheme of DSTATCOM

According to modulation index (MI) and phase angel α between the inverter voltage and line voltage PWM controls the output voltages for VSI. The PI controller of DSTATCOM controls the generating/absorbing the desired reactive power at the common coupling point in power system [11]. The goal of such control is to maintain constant voltage magnitude at PCC under system disturbances. Fig. 4 shows the controller input is an error signal which is the difference between the RMS reference voltage (1pu) and the RMS value of the

terminal voltage measured. The PI controller process the error signal and generate the required drive angle to minimize the error to zero [15].
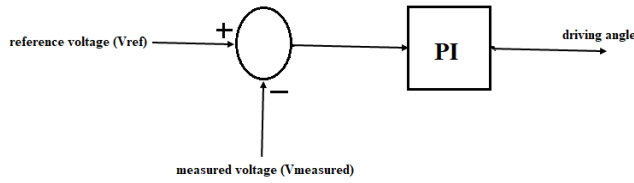


**Figure 4**: Direct PI control of DSTATCOM

### III. MATHEMATICAL MODEL OF PROPOSED DSTATCOM

The study of control strategy of DSTATCOM is according to the simplified mathematical formulas because of DSTATCOM has nonlinear operation structure, the configuration parameters of DSTATCOM connected on power grid is shown in Figure 5 [8].
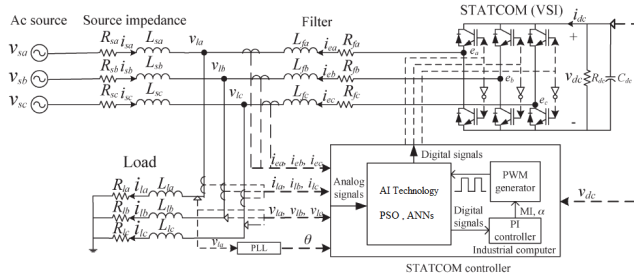


**Figure 5:** DSTATCOM Configuration connected on power system.

The real and reactive power of DSTATCOM controlled by the inverter voltage magnitude Vc and the angle α difference between the bus voltage and the output voltage of the inverter. The active and reactive power compensation of DSTATCOM is described by the equations (1) & (2), respectively [10]:

$$P = \frac{V_{Pcc}V_c \sin\alpha}{X} \tag{1}$$

$$Q = \frac{V_{Pcc}(V_{Pcc} - V_c \cos\alpha)}{X} \tag{2}$$

Where:

P: active Power.
Q: reactive Power
$V_c$: inverter Voltage
$V_{pcc}$: voltage at the point of common coupling
α: angle of $V_{pcc}$ with respect to $V_c$

X: reactance of the branch and the transformer.

The controller of DSTATCOM is designed due to the dynamic equations of the system and according to the consideration that the system is linear system [8].

#### A. Load Model Mathematical Equations

As shown in Fig. 5 due to the explained configuration of the system, the three phase load voltages coordinates may written as:

$$\begin{pmatrix} V_{la} \\ V_{lb} \\ V_{lc} \end{pmatrix} = R_l \begin{pmatrix} i_{la} \\ i_{lb} \\ i_{lc} \end{pmatrix} + L_l \begin{pmatrix} i_{la} \\ i_{lb} \\ i_{lc} \end{pmatrix} \tag{3}$$

To convert three phase balanced system into two phase dq0 system the park transformation can be used to do that, the following equation shows park transformation

$$T = \frac{2}{3} \begin{bmatrix} \cos\theta & \cos(\theta - \frac{2\Pi}{3}) & \cos(\theta + \frac{2\Pi}{3}) \\ -\sin\theta & -\sin(\theta - \frac{2\Pi}{3}) & -\sin(\theta + \frac{2\Pi}{3}) \\ \frac{1}{2} & \frac{1}{2} & \frac{1}{2} \end{bmatrix} \tag{4}$$

The rotating reference frame is described by

$$\begin{pmatrix} V_{ld} \\ V_{lq} \end{pmatrix} = R_l \begin{pmatrix} i_{ld} \\ i_{lq} \end{pmatrix} + L_l \frac{d}{dt} \begin{pmatrix} i_{ld} \\ i_{lq} \end{pmatrix} + L_l \begin{pmatrix} 0 & -w \\ w & 0 \end{pmatrix} \begin{pmatrix} i_{ld} \\ i_{lq} \end{pmatrix} \tag{5}$$

Where $\theta = \tan^{-1}\frac{V_{lq}}{V_{ld}}$

#### B. VSI AC-Side Model

The source voltage Vs and the inverter output voltage can be written as: respectively [23].

$$\begin{pmatrix} V_{sa} \\ V_{sb} \\ V_{sc} \end{pmatrix} = \frac{a_1}{L_l}\begin{pmatrix} i_{sa} \\ i_{sb} \\ i_{sc} \end{pmatrix} \frac{b_1}{L_l}\frac{d}{dt}\begin{pmatrix} i_{ea} \\ i_{eb} \\ i_{ec} \end{pmatrix} \frac{c_1}{L_l}\begin{pmatrix} i_{ea} \\ i_{eb} \\ i_{ec} \end{pmatrix} \frac{d_1}{L_l}\begin{pmatrix} e_a \\ e_b \\ e_c \end{pmatrix} \tag{6}$$

$$\begin{pmatrix} e_a \\ e_b \\ e_c \end{pmatrix} = \frac{a_2}{L_l}\begin{pmatrix} i_{sa} \\ i_{sb} \\ i_{sc} \end{pmatrix} + \frac{b_2}{L_l}\frac{d}{dt}\begin{pmatrix} i_{sa} \\ i_{sb} \\ i_{sc} \end{pmatrix} + \frac{c_2}{L_l}\begin{pmatrix} i_{ea} \\ i_{eb} \\ i_{ec} \end{pmatrix} + \frac{d_2}{L_l}\begin{pmatrix} V_{sa} \\ V_{sb} \\ V_{sc} \end{pmatrix} \tag{7}$$

where:

$a_1 = (R_s L_l - R_l L_s)$
$b_1 = -(L_s L_f + L_s L_l + L_l L_f)$
$c_1 = -(R_f L_s + R_l L_s + R_f L_l)$
$d_1 = (L_s + L_l)$

$$a_2 = -(R_s L_f + R_l L_f + R_s L_l)$$
$$b_2 = -(L_s L_f + L_l L_f + L_s L_l)$$
$$c_2 = (R_f L_l - R_l L_f)$$
$$d_2 = (L_f + L_l)$$

### C. VSI DC-Side Model Equations

The power balance equation for VSI can be expressed as:

$$V_{dc} i_{dc} = \frac{3}{2}(e_d i_{ed} + e_q i_{eq})  \qquad (8)$$

$V_{dc}$ can be derived from a current balancing formula as:

$$\frac{d}{dt} V_{dc} = -(\frac{V_{dc}}{R_{dc} C_{dc}} + \frac{i_{dc}}{C_{dc}})  \qquad (9)$$

The current $i_{dc}$ can be expressed as:

$$i_{dc} = \frac{3}{2V_{dc}}(e_d i_{ed} + e_q i_{eq})  \qquad (10)$$

### D. DSTATCOM Design

DSTATCOM components should be calculated due to the equations of the mathematical model of the selected system [11], and these components are:

- *Design DC Bus Voltage*

The voltage DC link must be sufficient enough to obtain current compensation using the following equation can be calculated

$$V_{dc\,min} > \sqrt{2}V_{L-L(rms)} = \sqrt{2}\sqrt{3}V_{L-N(rms)}  \qquad (11)$$

- *Design DC Bus Capacitor*

According to the energy conservation principle, the $C_{dc}$ may calculated by:

$$\frac{1}{2} C_{dc}[V_{dc}{}^2 - V_{dc1}{}^2] = 3\,k\,a\,V\,I\,t  \qquad (12)$$

Where:
$V_{dc}$: is the reference DC bus Voltage
$V_{dc1}$: is the minimum level of the DC bus voltage
a: is the over loading factor
V: is the phase voltage
I: is the phase current
t: is the time for which the DC bus voltage is to be recovered
k: factor for variation of energy during dynamics

- *Design AC Interfacing Inductor*

The selection of suitable filter depends on the ripple current icr-pp, switching frequency fs and DC bus voltage $V_{dc}$ is given in Eq.13:

$$L_f = \frac{\sqrt{3}\,m\,V_{dc}}{12\,a\,f_s\,i_{cr-pp}}  \qquad (13)$$

Where *m* is modulation index.

- *Design Passive High Pass Ripple Filters*

To eliminate the high frequency noise from the voltage waveform at PCC in the power system the high pass filter is needed to do that, it could be calculated by the following formula:

$$R_r C_r = \frac{T_s}{10}  \qquad (14)$$

## IV. ARTIFICIAL INTELLIGENCE AND OPTIMIZATION TECHNIQUES

### A. Particle Swarm Optimization

PSO is a heuristic search optimization technique, inspired by social and cooperative behaviors. The technique is related to the main parts. One is guided by personal behavior (P_best) and the other part guided by social experience (G_best). The position of particle in search space is updated depends on these two parts [14]. The core equations of this technique are

$$V_{i,j}^{k+1} = w \times V_{i,j}^{k} + c_1 \times r_1 \times (P_{besti,j}^{k} - X_{i,j}^{k})(15) + c_2 \times r_2 \times (G_{besti,j}^{k} - X_{i,j}^{k})  \qquad (15)$$

$$X_{i,j}^{k+1} = X_{i,j}^{k} + V_{i,j}^{k+1}  \qquad (16)$$

Where $P_{besti,j}^{k}$ represent personal best $j^{th}$ component of $i^{th}$ individual, whereas $G_{bestj}^{k}$ represents $j^{th}$ component of the best individual of population up to iteration k. The PSO search mechanism is multidimensional search space as shown in Fig. 6.
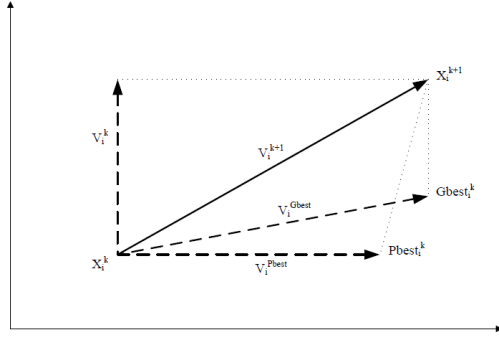
**Figure 6:** PSO mechanism search space

Fig..7 shows the considered steps of PSO technique in flowchart.
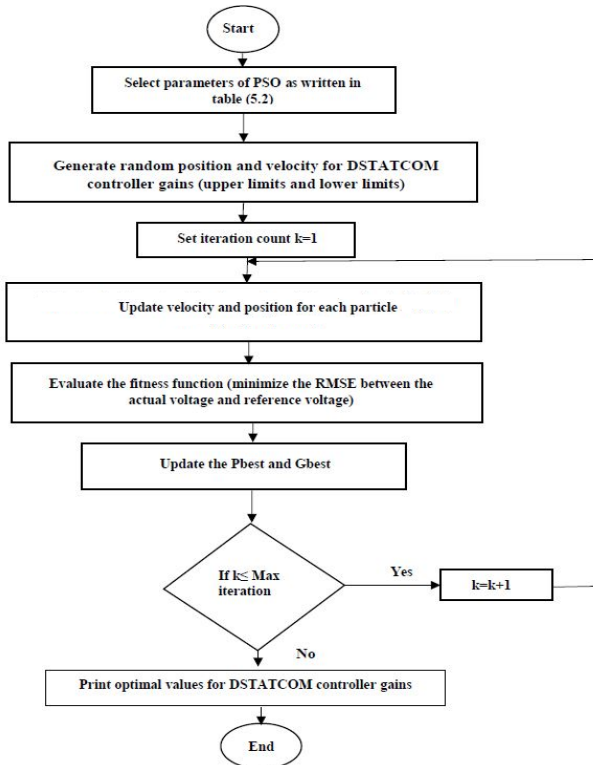


**Figure 7:** Flowchart of PSO algorithm

### B. Artificial Neural Networks (ANNs)

Feed forward ANN is used to tune the controller of DSTATCOM in real time according to distribution bus voltage level. Fig. 8 shows the basic architecture of a feed forward of ANN consist of three layers architecture: input, hidden and output layer respectively. each node (neurons) in one layer is connected to each node in the next layer. The input nodes number in the input layer equals the number of inputs of the system, the number of output nodes in the

output layer is the same number of outputs of the system. The number of hidden nodes in the middle layer is normally between the number of input nodes and the output nodes in the system. The number of hidden nodes is very important since both over fitting and under fitting will affect on the training results [15]-[16].
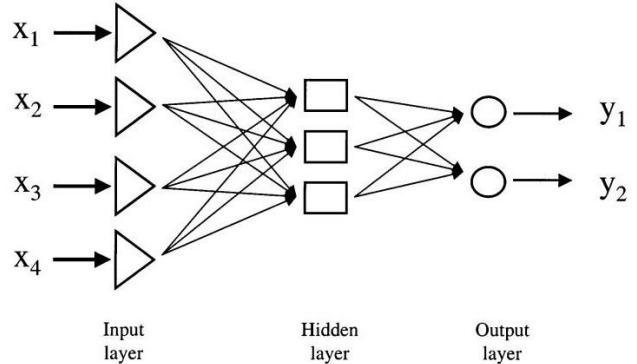


**Figure 8:** Basic neural network structure

The training procedure of the feed forward ANN used in this study is according to the mean square error of output criterion, which can be defined by

$$J = \sum_{1}^{N} e(i)^2 \qquad (17)$$

Where $N$ is the output neurons number, and $e(i)$ is instantaneous error between the actual and estimated value of the output.

The value of each neuron in the hidden layer $(y_j)$ is given in terms of the input values $x_i$ as shown in the following equation

$$y_j = \tanh(\sum w_{ij} x_i + b_j) \qquad (18)$$

### V. METHODOLOGY

#### A. Case Study

The work is applied on real network with data given by Jerusalem District Electricity Company (JDECO). The network is for Abu Mashaal zone in West Bank. The voltage on this network drops below the standard level (11kV) on distribution bus due the industrial nonlinear loads. The single line diagram of the given radial

network is shown in Fig. 8.
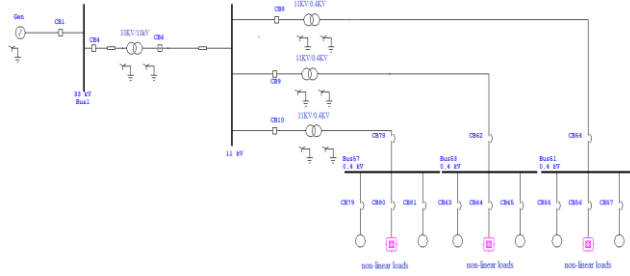


**Figure 9:** Single line diagram for radial network

Description of the system configuration is summarized in Table I.

**Table I**
Description of proposed distribution feeder

| Parameter | Value |
| --- | --- |
| 3 phase ac source | $V_{rm}$=11kV, f=50Hz |
| Line impedance | $L_s$=3.851mH, $R_s$=0.211Ω |
| Distribution transformers | 33kV/11kV, 11kV/0.4kV |

### B. Calculation of DSTATCOM Configurations

Configurations of DSTATCOM are calculated using mathematical equations design given in Eq.11 into Eq.14. The rated load connected on the end user of distribution system is 1MVA, Table II summarize the calculation values of DSTATCOM configuration.

**Table II:**
Values of DSTATCOM configuration

| Parameter | Value |
| --- | --- |
| $I_{rms}$ | 1443.3A |
| $V_{dc}$ | 15556.3V |
| $C_{dc}$ | 16.665mF |
| $L_f$ | 31.42μH |
| $C_r$ | 1.8mF |
| $R_r$ | 0.0027Ω |

### C. MATLAB Model Simulation

Fig. 10 shows the overall power system for given case study with DSTATCOM connecting on 11kV distribution bus.
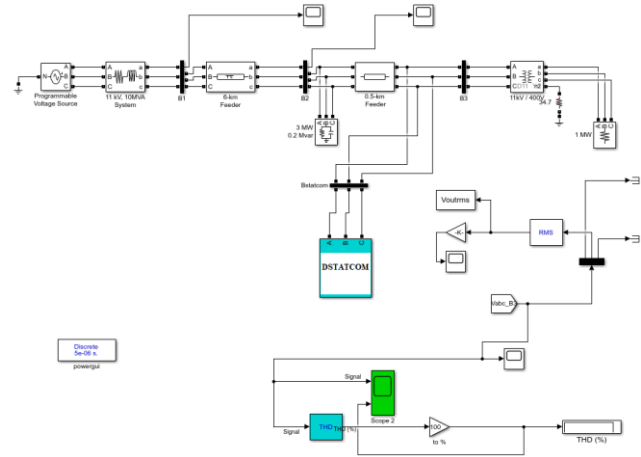


**Figure 10:** MATLAB Simulink simulation

The transfer function of the closed loop control system shown in Fig.11 can be written as

$$Transfer\ function = \frac{Gc(s) + G(s)}{1 + Gc(s) + G(s)} \quad (19)$$
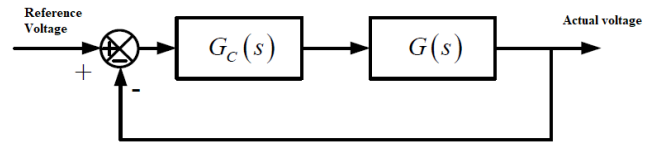


**Figure 11:** Block diagram of closed loop control system.

The Fig. 12 shows the control strategy of DSTATCOM based on PLL.
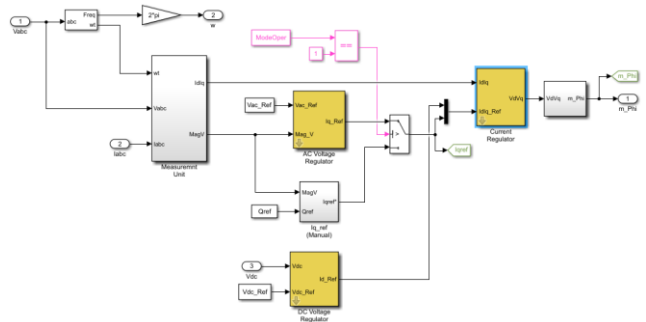


**Figure 12:** Control strategy for DSTATCOM [40]

### D. Tuning DSTATCOM controller using ANNs and PSO

- *Employ PSO for optimum value of controller*

PSO algorithm is applied to find the optimum

controller gains of DSTACOM (Vac regulator, Vdc regulator, and current regulator and PLL regulator). The algorithm parameters are selected as given in Table III.

**Table III.**
Parameters of PSO algorithm

| Parameter | Size |
|---|---|
| Population size | N=50 |
| Accelerated factors | $C_1=1$, $C_2=1.5$ |
| Inertia | w=1.2 |
| Number of iterations | i=100 |
| Upper limits for controller gains | [10 3500 10 20 5 1500 1500 3000] |
| Lower limits for controller gains | [0.01 10 0.0001 0.01 1 100 10 10] |

The objective function is minimization of root mean square error (RMSE) between the actual measured voltage and reference voltage (1pu). The RMSE and the objective function are as given in Eq.20 and Eq.21 respectively

$$RMSE = (\frac{1}{n} \sum_{i=1}^{n} (V_i - V_{ref})^2)^{\frac{1}{2}} \qquad (20)$$

$$J = \min[RMSE] \qquad (21)$$

Where $J$: fitness function, $RMSE$: Root mean square error, $V_i$: actual voltage, $V_{ref}$: reference voltage(1pu), and n: number of samples.

MATLAB code is written for the objective function and the PSO algorithm is running for voltage profile improvement. Sag and swell events are created in order to obtain controller gains for deviation of voltage from 1pu. The simulation is running for every deviation of (0.05pu) from extreme swell to extreme sag. At every case of sag and swell event the percentage error is calculated as well the THD.

• *Employ ANNs for control DSTATCOM*

ANN is proposed as AI method used for controlling DSTATCOM. The environment of ANN controller has made them a wide area of interest among researches in extensive field, due ANN can proficiently learn the unknown continuously varying environment and act accordingly. The results from PSO for wide range of sag and swell events (0.7-1.3) processed and nearly 70% of these data considered as a data base for ANNs training process. Then the results of ANNs provides real time to control DSTATCOM. The learning process of ANN is developed in MATLAB, aided by the toolbox neural network. For this study eight

networks are defined in MATLAB code in order to applied the ANNs algorithm for learning and find the best optimal value of controllers gains according to disturbance voltage level, the networks are defined as shown in Table IV.

**Table IV**
Define networks in ANN algorithm

| ANNs | Controller gain |
|---|---|
| Network1 | $V_{ac}(k_p)$ |
| Network2 | $V_{ac}(k_i)$ |
| Network3 | $V_{dc}(k_p)$ |
| Network4 | $V_{dc}(k_i)$ |
| Network5 | $i(k_p)$ |
| Network6 | $i(k_i)$ |
| Network7 | $PLL(k_p)$ |
| Network8 | $PPL(k_i)$ |

• *Designing and Programming ANNs*

Generally, programming ANNs follow a number of systemic procedures:
▪ Collecting of data from the PSO: the values of $k_p$ and $k_i$ for each case of sag and swell events using PSO.
▪ Data reprocessing in this step the data is normalized.
▪ Building the network.
▪ Training the network.
▪ Testing the network by used the targets output in simulation model.

Fig.13 describe the Basic flowchart for designing ANN Model.
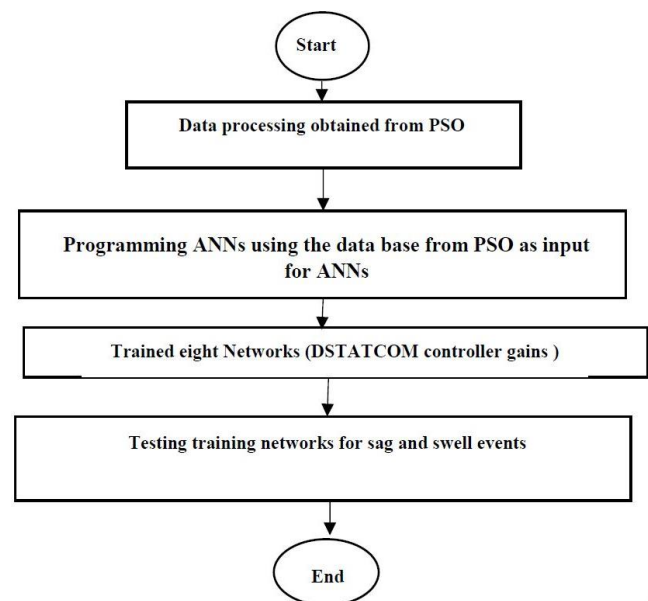


**Figure 13:** Basic flowchart for designing ANNs model

## VI. RESULTS AND DISCUSSION

### A. *Creation of Sag and Swell Events on Distribution Bus*

A wide range of extreme sag (0.7pu) and extreme swell (1.3pu) are created on distributed bus. This may represent the different disturbances occur on distribution system such as faults or over voltage due switching capacitor bank and other electrical disturbance may occur. Fig.s 14 and 15 show the extreme sag and extreme swell respectively.
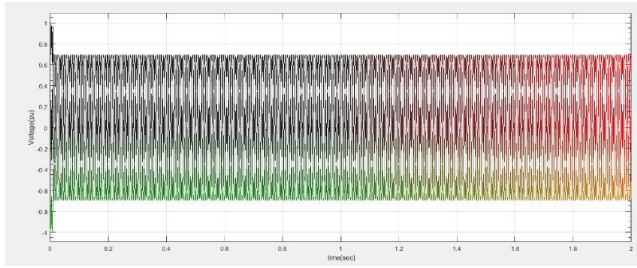


**Figure 14:** Extreme sag event 0.7pu
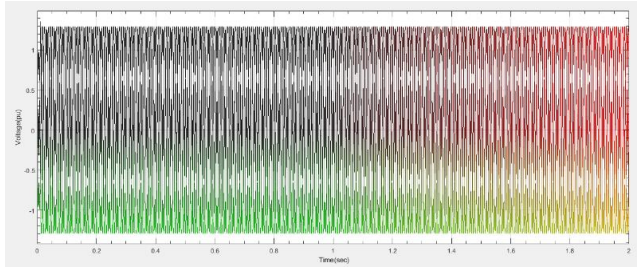


**Figure 15:** Extreme swell event 1.3pu

These events are simulated by network model using MATLAB/Simulink. The deviation of voltage on distribution bus is considered to be around 0.05 pu. DSTATCOM controller gains are obtained for each created event using PSO algorithm as well as the percentage error is also calculated according to the objective function of the optimization function. Table V and Table VI shows the results of DSTATCOM controller gains for the main steps selected from the data base obtained by PSO disturbances of swell and sag voltage events respectively.

**Table V.**
Optimal values of DSTATCOM controller gains during main steps of swell events using PSO

| Event | 1.3pu | 1.25pu | 1.20pu | 1.15pu | 1.10pu |
|---|---|---|---|---|---|
| $V_{ac}(k_p)$ | 10 | 7.43 | 3.82 | 10 | 10 |
| $V_{ac}(k_i)$ | 10 | 3500 | 198 | 10 | 10 |
| $V_{dc}(k_p)$ | 10 | 1e-4 | 6.22 | 10 | 10 |
| $V_{dc}(k_i)$ | 20 | 12.3 | 15.5 | 1e-2 | 20 |
| $i(k_p)$ | 2.75 | 2.17 | 2.05 | 5 | 5 |
| $i(k_i)$ | 415 | 1500 | 436 | 1280 | 1500 |
| $PLL(k_p)$ | 1170 | 1500 | 1380 | 1500 | 1800 |
| $PPL(k_i)$ | 3000 | 10 | 2640 | 3000 | 3000 |
| Error% | 4 | 4.58 | 5.457 | 8.86 | 5.925 |

**Table VI:**
Optimal values of DSTATCOM controller gains during main steps of sag events using PSO

| Event | 0.9pu | 0.85pu | 0.80pu | 0.75pu | 0.70pu |
|---|---|---|---|---|---|
| $V_{ac}(k_p)$ | 1e-2 | 1e-2 | 10 | 10 | 10 |
| $V_{ac}(k_i)$ | 10 | 3500 | 3500 | 3500 | 10 |
| $V_{dc}(k_p)$ | 1e-4 | 10 | 1e-4 | 1e-4 | 1e-4 |
| $V_{dc}(k_i)$ | 1e-2 | 1.67 | 20 | 20 | 20 |
| $i(k_p)$ | 1 | 1 | 5 | 1 | 1 |
| $i(k_i)$ | 100 | 1170 | 701 | 1370 | 100 |
| $PLL(k_p)$ | 2100 | 988 | 1130 | 659 | 25.5 |
| $PPL(k_i)$ | 23.8 | 3000 | 324 | 10 | 10 |
| Error% | 9.98 | 9.55 | 9.14 | 9.17 | 0.99 |

### B. *Selection of Controller Gains Using PSO*

The controller gains of DSTATCOM are selected and optimized according to the objective function which is minimization the RMSE between the measured bus voltage and the reference value (1pu). The sag events via error are drawn as in Fig. 16, while the swell events via error drawn in Fig. 17. From the charts of sag and swell via percentage error, it clear that the worst case of error is below 10% which acceptable referring to IEEE Standards.
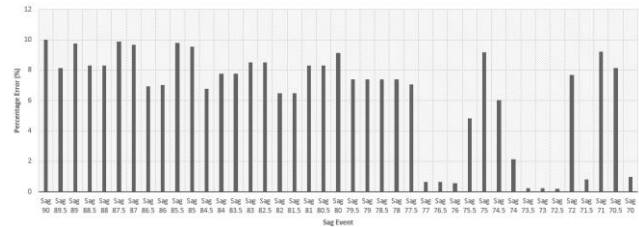


**Figure 16:** Sag events via error%
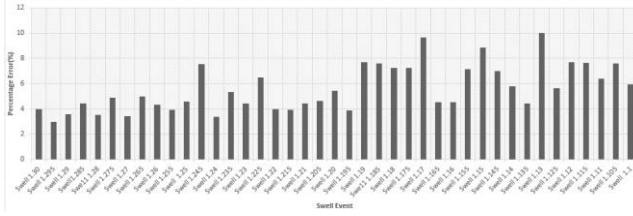
**Figure 17:** Swell events via error%

### C. Control DSTATCOM using ANNs

PSO is used as a tool to obtain the optimum values of controller gains. Then data processing is done and nearly 70% of these data is used to train eight networks that control DSTATCOM as mention in Table 4. Values for controller gains is applied to ANNs in training phase. ANN logarithm is used for practice the controller and select the gains constants according to activations elements. The controller constants are used as inputs to train the eight controller constants networks.

Fig. 18 shows the training, validation, and test errors used to check the progress of training for eight trained networks. Fig. 19 describe the estimation function by the ANN. The regression of output is reported in Table VII. The R value is an indication of the relationship between outputs and targets.
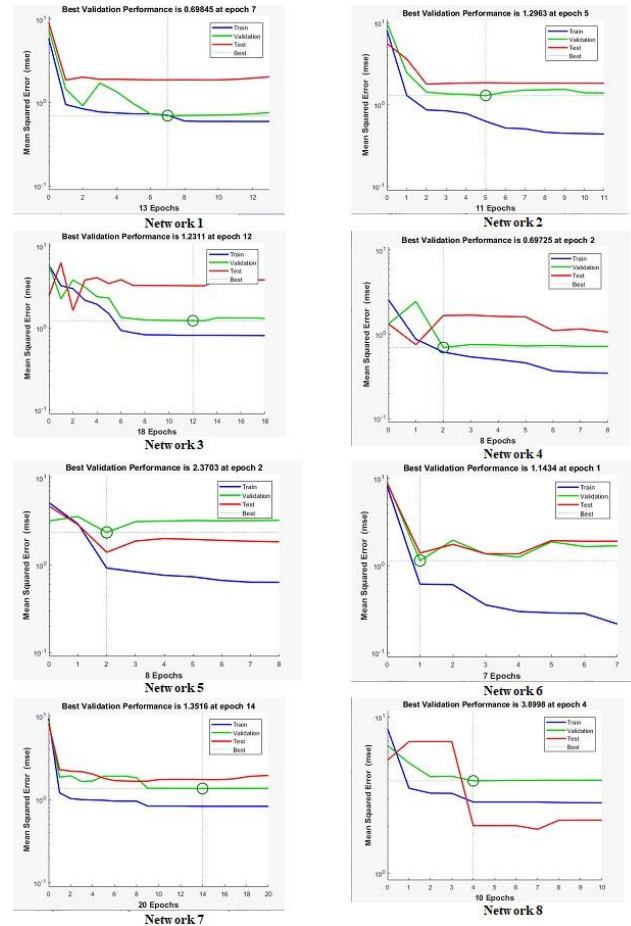


**Figure 18:** Training validation and test curves for neural networks

**Table VII.**
Evaluation of MSE and fitting function R for eight neural networks

| Neural Network | MSE | R |
|---|---|---|
| Network1 | 0.69845 | 0.81662 |
| Network2 | 1.2963 | 0.85723 |
| Network3 | 1.2311 | 0.75731 |
| Network4 | 0.69725 | 0.85287 |
| Network5 | 2.3703 | 0.81662 |
| Network6 | 1.1434 | 0.85723 |
| Network7 | 1.3516 | 0.75731 |
| Network8 | 3.8998 | 0.85287 |
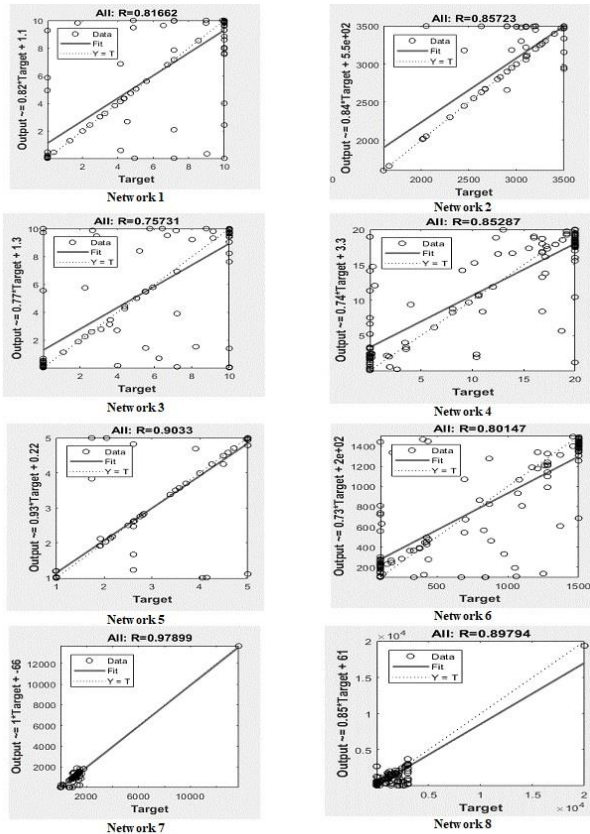
**Figure 19:** Estimation and fitting for neural networks

### D. Effect of ANNs Controller on Performance of DSTATCOM for Improve the Voltage Profile

ANN logarithm is used for practice the controller and select the its gains constants according to activations elements. The algorithm is employed using nearly 70% of data obtained from PSO. Table VIII shows the results and controller gains for extreme swell and extreme sag by using developed controller of DSTATCOM.

**Table VIII:**
Voltage profile improvement using developed DSTATCOM controller

| Event | Voltage profile improvement | THD% |
|---|---|---|
| Extreme swell (1.3pu) | 1.02pu | 3.26 |
| Extreme sag (0.7pu) | 1.07pu | 9.23 |

Fig. 20 shows the effect of DSTATCOM on improving the voltage profile of the system at PCC during voltage swell event with acceptable range according to IEEE Std.1159.
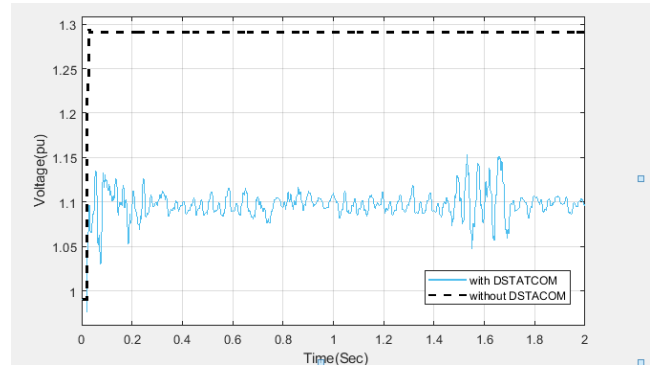


**Figure 19:** Effect of DSTATCOM on Voltage profile during extreme swell event**.**

Fig. 21 shows the effect of DSTATCOM on improving the voltage profile of the system at PCC during voltage sag event with acceptable range according to IEEE Std.1159.
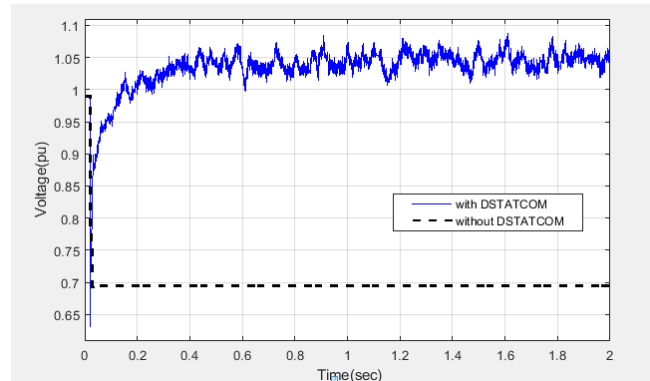


**Figure 20:** Voltage profile improvement for extreme sag event.

The proposed technique ANN with PSO is an effective technique to control DSTATCOM for voltage profile improvement on distribution system for the goal of real time control rather than traditional off line control. Also, the controller is examined for improving the voltage profile for continuous extreme sag and extreme swell, the results proved the robust and efficient of developed controller as shown in Fig.s 22 and 23 for rms voltage and phase voltage respectively.
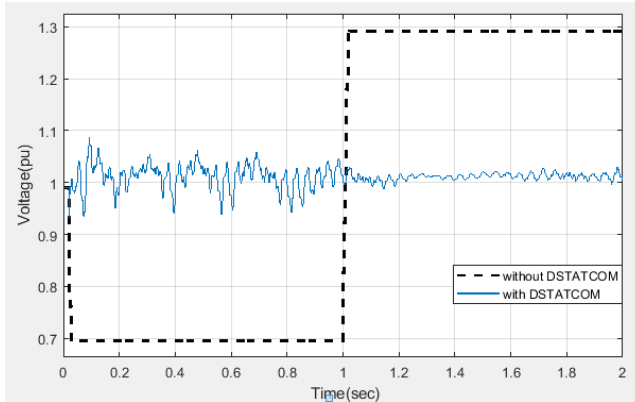
**Figure 21:** Effect of developed DSTATCOM controller using AI on rms voltage profile**.**
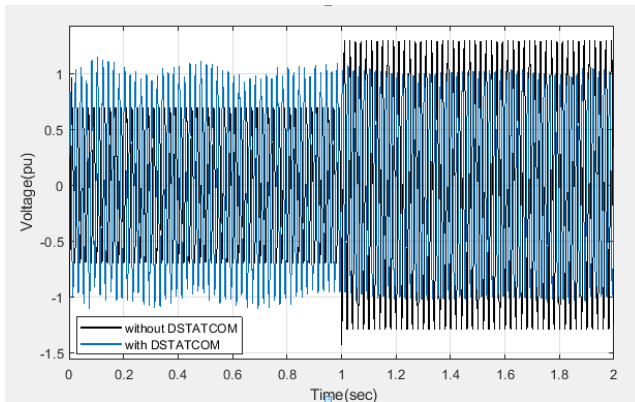


**Figure 22:** Effect of developed DSTATCOM controller using AI on instantaneous voltage profile**.**

## VII. CONCLUSIONS

The results proved the importance of using AI in controller design of DSTATCOM, the voltage profile is improved during voltage events mainly sag and swell events in real time. The PSO is used as a tool for obtained the optimum values of DSTATCOM controller gains and then ANN is used as AI technique for real time control of DSTATCOM. The work proved the efficient of using ANN as AI technique for tuning PI controller of DSTATCOM in order to improve the voltage profile on distribution system. The DSTATCOM with developed controller validated the importance of AI methods such as ANN. Using such this developed controller may increase stability and reliability of power system and hence the network converts to smart network. Developed controller using ANN supports DSTATCOM with robust tuning system, since its responds to different real time voltage

disturbances that may occur in distribution system with efficient enhancement for voltage profile compared with conventional control strategies. The simulation results proved the efficient of suggested method for controlling DSTATCOM in order to improve voltage profile on distribution system.

## CONFLICTS OF INTEREST

There is no conflict of interest.

## RESEARCH AND PUBLICATION ETHICS

The authors declare that this article does not require ethics committee approval or any special permission.

## REFERENCES

[1] Saafin Z, Zaro F, Jawadeh M. Voltage Profile Improvement Using DSTATCOM Based on Artificial Intelligent Techniques. *IEEE Jordan International Joint Conference on Electrical Engineering and Information Technology (JEEIT)*, 2019,*773-778*, doi: 10.1109/JEEIT.2019.8717452.

[2] Sharaf A, Gandoman F. A switched hybrid filter-DVS/green plug for smart grid nonlinear loads. *Smart Energy Grid Engineering (SEGE)*, 2015, 1-6, doi: 10.1109/SEGE.2015.7324588

[3] Short, T. Distribution reliability and power quality. United States: Crc Press, 2005.

[4] Zaro F, Abido M. Real-Time Detection and Classification of Power Quality Problems Based on Wavelet Transform. *Jordan Journal of Electrical Engineering,* 2019, *5(4),* 222-242.

[5] Ipinnimo, Chowdhury, O, Chowdhury, S, Mitra, J. A review of voltage dip mitigation techniques with distributed generation in electricity networks. *Electric Power Systems Research,* 2013, *103,* 28-36, https://doi.org/10.1016/j.epsr.2013.05.004.

[6] Rana A, Trivedi I, Vasoya C, Pandya M, Gohil S, Saradva P. Application of D-STATCOM for power quality improvement in distribution line. *International Conference on Computation of Power, Energy Information and Commuincation, Chennai*, 2016, 719-725, doi: 10.1109/ICCPEIC.2016.7557315.

[7] Bhim S, Sabha R, Pankajkumar V. An implementation of double-frequency oscillation cancellation technique in control of DSTATCOM. *International Transactions*

*on Electrical Energy Systems,* 2013, *24(6)*: 796-807, doi.org/10.1002/etep.1735

[8] Liu C, Hsu Y. Design of a self-tuning PI controller for a STATCOM using particle swarm optimization. *IEEE Transactions on industrial Electronics,* 2010, *57(2)*: 702-715, doi: 10.1109/TIE.2009.2028350.

[9] Kamaraj P, Thamizharasu T, M V. Voltage regulation of soft switched interleaved boost converter using fuzzy proportional integral controller. *Journal of Energy Systems*. 2020; *4(4)*: 145-160. https://doi.org/10.30521/jes.762506

[10] Alqam S, Zaro F. Power Quality Detection and Classification Using S-Transform and Rule-Based Decision Tree. *International Journal of Electrical and Electronic Engineering & Telecommunications,* 2019, *8(1)*: 45-50, doi: 10.18178/ijeetc.8.1.45-50

[11] Labeeb M, Lathika B. Design and analysis of DSTATCOM using SRFT and ANN-fuzzy based control for power quality improvement. *IEEE Recent Advances in Intelligent Computational Systems, Trivandrum, Kerala,* 2011, 274-279, doi: 10.1109/RAICS.2011.6069317.

[12] Nabisha A, Joseph X. Power Quality Enriched Wind Energy System using DSTATCOM based on PID-ANN Controller. *American-Eurasian Journal of Scientific Research,* 2017*, 12(5)*: 271-284, doi: 10.5829/idosi.aejsr.2017.271.284.

[13] Babaei M, Jafari-Marandi M, Abdelwahed S, Smith B. A simulated Annealing-based optimal design of STATCOM under unbalanced conditions and faults. *Power and Energy Conference at Illinois (PECI),* 2017, 1-5, doi: 10.1109/PECI.2017.7935768.

[14] Zaro F. True Multi-Objective Optimal Power Flow in a Deregulated Environment Using Intelligent Technique. *Journal of Engineering Research and Technology*, 2017, *3(4)*: 110-118.

[15] Panda S, Padhy N. Comparison of particle swarm optimization and genetic algorithm for FACTS-based controller design. *Applied soft computing,* 2008, *8(4)*: 1418-1427.

[16] Beşikçi E, Arslan O, Turan O, Ölçer A. An artificial neural network-based decision support system for energy efficient ship operations. *Computers & Operations Research,* 2016, *66*: 393-401, https://doi.org/10.1016/j.cor.2015.04.004.

[17] Samadianfard S, Jarhan S, Sadri Nahand H. Application of support vector regression integrated with firefly optimization algorithm for predicting global solar radiation. *Journal of Energy Systems*. 2018; *2(4)*: 180-189. https://doi.org/10.30521/jes.458328

RESEARCH ARTICLE

# Examination of The Weld Defects in The Inner-City Natural Gas Pipes with Non-Destructive and Destructive Testing Methods

* [iD]Hamit Adin, [1] [iD]Adnan Doğan, and [2] [iD]Mehmet Şükrü Adin

*Batman University, Department of Mechanical Engineering, Batman, Turkey. hamit.adin@batman.edu.tr orcid.0000-0003-2455-967X,
[1] Batman University, Department of Mechanical Engineering, Batman, Turkey. adnandogan2019@hotmail.com orcid.0000-0003-1202-5152,
[2] Batman University, Department of Mechanical Engineering, Batman, Turkey. mehmetsukru.adin@batman.edu.tr orcid.0000-0002-2307-9669

## HIGHLIGHTS

- *Radiography, tensile test and 3 different electrodes were used in the study*
- *As a result of the radiographic examinations, it has been determined that there are many defects in the welded joints.*
- *It has been found that the optimal electrode for joint welding is the T2-Pure electrode*

## GRAPHICAL ABSTRACT

Controls made during the production and assembly of natural gas pipelines are very important in terms of quality, human, environmental safety and security. For this reason, in our study, the joining welds of natural gas pipelines used in the city of Mardin were examined with a non-destructive method according to API 1104 standard. Radiographic pictures of the welded joints of the API 5L X42 standard steel pipes used in the natural gas pipeline for non-destructive testing were taken, defects were detected and solutions were tried to be developed. In addition, as part of the study, destructive tests were carried out with welded tensile samples taken from pipes. As a result of the tensile tests, it was seen that the optimal electrode for joint welding is T2-Pure electrode. The graphical abstract of the article is shown in Figure A.
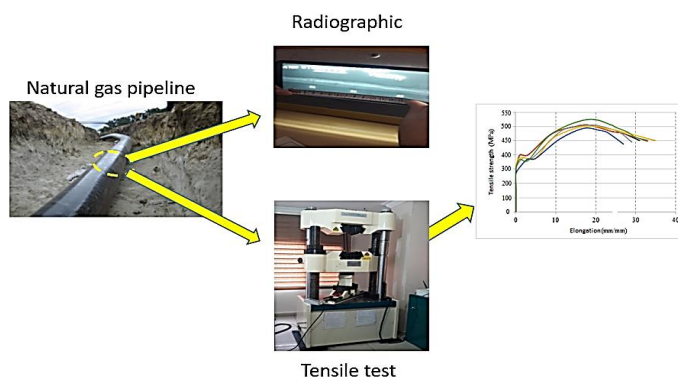
**Figure A.** Graphical work flow of the proposed study.

**Aim of Article:** *To examine the welding defects in natural gas pipelines as destructive and non-destructive.*

**Material and Method:** *Radiography, tensile test and 3 different electrodes were used in the study.*

**Findings and Results:** *According to API 1104 standard, defects occurring in welded joints in the pipeline were examined radiographically. In the radiographic examinations, defects were detected in the joint welding.*

**Conclusion:** *As a result of the radiographic examinations, it was determined that the defects in the joining weld were caused by the electrode used. In addition, as part of the study, destructive tests were carried out with welded tensile samples taken from pipes. As a result of the tensile tests, it was seen that the optimal electrode for joint welding is T2-Pure electrode.*

ARAŞTIRMA MAKALESİ / RESEARCH ARTICLE

# Şehir İçi Doğalgaz Borularındaki Kaynak Hatalarının Tahribatsız ve Tahribatlı Muayene Yöntemleri ile İncelenmesi

* [ID] Hamit Adin, [1] [ID] Adnan Doğan, [2] [ID] Mehmet Şükrü Adin

* Batman Üniversitesi, Makine Mühendisliği Bölümü, Batman, Türkiye. hamit.adin@batman.edu.tr  orcid.0000-0003-2455-967X,
[1] Batman Üniversitesi, Makine Mühendisliği Bölümü, Batman, Türkiye. adnandogan2019@hotmail.com  orcid.0000-0003-1202-5152,
[2] Batman Üniversitesi, Makine Mühendisliği Bölümü, Batman, Türkiye. mehmetsukru.adin@batman.edu.tr orcid.0000-0002-2307-9669

## ÖNE ÇIKANLAR / HIGHLIGHTS

- *Çalışmada radyografi, çekme testi ve 3 farklı elektrot kullanılmıştır*
- *Radyografik incelemeler sonucunda kaynaklı birleşim yerlerinde birçok hata olduğu tespit edilmiştir.*
- *Bağlantı kaynağı için en uygun elektrotun T2-Saf elektrotu olduğu bulunmuştur*

| **Makale Bilgileri** / Article Info / | **ÖZET** / ABSTRACT |
|---|---|
| | *Doğalgaz boru hatlarının imalat ve montajı aşamasında yapılan kontroller kalite, insan, çevre güvenliği ve emniyet bakımından çok önemlidir. Bu nedenle çalışmamızda, Mardin ili şehir içinde kullanılan doğalgaz boru hatlarının birleştirme kaynakları API 1104 standardına göre tahribatsız yöntemle muayene edilmiştir. Tahribatsız muayene için doğalgaz boru hattında kullanılan API 5L X42 standardındaki çelik boruların kaynaklı birleşme yerlerinin radyografik resimleri çekilerek hataları tespit edilmiş ve çözümler geliştirilmeye çalışılmıştır. Ayrıca, çalışma kapsamında borulardan alınan kaynaklı çekme numuneleri ile tahribatlı deneyler de yapılmıştır. Çekme deneyleri sonucunda, birleştirme kaynağı için en uygun elektrotun T2-saf elektrotu olduğu görülmüştür.*<br><br>**Anahtar Kelimeler:** *Doğalgaz boruları, API 5L X42, Kaynak hataları, API 1104, Tahribatsız muayene, Radyografik muayene* |

## I. GİRİŞ [INTRODUCTION]

Dünya genelinde artan doğalgaz kullanımı, arz ve talep merkezlerinin çeşitli taşıma türleri ile birbirine bağlanmalarını zorunlu kılmaktadır. Kara ve deniz yolu taşımacılıklarına kıyasla boru hatları ile doğalgaz taşımacılığı, daha yüksek taşıma hızı yanında daha güvenilir, kaliteli, çevreci ve atmosfer koşullarından etkilenmemesi sebebiyle üstünlükleri vardır. Bu nedenlerden dolayı doğal gaz, gelişen teknolojinin de yardımıyla, üretim merkezlerinden tüketim bölgelerine en ekonomik şekilde boru hatları vasıtasıyla taşınmaktadır

[1-4]. Ekonomik ve stratejik olarak önemli bir yeri olan doğalgazın, üretimi yapılan yerlerden son kullanılacak yere kadar taşınmaları dikkatle yürütülmesi gereken bir işlemdir.  Yüksek basınçlarda ve genellikle de çelik borularla bu işlem yapılmaktadır [5-7]. Taşıma işlemini yapacak olan bu boruların her türlü dış etkenlerden korunacak şekilde, yüksek mekanik özelliklere sahip olmaları gerekmektedir [3, 7, 8]. Bu yüzden, petrol ve doğalgazı taşıyan çelik borular, genel olarak API (American Petroleum Institue) 5L standardına uygun olarak üretimi sağlanmaktadır. API 5L standardında üretilen çelikler, düşük alaşımlı ve yüksek mukavemetli

çelik serileridirler [9-11]. API 5L standardı, A, B ve X kalite gruplarından oluşmaktadır. Bu kalite gruplarında, A kalite sınıfı 210 MPa (30500 Psi), B kalite sınıfı ise 245 Mpa (35500 Psi) minimum akma mukavemetini ifade etmektedir. X kalite sınıfına baktığımızda ise örneğin X42, 42100 Psi (290 MPa) minimum akma mukavemetini ifade etmektedir. Ayrıca, API 5L standardında üretilen borular, dikişsiz veya dikişli çelik borular olarak imal edilirler [12, 13]. Çelik sınıflarına göre API 5L standardında boru imalat metotları Tablo 1'de verilmiştir [14].

**Tablo 1.** Çelik sınıflarına göre API 5L standardında boru imalat metotları [14].

| Kullanılan kaynak tekniklerine göre boru imalat metodu | Çelik Sınıfı (Standart gösterim) | | |
|---|---|---|---|
| | A 25 | A ve B | X42 – X80 |
| Dikişsiz | ✓ | ✓ | ✓ |
| Dikişli (Boyuna ve spiral) | | | |
| Boyuna dikişli | | | |
| Alın kaynaklı | ✓ | | |
| Örtülü elektrotlu ark kaynaklı | ✓ | ✓ | ✓ |
| Toz altı ark kaynaklı | | ✓ | ✓ |
| Gaz metal ark kaynaklı | | ✓ | ✓ |
| Gaz metal ark ve toz altı ark kaynaklı | | | ✓ |
| Çift dikişli* | | ✓ | ✓ |
| Spiral dikişli** | | | |
| Spiral toz altı ark kaynaklı | | ✓ | ✓ |
| (*) Çift dikişli borular 914,4 mm ve daha büyük dış çaplar ile sınırlandırılmıştır. (**) Spiral dikişli borular 114,3 mm ve daha büyük dış çaplar ile sınırlandırılmışlardır. | | | |

Çelik sınıflarına göre API 5L standardında imal edilen çelik boruların mekanik özellikleri ise Tablo 2'de verilmiştir [15].

**Tablo 2.** API 5L standardına göre boruların mekanik özellikleri [15].

| Çelik Sınıfı | Minimum akma mukavemeti | | Minimum çekme mukavemeti | |
|---|---|---|---|---|
| | MPa | Psi | MPa | Psi |
| A 25 | 175 | 25400 | 310 | 45000 |
| A | 210 | 30500 | 335 | 48600 |
| B | 245 | 35500 | 415 | 60200 |
| X 42 | 290 | 42100 | 415 | 60200 |
| X 46 | 320 | 46400 | 435 | 63100 |
| X 52 | 360 | 52200 | 460 | 66700 |
| X 56 | 390 | 56600 | 490 | 71100 |
| X 60 | 415 | 60200 | 520 | 75400 |
| X 65 | 450 | 65300 | 535 | 77600 |
| X 70 | 485 | 70300 | 570 | 82700 |

Doğalgaz boruları genel olarak kaynak yapılarak birleştirildiğinden kaynaklı birleştirilmenin kalitesi önem arz etmektedir. Bu yüzden, kaynakla yapılan birleştirmelerde, istenilen mekanik özelliklere ulaşabilmek için kullanılan elektrotun uygunluğu çok önemlidir [16]. Ayrıca, kullanılan elektrotun uygunluğu ile birlikte kaynak yapan operatörün uzmanlığı da kaynak kalitesini oldukça artırmaktadır. Bu sayede, kaynak bölgesinde oluşabilecek olan cüruf, enine çatlaklar, eksik doldurulmuş oluk, aşırı kök nüfuziyeti, kök nüfuziyet eksikliği, erime eksikliği ve gözenekli yapı gibi kaynak bölgesi hataları en aza indirilmektedir [17].

Gelişen teknolojiyle birlikte imal edilen ürünlerin kalite ve güvenirliği de büyük bir önem kazanmaktadır. Bu yüzden, kalite ve güvenirliliğin sağlanması bakımından, üretilen ürüne herhangi bir zarar vermeden tahribatsız olarak muayene ilgi çekmektedir. Tahribatsız olarak yapılan muayene yöntemiyle, imal edilen ürünlerdeki hatalar kullanımdan önce tespit edilmiş olunmaktadır [18-20].

Tahribatsız muayene işlemlerinden olan radyografi testi, petrol ve doğalgaz taşıyan borulara yapılan birleştirme kaynağının uygunluğunu kontrol etmek amacıyla sıklıkla kullanılmaktadır. Bu yöntemin kaynak hatalarını

belirlemekte başarılı olduğu bilinmektedir [18, 20]. Çalışmamızda, Mardin İli şehir içi doğalgaz boru hatlarının birleştirilmesi için kullanılan kaynaktaki hataların tespiti amacıyla radyografik incelemeler yapılmıştır. İncelemeler için X ışını ve gama ışını cihazları kullanılarak boruların çok sayıda radyografik filmi çekilmiş ve kaynaklı birleştirmelerin kusurları bulunmuştur.

Çalışmalarda, bulunan kusurların giderilmesi için spiral dikişli API 5L standardında üretilen X42 çelik doğalgaz boruları 3 farklı elektrotla yeniden kaynak edilmiş ve kaynak birleştirme noktalarından elde edilen numunelere çekme testleri uygulanarak en uygun kaynak elektrodu tespit edilmeye çalışılmıştır.

## II. MATERYAL VE METOD [MATERIAL AND METHOD]

Çalışmada, Mardin İli sınırları içerisinde yer alan yaklaşık 7 km uzunluğunda, API 5L X42 kalitesinde, 8 inç ve 4,8 mm et kalınlığındaki doğalgaz borularının kaynak yerleri tahribatsız (Radyografik) muayene yöntemi ile incelenmiştir. Muayeneler esnasında, radyografik filmlerle tespit edilen kaynak hatalarının yerleri işaretlenmiştir. İşaretlenen hatalı kaynaklar mekanik olarak taşlama yapılarak temizlenmeye çalışılmıştır. Temizle işleminin yapılamadığı durumlarda ise kaynak bölgesi kesilerek boruların üzerinde yeniden kaynak ağzı açılmıştır. X42 çelik boruların kaynak ağzı "V" şeklinde ve 60° açılı olarak açılmıştır. Boruların kaynak ağzı başarılı bir kaynağın olması için her türlü pas, boya vb. şeylerden temizlenmiştir. Açık ve kapalı alanda kullanıma uygun olması ve doğalgaz borularının kaynaklı birleştirilmelerinde sıklıkla kullanılması sebebiyle örtülü elektrotla elektrik ark kaynak metodu kullanılmıştır [18]. Kaynak işlemi için kullanılan elektrotun çapı 2,5 mm olarak seçilmiştir. Boru kaynağında uygulanan pasolar, et kalınlığı 4 mm'den büyük olması sebebiyle 5 paso olarak

(kök, sıcak, dolgu, dolgu ve kapak şeklinde) yapılmış olup Kök pasoda 110 Amper ve 25 Volt, diğer pasolarda ise 290 Amper ve 30 Volt cihaz değerleri kullanılmıştır. Kaynak işlemi yukarıdan aşağıya olacak şekilde yapılmıştır. Boruların hizaları çok hassas şekilde sabitleyici aparatlarla yapılmıştır. Kullanılan elektrotlar, sadece kullanım aşamasında kutularından çıkarılmış olup dış etkilerden (yağmur, nem vb.) korunmasına dikkat edilmiştir. Bu amaç için portatif bir kulübe kullanılmıştır. Aynı şekilde, operatörler içinde portatif bir kulübe kullanılmıştır. Doğru sonuçların elde edilmesi amacıyla tüm kaynak işlemleri saha koşullarında yapılmıştır. Hatalı kaynak yapılan doğalgaz borularının kaynak yerleri taşlama yapılarak temizlendikten sonra 17 takım halinde ve 3 farklı (sırasıyla, E42 2C 21, T1-Saf ve T2-Saf elektrotları kullanılarak) elektrotla tekrar kaynak edilmiştir. Çalışmanın deneysel sonuçlar ve tartışma bölümünde, T1-Saf ve T2-Saf elektrotlarının ihtiyaçlara göre E42 2C 21 elektrodu (AWS A5.1 E6010) üzerinde kimyasal değişiklikle nasıl elde edildiği belirtilmiştir. Farklı elektrotlarla kaynak edilen bu takımların kaynak bölgelerinin yeniden radyografik filmleri çekilmiştir. Böylece, kaynak hataları varsa tespit edilerek sorunlar giderilmiştir. Tüm kaynak işlemleri API 1104 standartlarına uygun kaynak yapabilen sertifikalı uzman teknisyenler tarafından yapılmıştır. Hataları giderilen X42 çeliğinden yapılmış boruların kaynaklı birleştirme yerlerinden, kaynaklı birleştirmeyi yapmaya en uygun elektrotun tespiti amacıyla, numuneler alınarak mukavemetlerini ölçmek amacıyla çekme testi (tahribatlı) uygulanmıştır. Çekme deneyleri sonucunda, en yüksek çekme mukavemetini sağlayan elektrotun doğalgaz borularının birleştirilmeleri için kullanılması sağlanmıştır. Çalışmamız kapsamında kullanılan ve API standartlarına göre imal edilen X42 kalitesindeki çelikler, doğalgaz boru hatları olarak sıklıkla kullanılan, yüksek mukavemetli, düşük alaşımlı ve ince taneli doğalgaz borularıdır [9-11, 21, 22]. Çalışmada kullanılan X42 çeliğinin kimyasal bileşimi Tablo 3'te verilmiştir.

**Tablo 3.** X42 çeliğinin kimyasal bileşimi.

| Malzeme | Kimyasal Bileşim (%) | | | | | | | | | | | | | |
|---|---|---|---|---|---|---|---|---|---|---|---|---|---|---|
| | C | Si | Mn | P | S | Cr | Ni | Cu | Mo | Ti | Nb | V | B | Fe |
| X42 | 0,26 | 0,45 | 1,30 | 0,03 | 0,03 | 0,50 | 0,50 | 0,50 | 0,15 | 0,04 | 0,05 | 0,005 | 10 | Kalan |
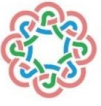
**Tablo 4.** Elektrotların kimyasal bileşimi.

| Elektrot | Kimyasal Bileşim (%) | | | | |
|---|---|---|---|---|---|
| | C | Si | Mn | Mo | Ni |
| E42 2C 21 | 0,08 | 0,2 | 0,6 | - | - |
| T1-Saf | 0,08 | 0,2 | 0,6 | 0,002 | 0,035 |
| T2-Saf | 0,08 | 0,2 | 1,1 | 0,008 | 0,048 |

Deneysel çalışmada kullanılan elektrotların kimyasal özellikleri Tablo 4'te verilmiştir.

## 2.1. Radyografik muayene

Kaynak yapılarak birleştirilen doğalgaz borularının, tahribatsız muayene yöntemlerinden radyografik incelemeleri (Kodak T200 film tipi) ile boru hattındaki birleştirme dikişlerinde meydana gelen hatalar uzman bir teknik personel tarafından API 1104 standardına göre tespit edilmiştir. Böylece kaynak hataları giderilmiştir. Radyografik incelemelerde, en yaygın görülen kaynak bölgesi hataları Şekil 1'de verilmiştir [23].
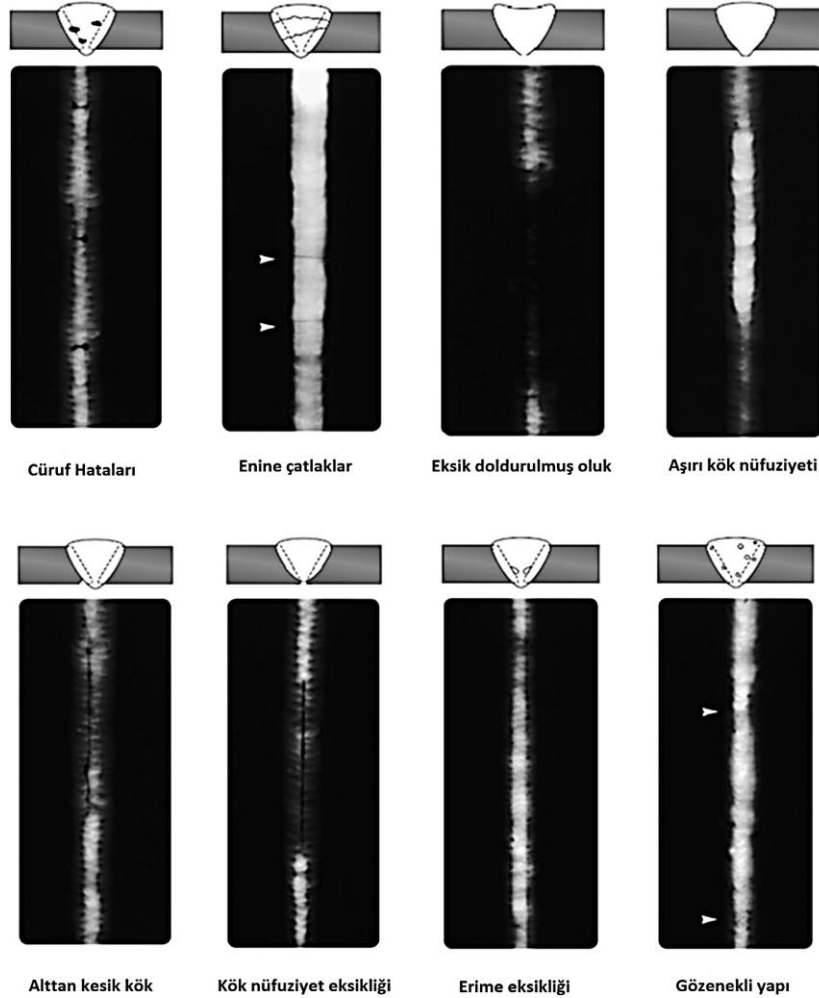


**Şekil 1.** Radyografik incelemelerde en yaygın görülen kaynak bölgesi hataları [23].

API 1104 standardına göre hataların değerlendirilmesi aşağıda belirtildiği gibidir [24].

- Bir gözeneğin çapı 1,5 mm'yi geçmemelidir.
- Kaynak dikişindeki herhangi bir çatlak hiçbir şekilde kabul edilemez ve bu dikişlerin hemen sökülüp tamir edilmesi gerekir.
- Yan cidarı kaynamama ve yetersiz nüfuziyet de boruların kaynağında müsaade edilmeyen hatalardır.
- Kök paso taşkınlığının (şişkinliğinin) 2 mm'ye kadar olanı kabul edilir.
- Kök pasonun içbükey olması halinde (çevre dikişinin yarısına kadar olması şartıyla) en çok cidar kalınlığının %10'una kadar mevcut bir içbükeylik kabul edilir.
- Rastgele dağılmış bulunan bir cüruf kalıntısının genişliği en fazla 3 mm olabilir. Komşu kalıntının da en az 50 mm uzakta olması gerekir.

## 2.2. Çekme deneyi

Mekanik olarak yapılan çekme deneylerinde, kaynak birleştirme noktalarından elde edilen ve API standardına göre hazırlanan numuneler kullanılmıştır. Çekme deneyleri 60 ton kapasiteli Laryee 600 LX isimli çekme cihazı ile oda sıcaklığında, %50 nemde yapılmıştır. Bütün çekme deneyleri 5 mm x dk$^{-1}$ çekme hızında gerçekleştirilmiştir. Çekme deneyleri sayesinde, kaynak yapılan doğalgaz borusunun dikişlerinin mukavemeti ve % uzaması değerlerinin bulunması sağlanmıştır. Bulunan bu değerlerin birbiriyle karşılaştırması ile kaynak bölgesine uygulanan elektrotun uygun olup olmadığı saptanmıştır.

Deneysel çalışma için doğalgaz borularının kaynak yapılmış kısımlarından alınan numuneler API standardına göre mm olarak 4,8x25x500 ölçülerinde hazırlanarak Laryee 600 LX isimli çekme cihazı ile otomatik şekilde, kopma meydana gelene kadar çekme işlemine devam edilmiştir. Çekme deneylerinde kaynağın mukavemeti ölçüldüğünden, kaynak yapılan bölgeye dik olacak şekilde çekme yükü uygulanmıştır. Çekme testinde, 17 deney takımının her birinden 3'er numune alınarak (Toplamda 51 adet) ortalama değerleri bulunmuştur. Çekme deneyi için hazırlanan bir numune Şekil 2'de gösterilmiştir.



**Şekil 2.** Çekme deneyi numunesi.

## III. DENEYSEL SONUÇLAR VE TARTIŞMA [EXPERIMENTAL RESULTS AND DISCUSSION]

### 3.1. Radyografik sonuçlar

API 1104 standardına göre, boru hattındaki kaynaklı birleştirmelerde meydana gelen hataların radyografik incelemeleri uzman bir teknik personel tarafından kontrol edilmiş olup tespit edilen bazı kaynak hatalarının fotoğrafları Şekil 3'te verilmiştir. Şekil 3'ten de anlaşıldığı gibi, 1. takım radyografik filmi incelendiğinde, 1 adet 4 cm uzunluğunda cüruf hatası ve 3 cm uzunluğunda kapak kaynağında düşüklük olduğu yani kapak pasosunun tamamlanmadığı gözlenmiştir. Tespit edilen bu kaynak hatasının giderilmesi amacıyla, mekanik olarak kaynak bölgesi temizlenerek tekrar kaynak yapılmış ve hata giderilmiştir.

**Şekil 3.** Radyografik incelemelerde tespit edilen bazı hataların fotoğrafları.

Şekil 3'te bulunan 3. takımın radyografik filmi incelendiğinde, kaynak dikişi boyunca yanma olduğu görülmektedir.

Kaynak yapılırken, kaynak operatörünün amperi yüksek tutması sebebiyle kaynakta 5,5 cm uzunluğunda yanma oluştuğu anlaşılmıştır. Tespit edilen bu kaynak hatası, kaynaklı bölge mekanik olarak temizlendikten sonra yeniden kaynak yapılmıştır. Şekil 3'te verilen 5. Takımın radyografik filmi incelendiğinde, 10-20 cm aralığında 3 tane küçük gaz boşluğu olduğu ve kapakta yanma oluştuğu görülmektedir. 10-20 cm aralığında bulunan hatalı kaynak mekanik olarak temizlendikten sonra yeniden kaynak yapılarak hata giderilmiştir. Şekil 3'te bulunan 7. takımın radyografik filmi incelendiğinde, 30-35 cm aralığında cüruf sıkışması olduğu, ayrıca 35-40 cm arasında ise kapakta düşüklük olduğu gözlemlenmiştir. Belirlenen hatalı bölge temizlenerek tekrar kaynak yapılmış ve kapaktaki düşüklük böylece giderilmiştir. Şekil 3'te bulunan 9. takımın radyografik filmi incelendiğinde, 10-15 cm aralığında az da olsa kaynak erime eksikliği olduğu görülmektedir. Belirlenen hatalı bölge temizlenerek tekrar kaynak yapılmıştır. Şekil 3'te bulunan 11. takımın radyografik filmi incelendiğinde, 52-53 cm aralığında küçük gaz boşluklarının olduğu ve kök pasoda (boru ağzında yığılmanın) olduğu görülmüştür. Belirlenen hatalı bölgedeki kaynak temizlendikten sonra düzgün bir şekilde yeniden kaynak yapılarak hata giderilmiştir. Şekil 3'te bulunan 13. takımın radyografik filmi incelendiğinde, 45. cm hizasında kaynak bölgesinde kayma olduğu tespit edilmiş ve bölge temizlenip düzeltildikten sonra yeniden kaynak yapılarak hata giderilmiştir. Şekil 3'te bulunan 15. takımın radyografik filmi incelendiğinde, kaynak yapılan bölgede küçük bir cüruf kalıntısı tespit edilmiştir. Belirlenen bu cüruf kalıntısının bulunduğu kaynak bölgesi temizlendikten sonra yeniden kaynak yapılarak hata giderilmiştir.

### 3.2. Çekme deneyi sonuçları

3 farklı elektrotla birleştirilen doğalgaz borularının kaynak bölgesinden elde edilen 17 deney takımındaki (her takımda 3'er numune) toplam 51 numuneye çekme testi uygulanmıştır. API standardına göre hazırlanan numunelerin çekme testinden elde edilen verilerle hangi elektrotun doğalgaz borularını birleştirmeye en uygun olduğu tespit edilmiştir.

E42 2C 21 elektrotu ile birleştirme kaynağı yapılan X42 çelik doğalgaz borularından alınan 1.takım numunelerine çekme testi uygulanmış olup akma ve çekme mukavemetleri ile kopmanın olduğu bölge Tablo 5'te belirtilmiştir.

**Tablo 5.** X42 çeliğin ve 1.takımın akma ve çekme mukavemeti değerleri.

| Numune | Akma (MPa) | Çekme (MPa) | Hasar Bölgesi |
|--------|-----------|-------------|---------------|
| X42 çeliği | 372,70 | 499,2 | - |
| 1.Takım | 362,46 | 452,6 | Kaynak |

Tablo 5'teki akma ve çekme mukavemeti değerleri incelendiğinde, X42 çeliğinin akma mukavemeti 372,7 MPa, çekme mukavemeti ise 499,2 MPa olduğu görülmüştür. Bu değerler 1.takımın 362,46 MPa olan akma mukavemeti ve 452,6 MPa olan çekme mukavemeti ile kıyaslandığında, E42 2C 21 elektrotunun birleştirmeye yeterli katkıyı sağlayamadığı açık şekilde görülmektedir. Ayrıca, kopmanın kaynak bölgesinde oluşması, başka bir olumsuz sebep olmuştur. Bu yüzden elektrotun değiştirilmesine karar verilmiştir. Şekil 4'te, E42 2C 21 elektrotu kullanılarak birleştirilen 1. Takımdaki X42 çelik borularından alınmış numunenin gerilme-şekil değiştirme diyagramı, X42 çelik borularının çekme testi değerleri ile karşılaştırılarak verilmiştir. Uyumsuzluk burada daha net şekilde görülmektedir.
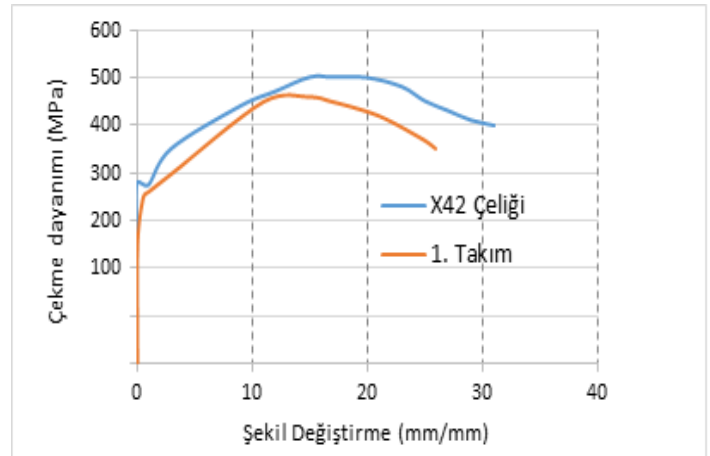


**Şekil 4.** X42 çeliği ve 1. takımın gerilme-şekil değiştirme diyagramı.

Hem kaynak hatalarının giderilmesi hem de kaynak dikişinin mekanik olarak güçlendirilmesi amacıyla, E42 2C 21 elektrotunun kimyasal yapısına, tokluk ve dayanımının artırılması için %0,002 oranında Molibden elementi ve %0,035 oranında Nikel elementi eklenen T1-Saf ismi verilen yeni bir örtülü elektrot, üretici firmaya özel olarak yaptırılmıştır (Tablo 4). Yeni üretilen T1-Saf elektrotun çapı da 2,5 mm olarak belirlenmiştir.

Tablo 6'daki akma ve çekme mukavemeti değerleri incelendiğinde, X42 çeliğinin akma Mukavemeti 372,7 MPa, çekme mukavemeti ise 499,2 MPa olduğu görülmüştür. Bu değerler T1-Saf elektrotu ile kaynak yapılarak birleştirilen 3.takımın 329,96 MPa olan akma mukavemeti ve 467,1 MPa olan çekme mukavemeti ile kıyaslandığında, T1-Saf elektrotunun da birleştirmeye yeterli katkıyı sağlayamadığını göstermektedir.

**Tablo 6.** X42 çeliğin ve 3.takımın akma ve çekme mukavemeti değerleri.

| Numune | Akma (MPa) | Çekme (MPa) | Hasar Bölgesi |
|---|---|---|---|
| X42 çeliği | 372,70 | 499,2 | - |
| 3.Takım | 329,96 | 467,1 | Kaynak |

T1-Saf elektrotunun uygun olmadığı saptandıktan sonra tokluk ve dayanımının daha da artırılması için E42 2C 21 elektrotunun kimyasal yapısına Tablo 4'te belirtildiği gibi %0,008 oranında Molibden ve %0,048 oranında Nikel elementi eklenerek T2-Saf isminde (2,5 mm çapında) yeni bir örtülü elektrot üretici firmaya özel olarak yaptırılmıştır.

T2-Saf elektrotu kullanılarak yapılan birleştirme kaynağının 7, 9, 11, 13, 15 ve 17. takımdaki çekme deneyi sonuçları Tablo 7 de ve grafik olarak ise Şekil 5'te verilmiştir. Tablo 7 ve Şekil 5'ten de anlaşıldığı gibi en uygun elektrotun T2-Saf olduğu anlaşılmıştır. Ayrıca tüm çekme deneyi kopmaları da X42 çelik boru (Ana metal) tarafında olmuştur. Bu da olması istenilen en iyi durumdur [25].

Şekil 5'te görüldüğü gibi, 9. takımın gerilme-şekil değiştirme grafiği incelendiğinde, ortalama akma mukavemetinin en yüksek değer olan 399,2 MPa'a ulaştığı, çekme mukavemetinin 495,76 MPa olduğu ve şekil değiştirme değerinin ise 33 (mm/mm) olduğu görülmektedir. X42 çeliğinin 372,70 MPa olan akma ve 499 MPa olan çekme mukavemeti ile karşılaştırıldığında T2-Saf elektrotunun oldukça başarılı bir kaynak elektrotu olduğu görülmektedir. Elde edilen değerlerden sonra 584 adet X42 çeliğinden üretilmiş doğal gaz boruları T2-Saf elektrotu ile birbirine yeniden kaynak edilmiştir.
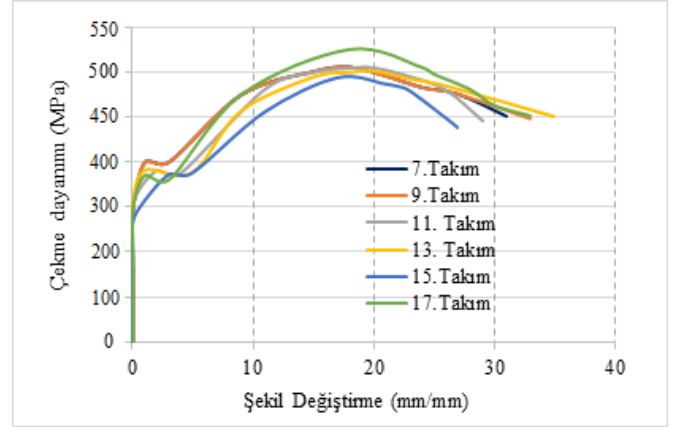


**Şekil 5.** 7, 9, 11, 13, 15 ve 17. takımın gerilme-şekil değiştirme diyagramı.

Şekil 6'da, çekme deneyi öncesi X42 boru çeliği çekme testi numunesi, çekme deneyi sonrası kaynak bölgesi ve ana metalde meydana gelen kırılmaların fotoğrafları verilmiştir.
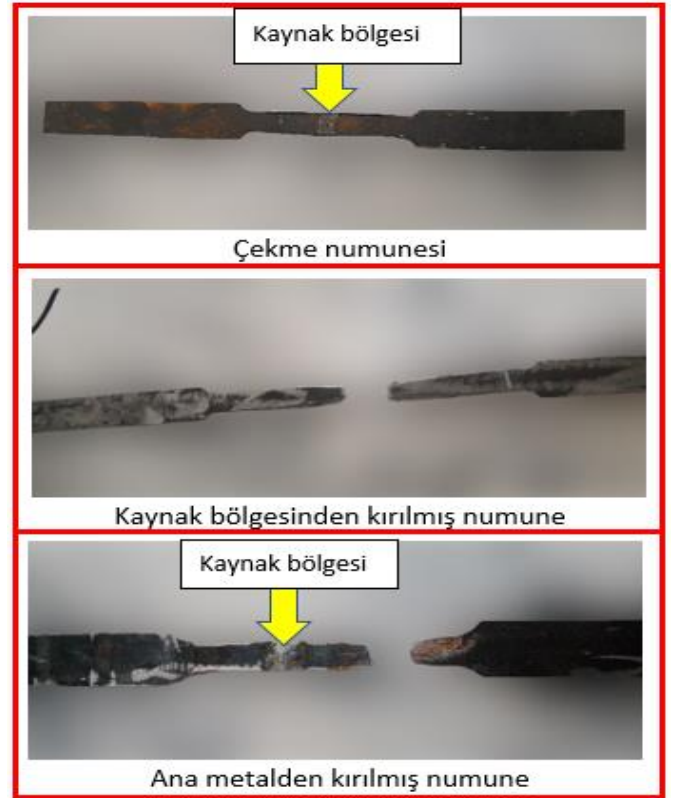


**Şekil 6.** Çekme deneyi öncesi ve sonrası numune fotoğrafları.

**Tablo 7.** Çekme deneyinde kullanılan 7, 9, 11, 13, 15 ve 17. takımların akma ve çekme mukavemeti değerleri.

| Deney Takımı | Numune | Akma Gerilmesi (MPa) | Çekme Gerilmesi (MPa) | Hasar Bölgesi |
|---|---|---|---|---|
| | 1 | 379,60 | 497,70 | Ana Metal |
| | 2 | 382,50 | 501,30 | Ana Metal |
| 7.Takım | 3 | 376,20 | 505,10 | Ana Metal |
| | Ortalama | 379,43 | 501,36 | Ana metal |
| | 1 | 402,70 | 493,00 | Ana Metal |
| | 2 | 395,34 | 499,10 | Ana Metal |
| 9. Takım | 3 | 399,67 | 495,20 | Ana Metal |
| | Ortalama | 399,20 | 495,76 | Ana Metal |
| | 1 | 377,10 | 490,90 | Ana Metal |
| | 2 | 382,80 | 496,30 | Ana Metal |
| 11. Takım | 3 | 389,50 | 492,50 | Ana Metal |
| | Ortalama | 383.13 | 493,23 | Ana Metal |
| | 1 | 370,8 | 509,66 | Ana Metal |
| | 2 | 383,00 | 496,00 | Ana Metal |
| 13. Takım | 3 | 376,00 | 499,33 | Ana Metal |
| | Ortalama | 376,6 | 501,66 | Ana Metal |
| | 1 | 377,00 | 489,10 | Ana Metal |
| | 2 | 369,90 | 472,60 | Ana Metal |
| 15. Takım | 3 | 370,60 | 473,90 | Ana Metal |
| | Ortalama | 372,50 | 478,53 | Ana Metal |
| | 1 | 379,30 | 527,51 | Ana Metal |
| | 2 | 380,90 | 520,99 | Ana Metal |
| 17. Takım | 3 | 375,60 | 519,78 | Ana Metal |
| | Ortalama | 378,60 | 522,76 | Ana Metal |

## IV. SONUÇ VE ÖNERİLER [CONCLUSION AND RECOMMENDATIONS ]

Bu çalışmada, Mardin İli sınırları içerisinde yer alan yaklaşık 7 km uzunluğunda, API 5L X42 kalitesinde, 8 inç ve 4,8 mm et kalınlığındaki doğalgaz borularının kaynak yerleri tahribatsız (Radyografik) muayene yöntemi ile incelenmiştir. Radyografik incelemelerde, kaynak dikişlerinin API 1104 standartlarına uygun olmadığı gözlemlenmiştir. Hatalı kaynak yerleri temizlenen (veya yeniden kaynak ağzı açılan) doğalgaz borularına 17 takım halinde ve 3 farklı elektrotla (Sırasıyla, E42 2C 21, T1-Saf ve T2-Saf) tekrar kaynak yapılmıştır. Daha sonra, tamiri yapılan bu takımların kaynak bölgelerinin yeniden radyografik filmleri çekilmiştir. Böylece, kaynak hataları tespit edilerek sorunlar giderilmiştir. Hataları giderilen X42 çeliğinden yapılmış boruların kaynaklı birleştirme yerlerinden, kaynaklı birleştirmeyi yapmaya en uygun elektrotun tespiti amacıyla numuneler alınarak mukavemetlerini ölçmek için çekme testleri uygulanmıştır. Çekme testleri sonucunda, en yüksek çekme mukavemetini sağlayan T2-Saf elektrotunun en uygun elektrot olduğu tespit edilerek, X42 çeliğinden yapılmış doğalgaz borularının birleştirilmeleri için kullanılması sağlanmıştır. Çalışmamız kapsamında yapılan tahribatlı ve tahribatsız deneylerden elde edilen sonuçlar aşağıda verilmiştir.

• Radyografik incelemeler sonucunda, kaynak yapılan yerlerde cüruf, gözenek ve yeterli birleşmeme gibi birçok hatanın olduğu tespit edilmiştir. İşaretlenen hatalı kaynaklar mekanik olarak taşlama yapılarak temizlenmeye çalışılmıştır. Temizle işleminin yapılamadığı durumlarda ise kaynak bölgesi kesilerek boruların üzerinde yeniden kaynak ağzı açılmış ve tekrar kaynak yapılmıştır.

• Yeni kaynak için sırasıyla, E42 2C 21, T1-Saf ve T2-Saf elektrotları kullanılmıştır.

• Yeni kaynak için denenen elektrotlardan T1-Saf ve T2-Saf elektrotları, E42 2C 21 elektrotunun kimyasal bileşimine farklı oranlarda Molibden ve Nikel elementleri eklenerek ihtiyaçlar doğrultusunda özel olarak üretilerek isimlendirilmişlerdir. Yeni Elektrotların çapı standartlara uygun olarak 2,5 mm olarak üretilmiştir.

• API 5L X42 kalitesinde üretilen doğalgaz borularının kaynakla birleştirilmesi için kullanılan E42 2C 21 ve T1-Saf elektrotlarının, çekme deneyi sonuçlarına göre kopmaların kaynak bölgesinde olmaları sebebiyle uygun olmadıkları tespit edilmiştir. Ayrıca, E42 2C 21 ve T1-Saf elektrotlarının uygun olmamasının bir diğer sebebi de X42

çeliğine göre akma ve çekme mukavemetleri değerlerinin daha düşük çıkmasıdır.

• E42 2C 21 ve T1-Saf elektrotlarının uygun olmamaları sebebiyle T2-Saf elektrodu denenmiştir. T2-Saf elektrodu ile yapılan kaynaklı numunelerin akma ve çekme mukavemetlerinin X42 çeliğinin mukavemet değerlerine yakın hatta bazı takımlarda daha yüksek çıktığı belirlenmiştir. Böylece T2-Saf elektrodu ile doğalgaz boruları kaynak yapılmıştır.

Bu çalışma sayesinde, API 5L X42 kalitesinde üretilen doğalgaz borularının kaynak edilmesinde kullanılacak en uygun elektrot (T2-Saf) belirlenerek ilerde oluşabilecek hasarların önüne geçilmiştir.

### ÇIKAR ÇATIŞMASI [CONFLICTS OF INTEREST]
Yazarlar arasında ve ilgili kurumları arasında herhangi çıkar çatışması olmadığını bildirmişlerdir.

### ETİK KURALLARA UYGUNLUK [RESEARCH AND PUBLICATION ETHICS]
Yazarlar bu makalenin etik kurul onayı veya herhangi bir özel izin gerektirmediğini beyan ederler.

## KAYNAKLAR [REFERENCES]

[1] R. Ashari, A. Eslami, M. Shamanian, and S. Asghari, "Effect of weld heat input on corrosion of dissimilar welded pipeline steels under simulated coating disbondment protected by cathodic protection," *J Mater Res Technol*, vol. 9, no. 2, pp. 2136-2145, Mar-Apr 2020, doi: 10.1016/j.jmrt.2019.12.044.

[2] R. Ashari and A. Eslami, "Anisotropy in Mechanical Properties and Corrosion of X-52 Pipeline Steel at Different Pipe Angles," *Protection of Metals and Physical Chemistry of Surfaces*, vol. 55, no. 3, pp. 546-553, 2019.

[3] J.-h. Baek, Y.-p. Kim, C.-m. Kim, W.-s. Kim, and C.-s. Seok, "Effects of pre-strain on the mechanical properties of API 5L X65 pipe," *Materials Science and Engineering: A*, vol. 527, no. 6, pp. 1473-1479, 2010.

[4] S. S. Abedi, A. Abdolmaleki, and N. Adibi, "Failure analysis of SCC and SRB induced cracking of a transmission oil products pipeline," *Engineering Failure Analysis*, vol. 14, no. 1, pp. 250-261, 2007.

[5] S. Aksöz, H. Ada, and A. Özer, "Toz Altı Kaynak Yöntemiyle Üretilen API 5L X70 Kalite Çelik Boruların Mikroyapı Ve Mekanik Özellikleri," *Gazi Üniversitesi Fen Bilimleri Dergisi Part C: Tasarım ve Teknoloji*, vol. 5, no. 1, pp. 55-64, 2017.

[6] A. Hakan, S. Aksöz, T. Fındık, C. Çetinkaya, and M. Gülsün, "Tozaltı Kaynak Yöntemiyle Birleştirilen Petrol ve Doğalgaz Borularının Mikroyapı ve Mekanik Özelliklerinin İncelenmesi," *Politeknik Dergisi*, vol. 19, no. 3, pp. 275-282, 2016.

[7] Y. Bai, *Pipelines and risers*. Oxford, UK: Elsevier, 2001.

[8] J.-h. Baek, Y.-p. Kim, W.-s. Kim, J.-m. Koo, and C.-s. Seok, "Load bearing capacity of API X65 pipe with dent defect under internal pressure and in-plane bending," *Materials Science and Engineering: A*, vol. 540, pp. 70-82, 2012.

[9] S. Hashemi and D. Mohammadyani, "Characterisation of weldment hardness, impact energy and microstructure in API X65 steel," *International Journal of Pressure Vessels and Piping*, vol. 98, pp. 8-15, 2012.

[10] S. W. Hong, J. M. Koo, C. S. Seok, J. W. Kim, J. H. Kim, and S. K. Hong, "Fatigue life prediction for an API 5L X42 natural gas pipeline," *Engineering Failure Analysis*, vol. 56, pp. 396-402, 2015.

[11] M. Rakhshkhorshid and S. Hashemi, "Experimental study of hot deformation behavior in API X65 steel," *Materials Science and Engineering: A*, vol. 573, pp. 37-44, 2013.

[12] M. Yıldız, "Doğalgaz boru hatlarının kaynağı ve tahribatsız muayenesi," Yüksek Lisans Tezi, İstanbul Teknik Üniversitesi, 2000.

[13] H. Güloğlu, "Tozaltı kaynaklı spiral boru imalinde kaynak parametrelerinin boru kalitesine etkisi," Yüksek Lisans Tezi, İstanbul Teknik Üniversitesi, 1997.

[14] H. Özaltun, "Boru hatlarında hasar oluşumu ve hasarların çeşitli kaynak teknikleri kullanılarak tamir edilme usulleri," Yüksek Lisans Tezi, İstanbul Teknik Üniversitesi, 1999.

[15] API, *API specifications 5L: Specifications for line pipe*. American Petroleum Institute (API) 2015.

[16] K. Tülbentçi, *MİG-MAG Eriyen Elektrod ile Gazaltı Kaynağı*. Gedik Eğitim Vakfı, 1990.

[17] P. Kirkwood, K. Prosser, and P. Boothby, "The Properties of Pipeline Girth Welds Produced by Arc Welding Processes," *Pergamon Press Canada*, pp. 359-377, 1984.

[18] H. Ada, C. Çetinkaya, and A. Durgutlu, "Taguchi metoduyla belirlenen kaynak parametrelerinin API 5L X65 boru birleştirmelerinde radyografik ve makrografik incelemeleri," *Politeknik Dergisi*, vol. 22, no. 2, pp. 375-384, 2019.

[19] C. J. Hellier, *Handbook of nondestructive evaluation*. McGraw-Hill Education, 2013.

[20] G. Knauf and A. Kulgemeyer, "Major Standards for Line Pipe Manufacturing and Testing," *Oil and Gas Pipelines*, pp. 223-224, 2015.

[21] N. Idris, Z. Mustaffa, and A. Fauzi, "Experimental study on radial interacting corrosion for X42 pipelines," *IOP Conference Series: Earth and Environmental Science*, 2020, vol. 476, no. 1: IOP Publishing, p. 012068.

[22] M. A. Azam, S. Sukarti, and M. Zaimi, "Corrosion behavior of API-5L-X42 petroleum/natural gas pipeline steel in South China Sea and Strait of Melaka seawaters," *Engineering Failure Analysis*, vol. 115, p. 104654, 2020.

[23] ASME, *Boiler and Pressure Vessel Code Section V: Nondestructive Examination*. The American Society of Mechanical Engineers 2017.

[24] API, *Welding of Pipelines and Related Facilities: Pipeline Segment*, *API Standard 1104*. American Petroleum Institute (API), 1995.

[25] S. Aksöz, H. Ada, T. Fındık, C. Çetinkaya, B. Bostan, and İ. Candan, "API 5L X65 Çeliklerinin Elektrik Ark Kaynak Yöntemi ile Birleştirilmesinde Kaynak İşleminin Mikroyapı ve Mekanik Özelliklere Etkisinin İncelenmesi," *El-Cezeri Journal of Science and Engineering*, vol. 4, no. 1, pp. 72-81, 2017.

RESEARCH ARTICLE

# Determination of Fuel Consumption for Poultry Farms in Balıkesir by Heating and Cooling Degree Days

*Asiye ASLAN

*Bandırma Onyedi Eylül University, Gönen Vocational School, Gönen-Balıkesir,Turkey,
aaslan@bandirma.edu.tr, ORCID: 0000-0002-1173-5008

## HIGHLIGHTS

- *Heating and cooling degree days were investigated for poultry farms*
- *Degree-day method was used*
- *Heating and cooling costs were calculated per unit area*
- *Highest fuel cost was obtained in the Dursunbey*

## Keywords:

- Degree Days
- Fuel Consumption
- Poultry Farm
- Balıkesir

## GRAPHICAL ABSTRACT

In this study, heating and cooling degree days were investigated for poultry farms using the degree-day method for regions where there are large numbers of poultry farms in the Balıkesir province (City Center, Bandırma, Edremit, Dursunbey, Susurluk, Burhaniye, Ayvalık, Bigadiç, Manyas, Erdek, Gönen). In Figure A, HDD and CDD values are given. The highest HDD value was obtained in Dursunbey as 3725, while the lowest HDD value was obtained in Edremit as 2554.
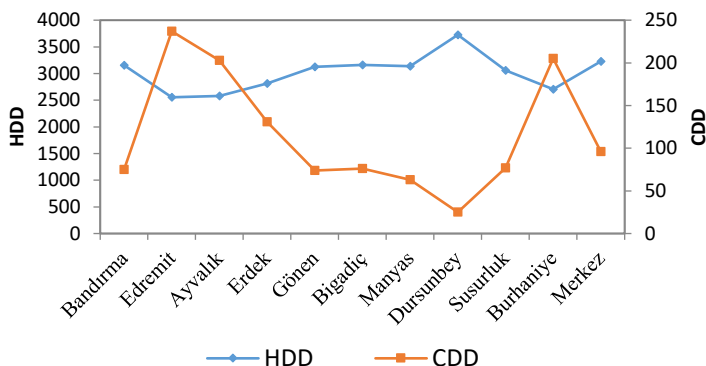
**Figure A.** *HDD and CDD degree days*

**Aim of Article:** *Poultry farming is an important activity in Balıkesir. In this study, heating and cooling degree days (HDD and CDD) were investigated for poultry farms using the degree-days method. Heating and cooling costs were calculated per unit area, according to the use of natural gas, coal, LPG, fuel oil in heating and electrical energy in cooling.*

**Theory and Methodology:** *Heating and cooling degree days were investigated using degree-days method for poultry farms.*

**Findings and Results:** *HDD and CDD varied between 3725 and 2554 and between 237 and 25, respectively.*

**Conclusion:** *HDD and CDD values are important indicators for estimating energy consumption.*

RESEARCH ARTICLE

# Determination of Fuel Consumption for Poultry Farms in Balıkesir by Heating and Cooling Degree Days

*iD Asiye ASLAN

*Bandırma Onyedi Eylül University, Gönen Vocational School, Gönen-Balıkesir,Turkey,
aaslan@bandirma.edu.tr, ORCID: 0000-0002-1173-5008

## HIGHLIGHTS

- *Heating and cooling degree days were investigated for poultry farms*
- *Degree-day method was used*
- *Heating and cooling costs were calculated per unit area*
- *Highest fuel cost was obtained in the Dursunbey*

## Article Info

## ABSTRACT

*Poultry farming is an important activity in Balıkesir. Approximately 12% of broilers produced in Turkey are produced in the province. There are about a hundred facilities within the provincial borders including the center and districts. In this study, heating and cooling degree days (HDD and CDD) were investigated for poultry farms using the degree-days method. Determination of HDD and CDD is important in terms of calculating the amount of energy needed during heating or cooling. Meteorological data for 2005-2018 obtained from the Turkish State Meteorological Service were used. The equilibrium temperature, on which the calculations were based, was the temperature required by broilers during the 6-week production season ($T_{base}$= 31, 29, 25, 23.50, 22.50 and 20.50°C). Heating and cooling costs were calculated per unit area, according to the use of natural gas, coal, LPG, fuel oil in heating and electrical energy in cooling. The results showed that the HDD and CDD values varied between 3725 and 2554 and between 237 and 25, respectively. The lowest fuel costs were obtained in the Edremit district when natural gas was used, while the highest fuel costs were obtained in the Dursunbey district when LPG was used. This study is expected to contribute to the literature and guide investments to be made in this region within this field.*

**Keywords:** *Degree days, fuel consumption, Poultry farm, Balıkesir*

## I. INTRODUCTION

Due to population and economic growth, the demand for energy is increasing rapidly, especially in developing market economies. As welfare increases, increased demand creates new challenges. Additionally, higher fossil fuel consumption leads to higher emissions of greenhouse gasses, especially carbon dioxide ($CO_2$), which causes global warming. These reasons necessitate the efficient use of energy.

Although there are many methods and techniques for energy analysis in buildings, the degree-day method, a simpler technique, is known as the most preferred method. Determination of heating and cooling degree-day numbers is important in terms of calculating the amount of energy needed during the heating and cooling of a building. In the degree-day method, the indoor temperature is directly proportional to the difference between the equilibrium temperature and the outdoor temperature [1-2].

In the field of animal husbandry, environmental conditions, especially temperature, mainly affect both the health and productivity of the animals [3]. While planning a well-organized facility, it should be noted that the facility must be protected from the cold in winter and the heat in summer, as well as from sudden changes of temperature and moisture condensation. Moreover, the optimum temperature must be kept indoor. Providing the optimum conditions for protecting poultry from the effects of unfavorable climatic conditions and increasing productivity depends on the accurate planning and design of houses. Providing the desired environmental conditions in poultry houses throughout the year effectively is also important in terms of economic aspects [4].

There are many studies in the literature to determine heating and cooling degree-day numbers. Dombaycı et al. made an energy consumption estimation by using different base temperatures in cooling months for ten cities in Turkey. As a result of their calculations, they concluded that the highest and the lowest degree-days for cooling were in Şanlıurfa and Ardahan, respectively. The energy consumption for the cooling of Şanlıurfa was 16 times greater than that of Ardahan [5]. Baytorun et al. investigated the statistical correlations between data on heating degree-day and heat energy requirements for provinces where greenhouses are widely used in Turkey. The results they obtained indicated that HDD values facilitate determination of heat energy requirements [6]. Pusat et al. determined degree-hour and degree-day data for the province of Karabük in Turkey. They obtained the meteorological data they used from the Turkish State Meteorological Service. They performed detailed analyses for the equilibrium temperatures of 5,10 and15 °C [7]. Boyacı determined the heating and cooling degree days in poultry houses for the province of Kırşehir and its districts. The degree days ranged from 2678.47 to 7846.63 for heating and from 0 to 441.76 for cooling. Since heating degree days are high, heating costs are also important for production costs [8]. Boyacı et al. determined the heating and cooling degree days of a laying quail henhouse. They concluded that, depending on the temperature outside, there was a need for heating in the henhouse for 74 days, and the HDD value was about 1175, while there was no need for cooling [9]. Harvey recommended three reference temperatures and corresponding indices for both HDD and CDD in their study. The first

reference temperature they proposed was the indoor thermostat setting. The second was the outdoor temperature at which the heat loss balances the internal heat gain. The third was the outdoor temperature at which the indoor and solar heat gains are balanced with the heat loss. In the results, the author stated that, if the differences between reference temperatures are known, these differences can be used to calculate the internal and solar heat gain for a given building [10]. D'Amico et al. determined the relationship between heating degree-day and heating energy performance with some simple correlations to obtain a preliminary assessment of energy demands. In their results, the authors stated that the proposed methodology could be expanded and used to increase the reliability of any decision support tool based on climate indices [11]. Karaağaç et al. planned a facility that aimed to meet electrical energy needs by placing solar panels on the roof of apoultry farm. The monthly average generation of the system to be installed on the roof was 2,875 kWh, and the total annual electricity generation was 34,510 kWh. The photovoltaic panels they used on the roof were calculated have a 6-year depreciation period, and 32,439.4 kg of $CO_2$ emission was prevented thanks to this solar power plant design [12].

In this study, heating and cooling degree days were investigated for poultry farms using the degree-day method for regions where there are large numbers of poultry farms in the Balıkesir province (Center, Bandırma, Edremit, Dursunbey, Susurluk, Burhaniye, Ayvalık, Bigadiç, Manyas, Erdek, Gönen) in Turkey. The meteorological data of 2005-2018 obtained from the Turkish State Meteorological Service were used in the study. The heating or cooling needs of poultry farms were determined by equilibrium temperatures. Heating and cooling costs were calculated per unit area, according to the use of natural gas, coal, LPG, fuel oil in heating and electrical energy in cooling.

## II. METHOD

### A. Heating and cooling degree-days

Generally, DD is considered one of the simplest methods for energy calculation during heating and cooling buildings [1]. Degree-days are characterized with the sum of temperature differences between the average outdoor air temperature over a given period of time and a known reference temperature. In this study,

the HDD and CDD were determined during poultry production based on equations (1) and (2) [13, 14].

For $T_{out} < T_{base}$,

$$HDD = \sum_{1}^{n}(T_{base} - T_{out}) \qquad (1)$$

For $T_{base} < T_{out}$,

$$CDD = \sum_{1}^{n}(T_{out} - T_{base}) \qquad (2)$$

where n is the days total number during the period. $T_{base}$ and $T_{out}$ are the broilers base temperature and the mean temperature of outside air, respectively.

Broiler production time is recommended to be 41 and 42 days for maximum profit. In this study, production for 42 days and downtime and annual rotation were taken as 7 (Table 1). Optimum internal temperature values, which poultrys in poultry need on a weekly basis, are the equilibrium temperature values recommended by researchers for poultry breeding (Table 2).

**TableI.**
Periods and dates of poultry production [13, 15].

| Annual rotation | Dates | Number of days |
|---|---|---|
| Production 1 | 1 Jan - 11 Feb | 42 |
| Closed | 12 Feb-23 Feb | 12 |
| Production 2 | 24 Feb-6 Apr | 42 |
| Closed | 7 Apr - 18 Apr | 12 |
| Production 3 | 19 Apr -30 May | 42 |
| Closed | 31 May- 11 Jun | 12 |
| Production 4 | 12 Jun-23 Jul | 42 |
| Closed | 24 Jul -4 Aug | 12 |
| Production 5 | 5 Aug - 15 Sep | 42 |
| Closed | 16 Sep -27 Sep | 12 |
| Production 6 | 28 Sep -8 Nov | 42 |
| Closed | 9 Nov- 20 Nov | 12 |
| Production 7 | 21 Nov - 31 Dec | 42 |

**TableII.**
Weekly base temperaturere commended for broilers [13, 15].

| Time | $T_{base}$(°C) |
|---|---|
| Week 1 | 31.00 |
| Week 2 | 29.00 |
| Week 3 | 25.00 |
| Week 4 | 23.50 |
| Week 5 | 22.50 |
| Week 6 | 20.50 |

*B. Calculating the Heat Load*

The heat loss from unit surface:

$$q = U\Delta T \qquad (3)$$

where U is the overall heat transfer coefficient. The annual heat losses from unit area can be approximately calculated depending on the degree-days number as the following:

$$q_A = 86400\ U\ DD \qquad (4)$$

where DD is the degree days. The annual energy requirement for heating ($E_A$) can be obtained approximately by dividing the annual heat loss to the efficiency of the heating system ($\eta_s$):

$$E_A = \frac{86400\ U\ DD}{\eta_s} \qquad (5)$$

The annual heating cost $C_{A,H}$ ($/m$^2$-year) per unit area can be calculated by the equation (6):

$$C_{A,H} = \frac{86400\ U\ HDD\ C_f}{H_u\ \eta_s} \qquad (6)$$

where $C_f$ is fuel cost ($/kg) and $H_u$ is the lower heating value of the fuel (J/kg; J/m$^3$). The annual cooling cost per unit area can be calculated using equation (7). COP is the performance coefficient of the cooling system and it was taken as 2.5 in this study [8]:

$$C_{A,C} = \frac{86400\ U\ CDD\ C_f}{COP} \qquad (7)$$

The data used to calculate the heating and cooling costs are given in Table 3.

**TableIII.**
Properties of fuels and system efficiency [16, 17].

| Fuel | Cost | Lower Heating Value, $H_u$ | System Efficiency ($\eta_s$)(%) |
|---|---|---|---|
| Natural gas | 0.2868 $/m$^3$ | 34.542x106J/m$^3$ | 93 |
| Coal | 0.1921 $/kg | 25.122x106 J/kg | 65 |
| LPG | 1.75 $/kg | 46.442x106 J/kg | 88 |
| Fuel-Oil | 0.73 $/kg | 41.317x106 J/kg | 80 |
| Electricity | 0.1252 $/kWh | (COP) | 2.5 |

## III. RESULTS AND DISCUSSION

In this study, heating and cooling degree days were investigated for poultry farms using the degree-day method for regions where there are large numbers of poultry farms in the Balıkesir province (City Center, Bandırma, Edremit, Dursunbey, Susurluk, Burhaniye, Ayvalık, Bigadiç, Manyas, Erdek, Gönen) of Turkey. Table 4 presents the calculated HDD and CDD values. The presented HDD and CDD values were the annual total values. The calculations were made by accounting for a total of 7 production periods in each year and 6 weeks in each period. In each production period, the equilibrium temperature of the relevant week was taken as a basis ($T_{base}$ = 31, 29, 25, 23.50, 22.50 and 20.50 °C). The periods when the system was turned off were not taken into account. (Tables 1, 2).

The highest HDD value was obtained in Dursunbey as 3725, while the lowest HDD value was obtained in Edremit as 2554.The highest and lowest CDD values were obtained in Edremit as 237 and in Dursunbey as 25, respectively.

Table 5 shows the HDD and CDD values according to the equilibrium temperatures. According to the given annual rotation table, while heating was required at all equilibrium temperatures except those corresponding to summer months, cooling was required at equilibrium temperatures corresponding to summer months.

Table 6 shows the HDD and CDD numbers that were obtained. Figure 1 graphically displays the HDD and CDD values according to the equilibrium temperatures in all districts.

**TableIV.**
Annual HDD and CDD degree days.

|  | HDD | CDD |
|---|---|---|
| Bandırma | 3155 | 75 |
| Edremit | 2554 | 237 |
| Ayvalık | 2581 | 203 |
| Erdek | 2816 | 131 |
| Gönen | 3123 | 74 |
| Bigadiç | 3159 | 76 |
| Manyas | 3137 | 63 |
| Dursunbey | 3725 | 25 |
| Susurluk | 3062 | 77 |
| Burhaniye | 2707 | 205 |
| Merkez | 3227 | 96 |

**TableV.**
HDD and CDD values according to base temperature for all production periods

|  | 31 °C | | 29 °C | | 25 °C | | 23.5 °C | | 22.5 °C | | 20.5 °C | |
|---|---|---|---|---|---|---|---|---|---|---|---|---|
|  | HDD | CDD | HDD | CDD | HDD | HDD | HDD | CDD | HDD | CDD | HDD | CDD |
| Bandırma | 805 | 0 | 715 | 0 | 502 | 1 | 429 | 11 | 402 | 20 | 299 | 43 |
| Edremit | 672 | 0 | 568 | 0 | 404 | 30 | 351 | 50 | 324 | 60 | 233 | 95 |
| Ayvalık | 682 | 0 | 575 | 0 | 405 | 25 | 353 | 42 | 328 | 50 | 235 | 85 |
| Erdek | 736 | 0 | 631 | 0 | 446 | 10 | 385 | 23 | 360 | 34 | 255 | 62 |
| Gönen | 791 | 0 | 700 | 0 | 497 | 1 | 430 | 10 | 402 | 18 | 300 | 44 |
| Bigadiç | 802 | 0 | 701 | 0 | 505 | 0 | 436 | 10 | 408 | 21 | 303 | 44 |
| Manyas | 793 | 0 | 706 | 0 | 502 | 0 | 431 | 6 | 407 | 17 | 295 | 39 |
| Dursunbey | 912 | 0 | 795 | 0 | 613 | 0 | 528 | 0 | 497 | 3 | 378 | 21 |
| Susurluk | 778 | 0 | 690 | 0 | 488 | 0 | 421 | 11 | 393 | 21 | 289 | 44 |
| Burhaniye | 702 | 0 | 596 | 0 | 430 | 24 | 371 | 43 | 348 | 51 | 254 | 86 |
| Merkez | 804 | 0 | 710 | 0 | 516 | 4 | 449 | 17 | 423 | 25 | 323 | 49 |

**TableVI.**
HDD and CDD numbers according to base temperature for all production periods

|  | 31 °C | | 29 °C | | 25 °C | | 23.5 °C | | 22.5 °C | | 20.5 °C | |
|---|---|---|---|---|---|---|---|---|---|---|---|---|
|  | HDD | CDD | HDD | CDD | HDD | CDD | HDD | CDD | HDD | CDD | HDD | CDD |
| Bandırma | 49 | 0 | 49 | 0 | 43 | 7 | 38 | 11 | 37 | 14 | 35 | 14 |
| Edremit | 49 | 0 | 49 | 0 | 35 | 11 | 35 | 14 | 35 | 14 | 29 | 27 |
| Ayvalık | 49 | 0 | 49 | 0 | 35 | 14 | 35 | 14 | 35 | 14 | 28 | 21 |
| Erdek | 49 | 0 | 49 | 0 | 42 | 7 | 35 | 14 | 35 | 14 | 35 | 20 |
| Gönen | 49 | 0 | 49 | 0 | 44 | 5 | 37 | 12 | 37 | 11 | 33 | 16 |
| Bigadiç | 49 | 0 | 49 | 0 | 45 | 0 | 38 | 11 | 38 | 12 | 31 | 18 |
| Manyas | 49 | 0 | 49 | 0 | 49 | 0 | 38 | 11 | 38 | 11 | 31 | 18 |
| Dursunbey | 49 | 0 | 49 | 0 | 49 | 0 | 49 | 0 | 45 | 4 | 42 | 7 |
| Susurluk | 49 | 0 | 49 | 0 | 46 | 3 | 37 | 12 | 35 | 12 | 30 | 18 |
| Burhaniye | 49 | 0 | 49 | 0 | 35 | 14 | 35 | 14 | 35 | 14 | 28 | 21 |
| Merkez | 49 | 0 | 49 | 0 | 42 | 7 | 35 | 14 | 35 | 14 | 35 | 14 |
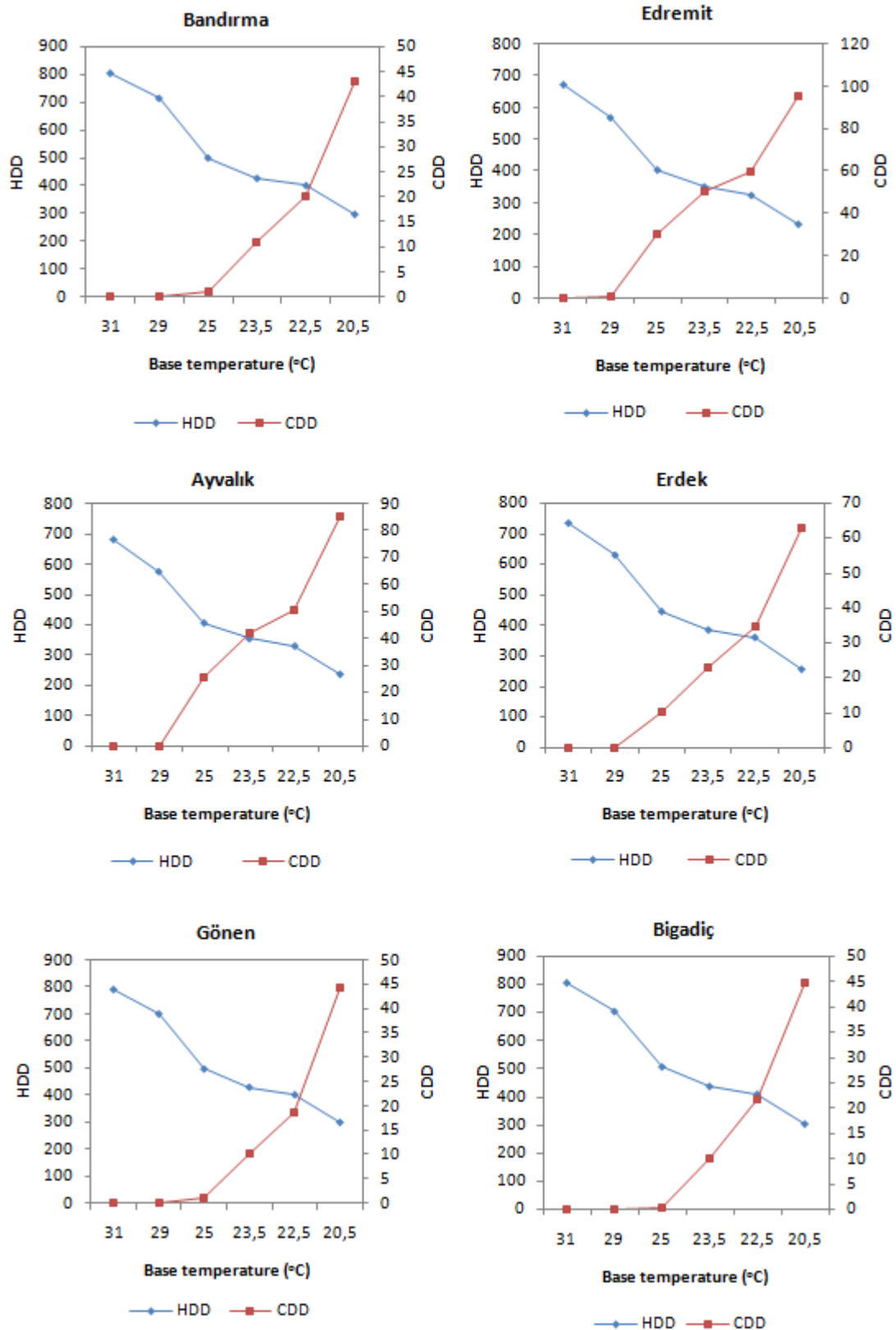
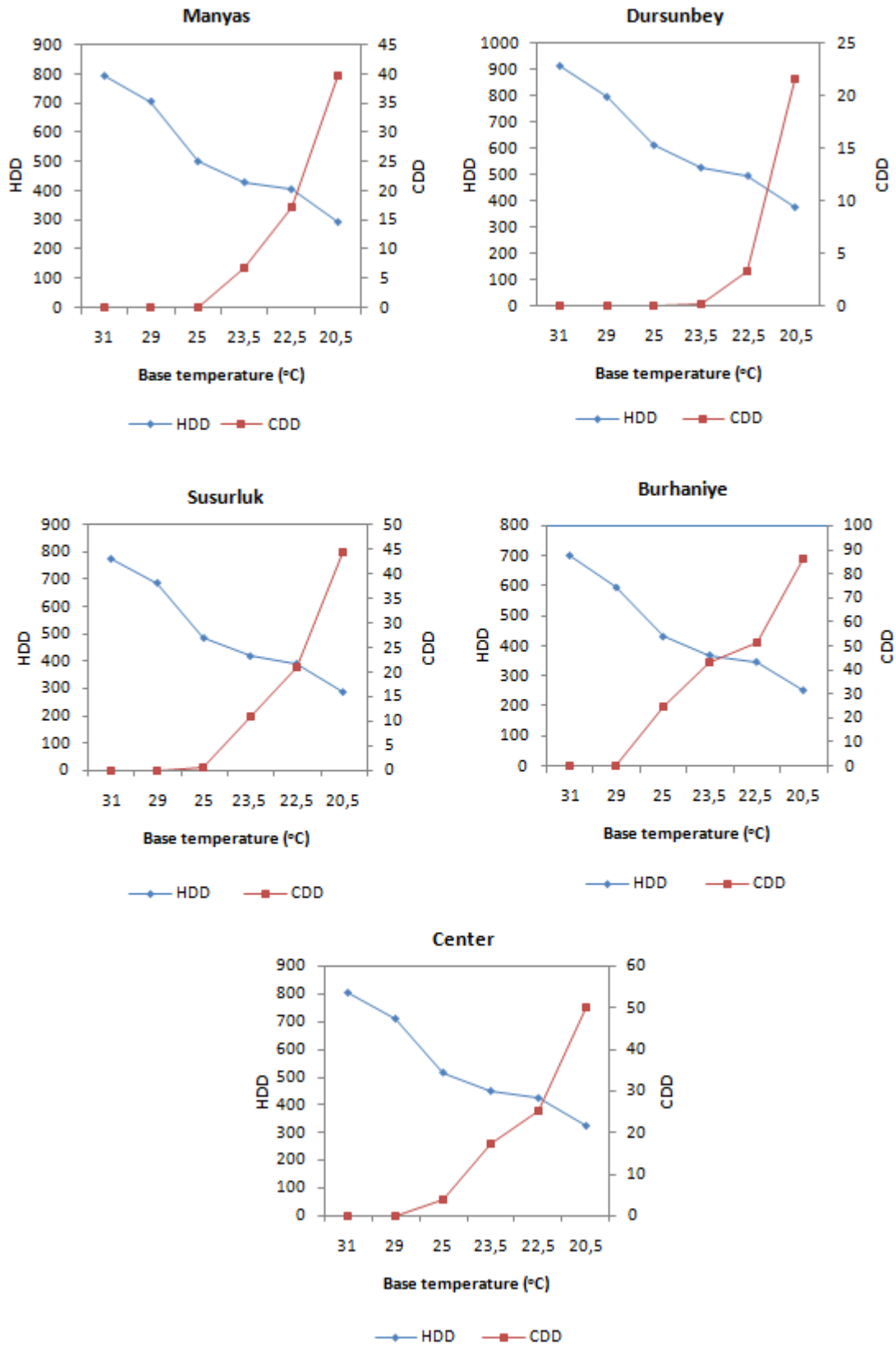**Figure 1.** HDD and CDD according to base temperature.

**Figure 1**. (continued)

Tables 7 and 8 show the costs of energy required per unit area by the equilibrium temperatures and the annual total value. Calculations were made for natural gas, coal, LPG and fuel oil in heating and for electrical energy in cooling. In the comparison on the basis of fuels, it was found that the most economical fuel was natural gas, while the highest cost was seen in LPG. In terms of heating, the highest and lowest energy costs were obtained in Dursunbey and in Edremit, respectively. The high energy costs in

heating revealed the importance of facility planning.

In terms of cooling, the energy cost in the region was generally low. This cost was obtained relatively higher in the gulf districts of Edremit, Burhaniye and Ayvalık. It was observed that the production periods that coincided only with the summer season in other regions also required energy for the high equilibrium temperatures.

**TableVII.**

Heating costs per unit area ($/m$^2$)

| | 31 $^{O}$C | 29 $^{O}$C | 25 $^{O}$C | 23.5 $^{O}$C | 22.5 $^{O}$C | 20.5 $^{O}$C | Annual |
|---|---|---|---|---|---|---|---|
| Natural gas | | | | | | | |
| Bandırma | 0.62 | 0.55 | 0.38 | 0.33 | 0.31 | 0.23 | 2.43 |
| Edremit | 0.51 | 0.43 | 0.31 | 0.27 | 0.25 | 0.18 | 1.97 |
| Ayvalık | 0.52 | 0.44 | 0.31 | 0.27 | 0.25 | 0.18 | 1.99 |
| Erdek | 0.56 | 0.48 | 0.34 | 0.29 | 0.27 | 0.19 | 2.17 |
| Gönen | 0.61 | 0.54 | 0.38 | 0.33 | 0.31 | 0.23 | 2.40 |
| Bigadiç | 0.61 | 0.54 | 0.39 | 0.33 | 0.31 | 0.23 | 2.43 |
| Manyas | 0.61 | 0.64 | 0.38 | 0.33 | 0.31 | 0.22 | 2.42 |
| Dursunbey | 0.70 | 0.61 | 0.47 | 0.40 | 0.38 | 0.29 | 2.87 |
| Susurluk | 0.60 | 0.53 | 0.37 | 0.32 | 0.30 | 0.22 | 2.36 |
| Burhaniye | 0.54 | 0.46 | 0.33 | 0.28 | 0.26 | 0.19 | 2.08 |
| Merkez | 0.62 | 0.54 | 0.39 | 0.34 | 0.32 | 0.24 | 2.48 |
| Coal | | | | | | | |
| Bandırma | 0.81 | 0.72 | 0.51 | 0.43 | 0.40 | 0.30 | 3.20 |
| Edremit | 0.68 | 0.57 | 0.41 | 0.35 | 0.33 | 0.23 | 2.59 |
| Ayvalık | 0.69 | 0.58 | 0.41 | 0.35 | 0.33 | 0.23 | 2.62 |
| Erdek | 0.74 | 0.64 | 0.45 | 0.39 | 0.36 | 0.26 | 2.86 |
| Gönen | 0.80 | 0.71 | 0.50 | 0.43 | 0.40 | 0.30 | 3.17 |
| Bigadiç | 0.81 | 0.71 | 0.51 | 0.44 | 0.41 | 0.30 | 3.21 |
| Manyas | 0.80 | 0.71 | 0.51 | 0.43 | 0.41 | 0.30 | 3.18 |
| Dursunbey | 0.92 | 0.80 | 0.62 | 0.53 | 0.50 | 0.38 | 3.78 |
| Susurluk | 0.79 | 0.70 | 0.49 | 0.42 | 0.40 | 0.29 | 3.11 |
| Burhaniye | 0.71 | 0.60 | 0.43 | 0.37 | 0.35 | 0.25 | 2.74 |
| Merkez | 0.81 | 0.72 | 0.52 | 0.45 | 0.43 | 0.32 | 3.28 |
| LPG | | | | | | | |
| Bandırma | 2.98 | 2.64 | 1.85 | 1.58 | 1.49 | 1.10 | 11.68 |
| Edremit | 2.48 | 2.10 | 1.49 | 1.30 | 1.20 | 0.86 | 9.45 |
| Ayvalık | 2.52 | 2.13 | 1.50 | 1.30 | 1.21 | 0.87 | 9.55 |
| Erdek | 2.72 | 2.33 | 1.65 | 1.42 | 1.33 | 0.94 | 10.42 |
| Gönen | 2.92 | 2.59 | 1.84 | 1.59 | 1.49 | 1.11 | 11.56 |
| Bigadiç | 2.97 | 2.59 | 1.87 | 1.61 | 1.51 | 1.12 | 11.69 |
| Manyas | 2.93 | 2.61 | 1.85 | 1.59 | 1.50 | 1.09 | 11.61 |
| Dursunbey | 3.37 | 2.94 | 2.26 | 1.95 | 1.84 | 1.40 | 13.79 |
| Susurluk | 2.88 | 2.55 | 1.80 | 1.56 | 1.45 | 1.07 | 11.33 |
| Burhaniye | 2.59 | 2.20 | 1.59 | 1.37 | 1.29 | 0.94 | 10.01 |
| Merkez | 2.97 | 2.63 | 1.91 | 1.66 | 1.56 | 1.19 | 11.94 |
| Fuel-oil | | | | | | | |
| Bandırma | 1.89 | 1.68 | 1.17 | 1.00 | 0.94 | 0.70 | 7.40 |
| Edremit | 1.57 | 1.53 | 0.94 | 0.82 | 0.76 | 0.54 | 5.99 |
| Ayvalık | 1.60 | 1.35 | 0.95 | 0.82 | 0.77 | 0.55 | 6.06 |
| Erdek | 1.73 | 1.48 | 1.04 | 0.90 | 0.84 | 0.60 | 6.61 |
| Gönen | 1.85 | 1.64 | 1.16 | 1.01 | 0.94 | 0.70 | 7.33 |
| Bigadiç | 1.84 | 1.64 | 1.18 | 1.02 | 0.96 | 0.71 | 7.41 |
| Manyas | 1.86 | 1.66 | 1.17 | 1.01 | 0.95 | 0.69 | 7.36 |
| Dursunbey | 2.14 | 1.86 | 1.44 | 1.24 | 1.16 | 0.88 | 8.74 |
| Susurluk | 1.82 | 1.52 | 1.14 | 0.99 | 0.92 | 0.68 | 7.19 |
| Burhaniye | 1.64 | 1.40 | 1.01 | 0.87 | 0.91 | 0.59 | 6.35 |
| Merkez | 1.89 | 1.67 | 1.21 | 1.05 | 0.99 | 0.75 | 7.57 |

**TableVIII.**
Cooling costs per unit area ($/m$^2$)

| | 31 $^{\circ}$C | 29 $^{\circ}$C | 25 $^{\circ}$C | 23.5 $^{\circ}$C | 22.5 $^{\circ}$C | 20.5 $^{\circ}$C | Annual |
|---|---|---|---|---|---|---|---|
| | | | | Electricity | | | |
| Bandırma | 0.00 | 0.00 | 0.00 | 0.03 | 0.06 | 0.13 | 0.22 |
| Edremit | 0.00 | 0.00 | 0.09 | 0.15 | 0.18 | 0.29 | 0.72 |
| Ayvalık | 0.00 | 0.00 | 0.07 | 0.12 | 0.15 | 0.25 | 0.61 |
| Erdek | 0.00 | 0.00 | 0.03 | 0.07 | 0.10 | 0.19 | 0.39 |
| Gönen | 0.00 | 0.00 | 0.00 | 0.03 | 0.05 | 0.13 | 0.22 |
| Bigadiç | 0.00 | 0.00 | 0.00 | 0.03 | 0.06 | 0.13 | 0.23 |
| Manyas | 0.00 | 0.00 | 0.00 | 0.02 | 0.05 | 0.12 | 0.19 |
| Dursunbey | 0.00 | 0.00 | 0.00 | 0.00 | 0.01 | 0.06 | 0.07 |
| Susurluk | 0.00 | 0.00 | 0.00 | 0.03 | 0.06 | 0.13 | 0.23 |
| Burhaniye | 0.00 | 0.00 | 0.07 | 0.13 | 0.15 | 0.26 | 0.62 |
| Merkez | 0.00 | 0.00 | 0.01 | 0.05 | 0.07 | 0.15 | 0.29 |

Calculation of HDD and CDD values provides important information in the planning phase of facilities. This calculation will allow selection of the appropriate system and material to meet the energy need and design of the structure. Besides, accurately estimating the energy need will allow broilers to be bred under suitable conditions and thus increase productivity.

Besides, HDD and CDD values are also important indicators for estimating energy consumption. This is because it is known that energy consumption increases as the number of heating and cooling degree days increases and decreases as the number of days decreases.

It was observed that the HDD values were higher than the CDD values throughout the region. The low energy costs for cooling were an important advantage. To make heating energy consumption more economical, on the other hand, utilization of renewable energy resources may be considered. The existence of geothermal resources in the Edremit, Gönen and Bigadiç districts may provide an opportunity to utilize geothermal energy in these regions.

Furthermore, thermal insulation is a critical factor in reducing energy costs. Insulation of the external walls and roofs of facilities with proper insulation materials will reduce the energy need and provide energy savings. Insulation will contribute to both making savings and environmental factors.

## IV.  CONCLUSION

In this study, HDD and CDD values for raising broiler were calculated, using the meteorological data obtained from the General Directorate of Meteorology for the city center and districts of the province of Balıkesir in Turkey. The daily average outdoor temperature data between 2005 and 2018 were used. Calculations were made based on the required equilibrium temperatures for the annual rotation and 6-week broiler breeding periods. Given the HDD and CDD values, it was considered that four different fuels (natural gas, coal, LPG and fuel oil) would be used for heating, and electrical energy would be used for cooling. The results showed that the heating costs were higher than the cooling costs. It was concluded that insulation would be a significant factor in reducing energy costs for the current facilities and new facilities planned to be established in the region. Insulation is highly important for reducing emissions, as well.

## CONFLICTS OF INTEREST

They reported that there was no conflict of interest between the authors and their respective institutions.

## RESEARCH AND PUBLICATION ETHICS

In the studies carried out within the scope of this article, the rules of research and publication ethics were followed.

## REFERENCES

[1]  Büyükalaca, O., Bulut, H., Yılmaz, T., (2001) Analysis of variable-base heating and cooling degree-days for Turkey, Applied Energy 69/4, 269-283.
[2]  Büyükalaca, O., Bulut, H., Yılmaz, T., (2000) Türkiye'nin bazı illeri için derece-gün değerleri, 12. Ulusal Isı Bilimi ve Tekniği Kongresi Bildiriler Kitabı, Cilt 1, sayfa 107-112, Sakarya.

[3] Arıtürk, E., Ergün, A., Yalçın, S., (1986) The Relationship Between Poultry and Environmental Temperature, Lalahan Zoot. Arast. Enst. Derg. 26 (1-4) 42-52.

[4] Özdemir, E., Poyraz, Ö., (1997) Insulation of Poultry Houses, Lalahan Hay. Arast. Enst. Derg. 37 (2) 91-108.

[5] Dombaycı, A., Bayrakçı , HC., Özgür, A. E., (2009) Estimation of Cooling Energy Consumption in Residents for Different Base Temperatures By Degree Day Method, Süleyman Demirel Üniversitesi, Fen Bilimleri Enstitüsü Dergisi, 13-3,311-314.

[6] Baytorun, A.N., Üstün, S., Akyüz, A., (2016) Determination of Heat Energy Requirements for Greenhouses in Regions with Different Heating-Degree-Day (HDD) Values, Çukurova Üniversitesi Mühendislik Mimarlık Fakültesi Dergisi, 31(2), 119-128.

[7] Pusat, Ş., Tunç, N., Ekmekçi İ., Yetişken, Y., (2015) Degree-Time Calculations For Karabük, ISITES2015 Valencia –Spain

[8] Boyacı, S., (2018) Determination of Heating and Cooling Degree Values in Poultry House Using Degree Day Method: The Case of Kırşehir, Nevşehir Bilim ve Teknoloji Dergisi (2018), 7(1) 75-82.

[9] Boyacı, S., Filik, G., Filik A.G., (2018) Determination of the heating and cooling degree day values of laying quail henhouse by the degree day method, Süleyman Demirel Üniversitesi Ziraat Fakültesi Dergisi, ISSN 1304-9984.

[10] Harvey, L.D, (2020) Using modified multiple heatinh-degree day (HDD) and cooling-degree day (CDD) indices to estimate building heating and cooling loads, Energy and Buildings, 229,110475.

[11] D'Amico, G., Ciulla, G., Ferrari, S., (2019), Building energy demand assessment through heating degree days: The importance of a climatic dataset, Applied Energy, 242, 1285-1306.

[12] Karaağaç, M.O., Oğul, H., Bardak, S., (2020) Design and cost analysis of solar energy system for poultry farm, Düzce Üniversitesi Bilim ve Teknoloji Dergisi, 8, 711-722.

[13] Küçüktopcu, E., Cemek, B., (2018) A study on environmental impact of insulation thickness of poultry building walls, Energy 150 583-590.

[14] De Rosa, M., Bianco, V., Scarpa F., Tagliafico LA., (2014) Heating and cooling building energy demand evaluation; a simplified model and a modified degree days approach. Appl energy, 128:217-29.

[15] Matzarakis, A., Balafoutis, C., (2004) Heating degree-days over Greece as an index of energyconsumption. Int J Climatol 24(14):1817-28.

[16] http://www.canakkalegaz.com.tr/turkish/2019.

[17] www.dosider.org, Fuel prices, 2020.

RESEARCH ARTICLE

# Production of Self-Cleaning Laminate Surfaces with Antimicrobial Effect

* Ahmet GENÇER, [1] Gül Merve GENÇER, [2] Murat AKARSU, [3] Ertuğrul ARPAÇ

* AGT Wood Industry and Trade Co., R&D Center, 07190, Turkey, ahmet88gencer@gmail.com orcid.0000-0002-4961-966X
[1] BelenMed R&D Ltd., Antalya Technopolis, 07070, Turkey, gulmervekurtbelen@gmail.com orcid.0000-0001-7087-609X
[2] Akdeniz University, Faculty of Science, 07058 Antalya, Turkey, akarsu@akdeniz.edu.tr orcid.0000-0003-2053-2197
[3] Akdeniz University, Faculty of Science, 07058 Antalya, Turkey, earpac@akdeniz.edu.tr orcid.0000-0001-8645-6786

## HIGHLIGHTS

- *Laminate surface coating solution with self-cleaning properties and antimicrobial effect was obtained.*
- *Sn and Fe doped $TiO_2$ nanoparticle sols with an average particle size of 15 nm were synthesized in different solvent system using the sol-gel method.*
- *The functional surface coating solution obtained by the study has the qualities to be used on different surfaces (metal, plastic, glass, etc.) other than laminate, due to its high strength, non-toxic effect and versatility.*
- *With this research, the production method of doped titanium dioxide nanoparticle that can be synthesized on an industrial scale was determined.*

## GRAPHICAL ABSTRACT

Sn and Fe doped $TiO_2$ nanoparticle sols having a mean particle size of $15\pm2$ nm have been successfully synthesized via a sol-gel method and their absorption behavior were determined. Effects of different types of acids and acid/precursor mol ratio on particle size were investigated. Results indicate that photocatalytic performance decreases as the particle size increases and there is an optimum %wt value of doping. Synthesized sols were also applied as a coating on lignocellulosic industrial materials such as high density (HDF) melamine faced laminate floorings and their self cleaning properties and anti-microbial efficiencies were evaluated. In Figure A self-cleaning properties of doped-$TiO_2$ nanoparticle coated surfaces against different types of pollutants were observed as %80,1 more efficient against Rodamin B dye, %89,9 against Methylene Blue dye.
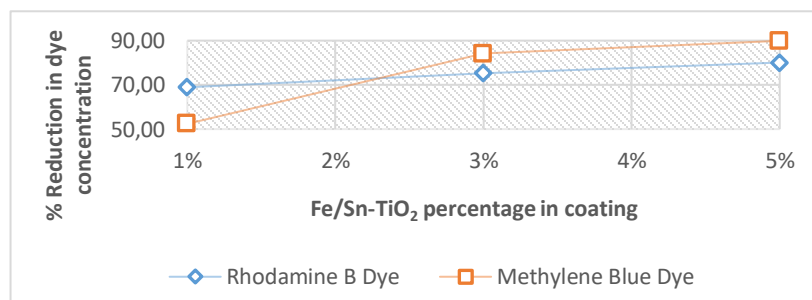
**Figure A.** Solar-Box weathering test against dyes pollutant results of the samples

**Aim of Article:** *Photocatalytic, anti-bacterial efficent and easy-to-clean coating material for laminate flooring products consists of Sn and Fe doped $TiO_2$ synthesized via a sol-gel method.*

**Theory and Methodology:** *Two different synthesis methods; solvent-based and water-based, were used to obtain nanoparticle sols with the same characteristics. $TiO_2$ nanoparticles were doped with a combination of Sn and Fe elements in order to shift the absorption behavior of the non-doped $TiO_2$ from the UV region to the Visible region of the light, so as to obtain much better photocatalytic activity. Synthesized sols were also applied as a coating on lignocellulosic industrial materials such as high density (HDF) melamine faced laminate floorings and their self cleaning properties and anti-microbial efficiencies were evaluated.*

**Findings and Results:** *Self-cleaning properties of doped-$TiO_2$ nanoparticle coated surfaces against different types of pollutants were observed as %80,1 more efficient against Rodamin B dye, %89,9 against Methylene Blue dye, and %50 against oleic acid. It has been observed the coated laminate flooring surfaces perform an antibacterial efficiency with a %97 reduction of bacterial load for E.coli and a %87 reduction for the S.aureus.*

**Conclusion:** *This research focused on an easy and industrial applicable synthesis of doped-titanium dioxide nanoparticles and utilizing of these sols in industrial applications as a coating material on laminate flooring products in order to add functional properties.*

ARAŞTIRMA MAKALESİ | *RESEARCH ARTICLE*

# Kendi Kendini Temizleme Özelliğine Sahip Antimikrobiyal Etki Gösteren Laminat Yüzeylerinin Eldesi

* 🆔Ahmet GENÇER, [1] 🆔Gül Merve GENÇER, [2] 🆔Murat AKARSU, [3] 🆔Ertuğrul ARPAÇ

* AGT Wood Industry and Trade Co., R&D Center, 07190, Turkey, ahmet88gencer@gmail.com orcid.0000-0002-4961-966X
[1] BelenMed R&D Ltd., Antalya Technopolis, 07070, Turkey, gulmervekurtbelen@gmail.com orcid.0000-0001-7087-609X
[2] Akdeniz University, Faculty of Science, 07058 Antalya, Turkey, akarsu@akdeniz.edu.tr orcid.0000-0003-2053-2197
[3] Akdeniz University, Faculty of Science, 07058 Antalya, Turkey, earpac@akdeniz.edu.tr orcid.0000-0001-8645-6786

**Ö N E Ç I K A N L A R**/ H I G H L I G H T S

- *Kendi kendini temizleyebilen özelliğe sahip, antimikrobiyal etki gösteren laminat yüzey kaplama çözeltisinin eldesi sağlanmıştır.*
- *Ortalama 15 nm partikül boyutuna sahip Sn ve Fe katkılı TiO₂ nanopartikül solları, sol-jel yöntemi kullanılarak farklı çözgen ortamlarında sentezlenmiştir.*
- *Çalışma ile elde edilen fonksiyonel yüzey kaplama çözeltisi dayanımının yüksek olması, toksik etki göstermemesi ve çok yönlü olması sebebiyle laminat dışında farklı yüzeylere de (metal, plastik, cam vb.) kullanılabilecek niteliklere sahiptir.*
- *Bu araştırma ile endüstriyel ölçekte sentezlenebilecek düzeyde katkılı titanyum dioksit nanopartikül üretim yöntemi belirlenmiştir.*

**ÖZET** / *ABSTRACT*

*Gelişen teknoloji ile birlikte mevcut malzemelerde sürekli olarak iyileştirme ve geliştirme ihtiyacı oluşmaktadır. Geçmişte, laminat parke ürünlerinden beklenen özellikler, genleşme katsayılarının düşük olması, yüksek dayanım göstermesi, aşınma ve su direncinin yüksek olması vb. mekanik mukavemetlerini iyileştirmek iken, günümüzde bu özelliklere ek olarak antibakteriyel aktivitesinin yüksek olması, kolay temizlenebilir veya kendi kendini temizleme özelliğinin bulunması, yangına karşı yüksek direnç göstermesi, foto-kromik veya termo-krom yüzeye sahip olması, ses bariyeri özelliğinin bulunması vb. özellikler aranmaktadır. Yapılan araştırmalar; insanların zamanlarının %85'inden fazlasını kapalı alanlarda geçirdiğini dolayısıyla kapalı alanlarda kullanılan malzemelerin kalitesinin yaşam kalitesini yakından etkilediğini bildirmektedir. Ayrıca olası pandemi koşulları düşünüldüğünde kapalı alanlarda geçirilen zaman diliminin artması nedeniyle kendi kendine temizlenebilen ve antimikrobiyal aktivite gösteren yüzeylerin iç mekanlarda kullanımının hayati öneme sahip olduğu söylenebilir. Yapılan çalışma sonucunda görünür ışıkta kendi kendini temizleyebilen ve antimikrobiyal etki gösteren fonksiyonel yüzey çözeltileri elde edilmiştir. Bu amaç doğrultusunda sentezlenen nanopartiküllerin aktivasyon enerjisi, katkılama ile azaltılmış ve absorpsiyon spektrumu ışığın görünür bölgesine doğru kaydırılmıştır. Ortalama partikül boyutu 15±2 nm olan Sn ve Fe katkılı TiO₂ nanopartikül solları bir sol-jel yöntemi ile başarıyla sentezlenmiş ve absorpsiyon davranışları belirlenmiştir. Farklı asit türlerinin ve asit / başlatıcı mol oranının partikül boyutu üzerindeki etkileri araştırılmıştır. Sentezlenen soller yüksek yoğunluklu (HDF) melamin kaplı laminat parkeler gibi lignoselülozik endüstriyel malzemeler üzerine kaplama olarak uygulanmış ve kendi kendini temizleme özellikleri ve antimikrobiyal etkinlikleri değerlendirilmiştir. Katkılı TiO₂ nanopartikül kaplı yüzeylerin farklı kirletici türlerine karşı kendi kendini temizleme özellikleri Rodamin B boyasına karşı% 80,1, Metilen Mavisi boyaya karşı% 89,9 olduğu saptanmıştır. Kaplanmış laminat parke yüzeylerinin, E.coli bakteriyel yükünde %97, S. aureus için %87 azalma ile antibakteriyel etkinlik sağladığı görülmüştür.*

**Anahtar Kelimeler** / *Keywords: Katkılı TiO₂, Metal Oksit Nanopartiküller, Fotokatalitik Aktivite, Yüzey Kaplama Malzemesi, Kendi Kendini Temizleme, Antimikrobiyal Kaplama*

## I. GİRİŞ [INTRODUCTION]

Ahşap ve ahşap esaslı malzemeler, iç mekan dekorasyonuna sıcak ve samimi bir atmosfer sağladıkları için uzun yıllardır en çok kullanılan döşeme ürünleri olmaktadır. Bu ürünler arasında laminat parkeler, 1977 yılında piyasaya ilk girişlerinden bu yana en çok kullanılar arasındadır. Laminatlar genellikle, yüzeyi aşınmadan korumak için bir melamin-formaldehit reçinesi ile muamele edilmiş bir dekoratif ve bir kaplama tabakası ile sağlanan bir temel fiber levhadan (HDF, yüksek yoğunluklu ve MDF, orta yoğunluklu) yapılmaktadır. Bu tabakalar belirli bir süre ısı ve basınç ile birbirine kaynaştırılmaktadır [1].

Gelişen teknoloji nedeniyle mevcut malzemelerde sürekli olarak iyileştirme ve geliştirme ihtiyacı oluşmaktadır. Geçmişte, laminat parke ürünlerinden beklenen özellikler, genleşme katsayılarının düşük olması, daha iyi dayanıklılık göstermesi, aşınma ve su direncinin yüksek olası vb. mekanik mukavemetlerini iyileştirmek iken [2], günümüzde bu özelliklere ilave olarak anti-bakteri aktivitesinin yüksek olması, kolay temizlenebilir veya kendi kendini temizleme özelliğinin bulunması, yangına karşı yüksek direnç göstermesi, foto-kromik veya termo-krom yüzeye sahip olması, ses bariyeri özelliğinin bulunması vb. özellikler de aranmaktadır [3]. Bu fonksiyonel özellikler arasında kendi kendini temizleme özelliğine [4] ve antibakteriyel etkinliğe sahip olması [5] laminat parkelerin iç mekan kullanımı için oldukça önemlidir.
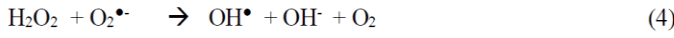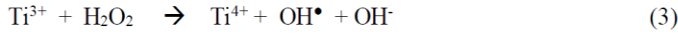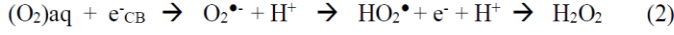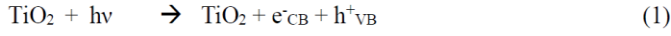
Enfeksiyon ve hastalığa neden olan zararlı mikroorganizmalar (norovirüsler, bakteriler vb.) sürekli olarak ortam havasında dolaşarak zeminde birikmektedir [6]. Suzuki vd. [7] sıradan bir ahşap esaslı laminat parkenin yüzeyinde 3,3 - 488 CFU / 10 cm$^2$ bakteri (CFU: koloni oluşturan birim) bulunduğunu ve bu kolonilerin yaklaşık %15'inin yüzeyde yürüme, fırçalama ve temizleme gibi mekanik etkiler ile havalanabildiğini belirtmektedir [8]. Bu sebeple zamanımızın çoğunu ev, çalışma ortamı, kafe ve restorantlar gibi kapalı ortamlarda geçirdiğimiz düşünüldüğünde (Meadow vd. ve Lax vd. insanların çoğunun zamanlarının %85'inden fazlasını kapalı alanlarda geçirdiğini saptamıştır) zemin kaplamada kullanılan mataryellerin niteliğinin oldukça önemli olduğu söylenebilir [9,10]. Günümüzdeki pandemi koşulları düşünüldüğünde kendiliğinden aktive gösterebilen yüzeylerin iç mekanlarda kullanımı hayati niteliktedir. Zeminde biriken mikroorganizmalar ve kirlilikler temizlik ürünleri ile de giderilmektedir. Fakat yüzeyleri temizlemek için kullanılan malzemeler uçucu organik bileşikler (VOC) olarak adlandırılan, ortamdaki hava kalitesini düşüren gazlar salmaktadır. Kapalı alanlarda temizlik amacıyla sıklıkla kullanılan malzemelerden salınan uçucu organik bileşikler; göz veya burunda tahriş, boğazda veya deride kuruluk, baş ağrısı ve yorgunluk gibi semptomlara neden olmaktadır [11]. Bu problem "Bina Kaynaklı Hasta Sendromu" olarak adlandırılmıştır ve esas olarak ortam havasındaki VOC'lerle ilgilidir. EPA'nın araştırmasında [12] rapor edildiği gibi VOC iç mekanda dış mekanda olduğundan on kata kadar daha yüksek konsantrasyonlarda sürekli olarak bulunmaktadır. Ayrıca yüzeylerde biriken kirleticileri uzaklaştırmak ve sterilizasyonu sağlamak amacıyla aralıklı olarak mekanik temizlik yapılması hem VOC salınımını daha da arttırmakta hem de sterilizasyonda süreklilik sağlayamamaktadır. Belirtilmesi gereken başka bir husus; zemin kaplama malzemelerinin yiyecek ve içecek kaynaklı organik kirleticiler ile kolaylıkla lekelenmesi ve bu lekelerin çıkatılması için yüzeylere yapılan mekanik temizlik nedeniyle yüzeylerde renk atmasının meydana gelmesidir. Bu durumda laminat parke yüzeylerini belirtilen bozulmalardan korumak için farklı tipte yüzey koruyucu cilalama maddeleri kullanılmaktadır. Bu cilalama maddeleri de genellikle kapalı alanlardaki ortam havasında VOC kirliliğine katkıda bulunan ve bu nedenle sağlık sorunlarına sebep olan çözücüler içermektedir [13]. Bu gibi etkiler düşünüldüğünde; çalışma ile elde edilen zemin yüzey kaplama ürününün kendiliğinden antimikrobiyal aktiviteye göstermesi ve kendi kendini temizleme özelliğinin bulunması ile VOC salınımına sebep olan malzemelerin kullanımının da azaltacaktır.

Bahsedilen bu sorunları çözmenin en kolay ve belki de en sağlıklı yolu; yüzeyde veya ortam havasında organik kirleticilerin bozulmasını sağlamak ve antimikrobiyal etki elde etmek için, fotokatalizör olarak yarı iletken oksit partiküllerini kullanmaktır. Bu tür fotokatalitik oksit parçacıkları da belirli bir dereceye kadar antibakteriyel aktivite göstermektedir. Bu tür yarı iletken oksit partiküllerine örnek olarak; $ZnO$, $SrTiO_3$, $CeO_2$, $WO_3$ ve $Fe_2O_3$ verilebilir. Bu materyaller arasında $TiO_2$'nin en popüleridir ve etkili olduğu kanıtlanmıştır. $TiO_2$ malzeme yüzeyinde bununan VOC'leri ve mikroorganizmaları, organik lekeleri tamamen parçalanmasında büyük performans göstermektedir. $TiO_2$ aynı zamanda fotostabildir, uzun vadeli etkiye sahiptir, toksik değildir, kolayca bulunur ve maliyeti düşüktür [14].

$TiO_2$'nin yüksek fotokatalitik aktivitesine rağmen, performansını artırmak için birçok strateji vardır. Bu stratejilerden biri $TiO_2$'nin Sn, Fe, Ni, Ce, N, Mg, Mn vb.

farklı elementlerle katkılanmasıdır [15, 16]. TiO$_2$ nanopartiküllerinin su/nem ile temas ettiğinde fotokatalitik reaksiyonları şu şekilde tanımlanabilir [17]:

$$TiO_2 + h\nu \rightarrow TiO_2 + e^-_{CB} + h^+_{VB} \qquad (1)$$

$$(O_2)aq + e^-_{CB} \rightarrow O_2^{\bullet-} + H^+ \rightarrow HO_2^\bullet + e^- + H^+ \rightarrow H_2O_2 \qquad (2)$$

$$Ti^{3+} + H_2O_2 \rightarrow Ti^{4+} + OH^\bullet + OH^- \qquad (3)$$

$$H_2O_2 + O_2^{\bullet-} \rightarrow OH^\bullet + OH^- + O_2 \qquad (4)$$

$$H_2O_2 + h\nu \rightarrow 2OH^\bullet \qquad (5)$$

$$O_s^{2-} + H^+_{aq} + h^+_{VB} \rightarrow OH_s^\bullet \qquad (6)$$

H$\nu$: UV ışıması
h$^+_{VB}$: valans-bant delikleri
e$^-_{CB}$: iletim-bant elektronları

TiO$_2$ nanopartikülleri UV ışığı altında partiküller su ile temas ettiğinde reaktif oksijen türlerinin (ROS) oluşumu nedeniyle antibakteriyel aktivite göstermektedir [18]. Antibakteriyel aktivitenin etki mekanizmasını aydınlatmak için çok sayıda çalışma yapılmış ve ROS'un bakteri hücre duvarına saldırdığı, böylece membran geçirgenliğinde değişikliklere yol açarak hücrenin ölümüne neden olduğunu saptanmıştır [19, 20].

Genel olarak bakıldığında TiO$_2$ içerikli laminat parke kaplaması; ortam hava kalitesini bozmadan, antibakteriyel aktivite ve kendi kendini temizleme özelliği gösteren ve yukarıda belirtilen sorunları önlemede kullanılabilecek mükemmel bir malzemedir. Bu nedenlerle bu çalışma, sol-jel yöntemi ile sentezlenen Sn ve Fe katkılı TiO$_2$'den oluşan, fotokatalitik, antibakteriyel etkili ve kolay temizlenebilir bir kaplama malzemesinin eldesi ve bu malzemenin kendi kendini temizleme özelliği, ortam iç havasını temizleme ve bir dereceye kadar antibakteriyel etki eldesi için lignoselülozik MDF ve HDF laminat parke malzemeleri üzerine uygulanmasını amaçlamaktadır.

## II. MATERYAL VE METOD [MATERIALS AND METHODS]

### A. *Malzemeler ve nanopartiküllerin sentezi*

Titanyum (IV) izopropoksit (%97 saf), etanol (absolute), hidroklorik asit (%37), nitrik asit (%65) ve metilen mavisi (susuz) Merck Millipore'dan satın alındı. Kalay (IV) klorür pentahidrat (%98), demir (III) nitrat nonahidrat (>%98) ve Rodamin B (>%97) Sigma-Aldrich'ten satın alındı.
Tüm deneyler, 9.4 MΩ/cm (6 ppm, TDS) dirençli bir BMB RO-30 ters ozmoz arıtma sisteminden (BMB Technology, TR) geçirilen saf su ile gerçekleştirilmiştir.

TiO$_2$ nanoparçacıklarının sol-jel sentezi, solvent bazlı ve su bazlı sistemler olmak üzere iki farklı aşamada gerçekleştirilmiştir. Solvent bazlı sistemler için, öncül Ti(OPr$_4$) absolute etanol içinde çözüldü, ardından SnCl$_4$.5H$_2$O ve Fe(NO$_3$)$_3$.9H$_2$O olarak katkı maddeleri ilave edildi ve 15 dakika karıştırıldı, ardından sırasıyla hidroklorik asit ve damıtılmış su eklendi. Reaksiyon, 90 ºC'de 16 saat süreyle gerçekleştirildi. Su bazlı sistemler için önce distile su ve nitrik asit karıştırılmış, ardından SnCl$_4$.5H$_2$O ve Fe(NO$_3$)$_3$.9H$_2$O olarak katkı maddeleri ve sabit karıştırma öncüsü altında Ti(OPr$_4$) damla damla eklenmiştir. Reaksiyon 80 ºC'de 16 saat sürdürüldü. Katkılanmanın TiO$_2$ nanopartiküller üzerindeki etkisini karşılaştırmak için su bazlı ve solvent bazlı sistemler için katkı maddesi eklenmeden aynı adımlar izlenerek referans çözeltiler hazırlanmıştır. Sistemlerin kimyasal bileşimleri ve katı oranları Tablo I'de gösterilmiştir.

**Tablo I.**
Solvent bazlı ve su bazlı TiO$_2$ nanoparçacık sentez sistemlerinin kimyasal bileşimleri ve katı oranları

**Solvent-bazlı TiO$_2$ nanopartikül seltez sistemi**

| Kullanılan Kimyasallar | Örnek İsmi | | |
|---|---|---|---|
| | **1** | **1Sn** | **1Fe** |
| Ti(OPr$_4$) (mol) | 0,035 | 0,035 | 0,035 |
| Ethanol (mol) | 0,069 | 0,069 | 0,069 |
| HCl (mol) | 0,016 | 0,016 | 0,016 |
| H$_2$O (mol) | 0,086 | 0,072 | 0,075 |
| SnCl$_4$.5H$_2$O (mol) | - | 0,002 | - |
| Fe(NO$_3$)$_3$.9H$_2$O (mol) | - | - | 0,002 |
| ağırlık% TiO$_2$ | 18,27 | 18,32 | 18,32 |
| mol H$_2$O /mol Ti | 2,5 | 2,1 | 2,2 |
| mol asit / mol Ti | 0,45 | 0,45 | 0,45 |

**Su-bazlı TiO$_2$ nanopartikül seltez sistemi**

| Kullanılan Kimyasallar | Örnek İsmi | | |
|---|---|---|---|
| | **2** | **2Sn** | **2Fe** |
| Ti(OPr$_4$) (mol) | 0,035 | 0,035 | 0,035 |
| PM (mol) | 0,136 | 0,136 | 0,136 |
| HNO$_3$ (mol) | 0,032 | 0,032 | 0,032 |
| H$_2$O (mol) | 2,532 | 2,532 | 2,532 |
| SnCl$_4$.5H$_2$O (mol) | - | 0,002 | - |
| Fe(NO$_3$)$_3$.9H$_2$O (mol) | - | - | 0,002 |
| ağırlık% TiO$_2$ | 4,01 | 4,01 | 4,01 |
| mol H$_2$O /mol Ti | 72,3 | 72,3 | 72,3 |
| mol asit / mol Ti | 0,91 | 0,91 | 0,91 |

## B. Karakterizasyon

Sentezlenen TiO$_2$ sollarının partikül boyutu analizleri, sıcaklık ve zamanın partikül büyümesi üzerindeki etkisini belirlemek için partikül ve molekül boyutu analizörü (Malvern Zetasizer Nano ZS) kullanılarak gerçekleştirilmiştir.

Ultraviyole-Görünür Spektrofotometre (Varian Carry 5000) katkılı ve katkısız TiO$_2$ sollarının absorpsiyon spektrumlarındaki kaymaları araştırmak için kullanıldı.

Tüm numunelerin kendi kendini temizleme özelliğini incelemek amacıyla boyalara (Rodamin B ve Metilen Mavisi, ISO 10678:2010 standardı) karşı fotokatalitik aktivite testleri bir ışık maruziyeti/güneş ışığı simülatörü test cihazı kullanılarak (Erichsen Solar- Ayarlanabilir (300 -800 nm, 1000 W/m2) xenon ışık kaynağı içeren Box 1500) yapıldı.

E.coli ve S.aureus'a karşı antibakteriyel etkinlik testleri, modifiye edilmiş ASTM-e2149-01 standardına karşı gerçekleştirildi.

## C. Kaplama çözümlerinin hazırlanması ve çözeltilerin laminat parke üzerine uygulanması

Kaplama çözeltileri hazırlamak için sentezlenen sollar öncelikle seyreltildi. Bu amaçla solvent bazlı TiO$_2$ solüsyonundan çökelen partiküller ayrılarak; 1-metoksi-2-propanol (PM), butil glikol (BG) ve etilen glikol (EG) ağırlık oranı sırayla 4: 2: 1 ve katı oranı %0,75 olacak şekilde seyreltildi. Su bazlı sistemlerde ise ağırlıkça %0,75 katı oranını eldesini sağlayacak kadar su ilavesi ile seyreltme işlemi yapıldı. Hazırlanan çözeltiler melamin-formaldehit emdirilmiş kağıda gravür yöntemiyle uygulandı. Daha sonra yüzeyinde fotokatalitik TiO$_2$ nanoparçacıkları bulunan bu emprenye edilmiş kağıt, taban HDF sunta üzerine 200 bar basınç ve 180 °C sıcaklıkta 15 saniye preslendi.

### III. BULGULAR [RESULTS]

## A. Partikül boyutu analizi

Sentezlenen TiO$_2$ sollarının partikül boyutu analizleri, toplam reaksiyon süresi boyunca partikül büyümesini izlemek için bir partikül ve molekül boyutu analizörü (Malvern Zetasizer Nano ZS) kullanılarak gerçekleştirilmiştir. Şekil 1'de 16 saatlik reaksiyon süresinden sonra ortalama parçacık boyutu 15 nm olan TiO$_2$ nanopartiküllerin zetasizer ölçümleri yer almaktadır.
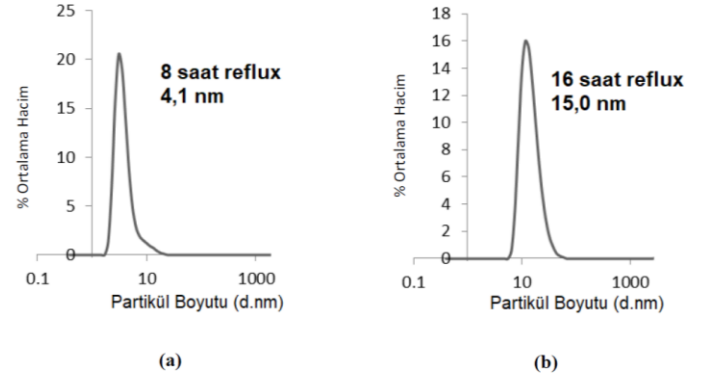


**Şekil. 1.** Reaksiyon süresi boyunca partikül boyutu büyümesi; (a) 92 °C reflux 8 saat, (b) 92 °C reflux 16 saat

## B. Sentezlenen TiO$_2$ nanoparçacıklarının UV-Vis spektroskopik analizi

Nanopartiküllerin absorpsiyon davranışını değerlendirmek için sentezlenen solların UV spektrumları analiz edildi. Şekil 2'de toplam absorpsiyon eğrisinin, artan % Sn/Fe katkılama miktarı ile dalga boyunun görünür ışık kısmına doğru kayması ve etkin absorpsiyon oranının artması görülmektedir. Katkılı TiO$_2$ parçacıkları sadece UV ışığı ile değil, aynı zamanda güneş ışığı, floresan ışık gibi görünür ışık kaynakları ile de aktive olmaktadır.
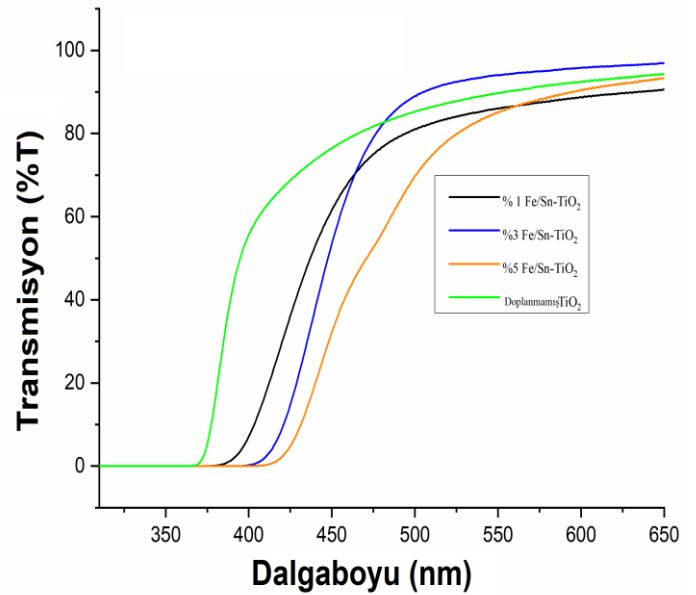


**Şekil. 2.** Sentezlenmiş TiO$_2$ sollarının UV-VİS spektrumları

*C. Nanoparçacık kaplı laminatların fotokatalitik aktivitesi*

Nanoparçacık kaplı yüzeylerin fotokatalitik aktiviteleri ve kendi kendini temizleme özellikleri, Rodamin B ve Metilen Mavisi boya çözeltilerine karşı değerlendirildi.

### i.   *Rodamin B boyasına karşı*

TiO$_2$ kaplamalı ve kaplamasız laminat parke numunesinin boyutları 10 x 10 cm olacak şekilde ayarlandıktan sonra 6 x 6 cm boşluklu bir aparata yerleştirildi. 25 ml 2 ppm Rodamin B boya solüsyonu distile su ile hazırlandı, aparat içerisine eklendi ve ultraviyole ve görünür ışık geçirgen cam lam ile kapatıldı. Örnekler, bir güneş simülatöründe (Erichsen Solar-Box 1500) 24 saat süreyle ışınlandı. Örneklerin görsel değişiklikleri Şekil 3'te verilmiştir. Rodamin B boya çözeltisinin konsantrasyonu Ultraviyole-Görünür Spektrofotometre (Varian Carry 5000) cihazı ile belirlendi.
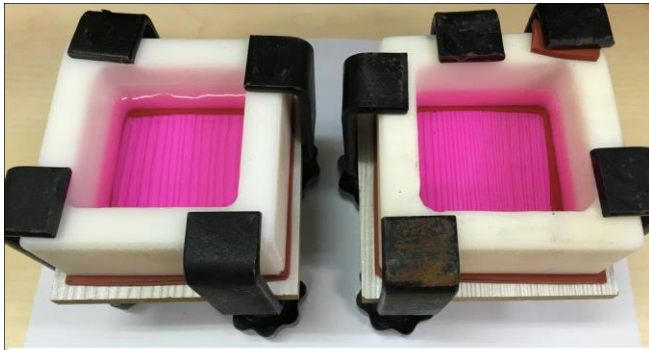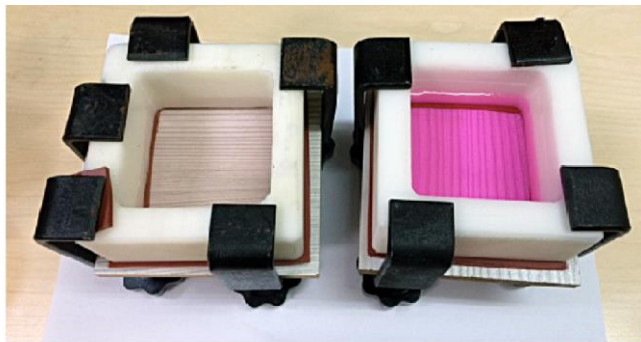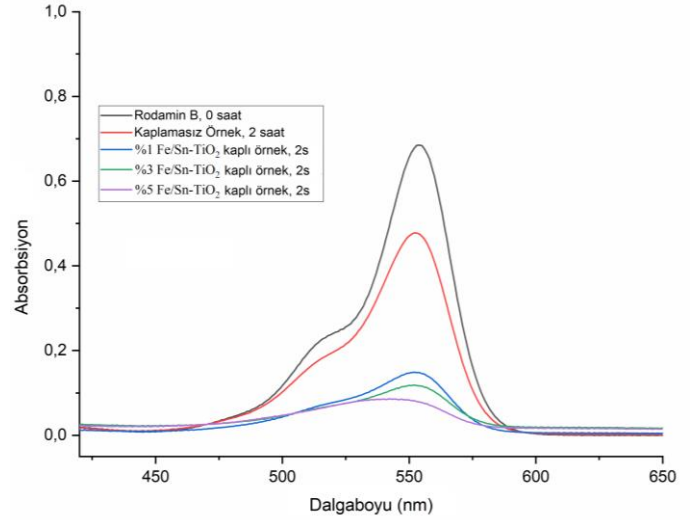


**Şekil. 3.** Rodamin B boya çözeltileri; ışınlamadan önce ((**a**)-sol) TiO$_2$ kaplı laminat numunesi, ((**a**)-sağ) kaplanmamış referans laminat numunesi ve 24 saat ışınlamadan sonra ((**b**)-sol) TiO$_2$ kaplı laminat numunesi, ((**b**)-sağ) kaplamasız referans laminat numunesi



**Şekil 4.** Rodamin B yapısının nanopartiküllere karşı bozunma hızının belirlenmesi için kullanılan absorbans grafiği

**Tablo II.**
Numunelerin Rodamin B boyasına karşı Solar-Box bozunma testi sonuçları

| Örnek İsmi | Rodamin B max. absorbsiyon | % Boya konsantrasyonunda azalma |
|---|---|---|
| 2 ppm Rodamin B stok çözeltisi | 0,685 | --- |
| Kaplanmamış Örnek | *0,477* | *-referans-* |
| %1 Fe/Sn-TiO$_2$ Kaplanmış Örnek | 0,148 | %68,9 |
| %3 Fe/Sn-TiO$_2$ Kaplanmış Örnek | 0,118 | %75,3 |
| %5 Fe/Sn-TiO$_2$ Kaplanmış Örnek | 0,095 | %80,1 |

Rodamin B boya çözeltisinin absorpsiyonun ölçümlerinde gözle görünür değişiklikler gözlemlenmiştir. Rodamin B boyası UV ışınlarına maruz kaldığında kademeli olarak bozunur ve bu durum Şekil 4'te kaplanmamış boş referans numunesinin absorpsiyon değişikliklerinde de görülmektedir. Bu durum boş referans numunede fotokatalitik etki gösteren Fe/Sn katkılı-TiO$_2$ nanopartikülleri ile kaplaması olmasada, Rodamin B boya çözeltisinin Solar-Box yaşlandırma testi işlemi kendi kendine bozunmasından kaynaklanır. Fakat kaplanmış numunelerin absorbans değerlerinde çok daha yüksek düşüş gözlemlenmektedir. Referans numune ile karşılaştırılan örneklerin performans sonuçları Tablo II'de verilmiştir.

Fe/Sn katkılı TiO$_2$ nanoparçacıklarından oluşan kaplamalı laminat parke numuneleri, standart numunelere göre Rodamin B kirleticisine karşı %80,1'e kadar daha hızlı yüzey temizleme etkisine sahip olduğu bulunmuştur.

### ii. Metilen Mavisi boyasına karşı

TiO$_2$ kaplamalı ve kaplamasız laminat parke numunesinin boyutları 10 x 10 cm olacak şekilde ayarlandıktan sonra 6 x 6 cm boşluklu bir aparata yerleştirildi. 25 ml 5 ppm Metilen Mavisi boya solüsyonu distile su ile hazırlandı, aparat içerisine eklendi ve ultraviyole ve görünür ışık geçiren cam lam ile kapatıldı. Örnekler, bir güneş simülatöründe (Erichsen Solar-Box 1500) 24 saat süreyle ışınlandı. Örneklerin görsel değişiklikleri Şekil 5'te verilmiştir.
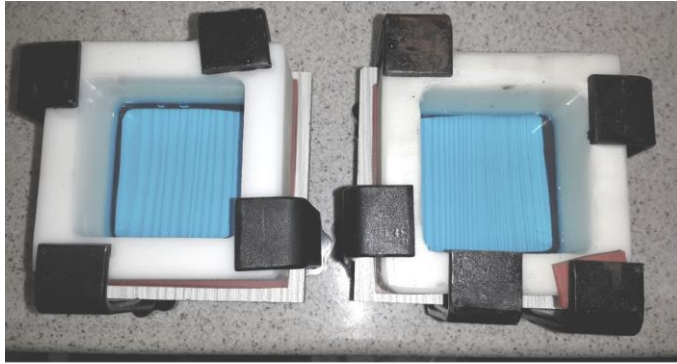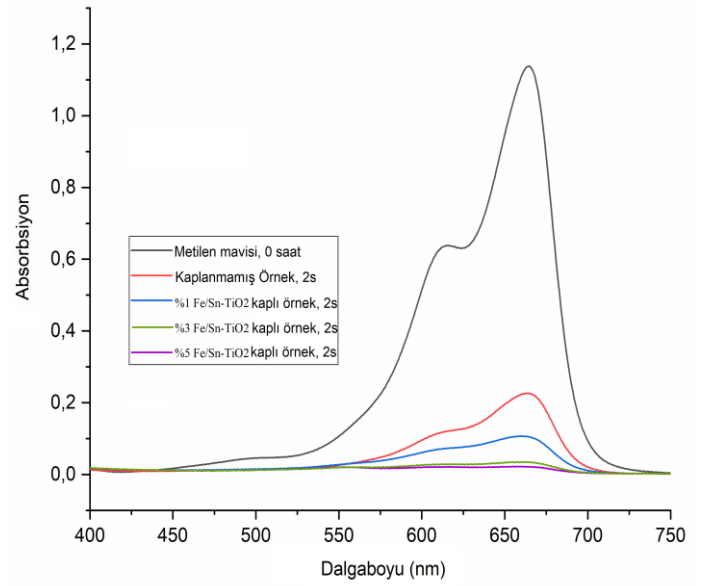


**(a)**
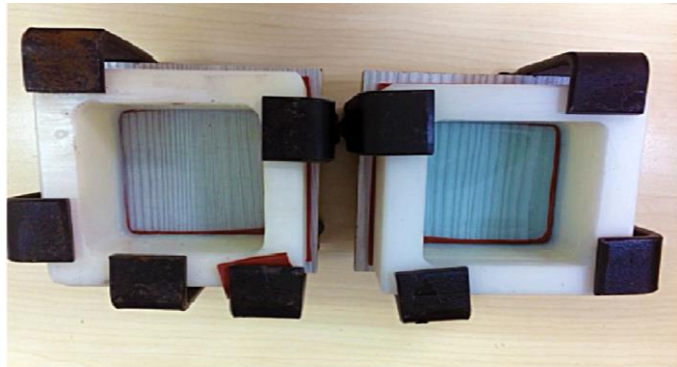


**(b)**

**Şekil. 5.** Metilen mavisi boya çözeltileri; ışınlamadan önce (**(a)**-sol) TiO$_2$ kaplı laminat numunesi, (**(a)**-sağ) kaplanmamış referans laminat numunesi ve 24 saat ışınlamadan sonra (**(b)**-sol) TiO$_2$ kaplı laminat numunesi, (**(b)**-sağ) kaplamasız referans laminat numunesi



**Şekil 6.** Metilen mavisi boyası yapısının nanopartiküllere karşı bozunma hızının belirlenmesi için kullanılan absorbans grafiği

Metilen Mavisi boyası UV ışınlarına maruz kaldığında Rodamin B boyasından daha hızlı bozunmaktadır. Fotokatalitik TiO$_2$ kaplı numuneler bozunma hızını hızlandırmış ve böylece kaplanmış numunelerin absorbansında önemli bir düşüş gözlemlenmiştir. Referans numune ile karşılaştırmalı performans sonuçları Tablo III'te verilmiştir. Fe/Sn katkılı TiO$_2$ nanoparçacıklarından oluşan kaplamalı laminat parke numuneleri, standart numunelere göre Metilen Mavisi kirleticisine karşı %89,9'a kadar daha hızlı yüzey temizleme etkisine sahiptir.

**Tablo III.**
Numunelerin Metilen Mavisi boyasına karşı Solar-Box bozunma testi sonuçları

| Örnek İsmi | Metilen mavisi max. absorbsiyon | % Boya konsantrasyonunda azalma |
|---|---|---|
| 5 ppm Metilen Mavisi stok çözeltisi | 1,137 | --- |
| Kaplanmamış Örnek | **0,227** | **-referans-** |
| %1 Fe/Sn-TiO$_2$ Kaplanmış Örnek | 0,108 | %52,4 |
| %3 Fe/Sn-TiO$_2$ Kaplanmış Örnek | 0,036 | %84,1 |
| %5 Fe/Sn-TiO$_2$ Kaplanmış Örnek | 0,023 | %89,9 |

*D. Nanopartikül kaplı laminat parkelerin antibakteriyel etkinliği*

Katkılı TiO₂ nanopartikül solları ile kaplanmış laminat parke yüzeylerinin antibakteriyel etkinlikleri modifiye edilmiş ASTM-e2149-01 standardı kullanılarak gram pozitif Staphylococcus aureus (ATCC 25923) ve gram negatif Escherichia coli (ATCC 11775) bakteri türlerine karşı değerlendirildi. Test için bakteri türlerinin Laktoz Broth (LB) besiyerinde bakteri popülasyonu büyüme eğrisi oluşturulmuş ve böylece büyüme hızları ve CFU/ml (mililitrede ortalama koloni sayısı) değerleri belirlenmiştir. Bakteri popülasyonunda maksimum artış elde etmek için optimum inkübasyon süresi bu büyüme eğrileri kullanılarak değerlendirilmiş ve *E.coli* için 5.30 saat ve *S.aureus* için 6.00 saat olarak belirlenmiştir. Bu süreye karşılık gelen uygun bakteri konsantrasyonları, $10^{-5}$'e seyreltilerek, katı besiyerindeki kültür ortamına bu seyreltilmiş çözeltiden 100 ul alınarak ekim işlemi yapılmıştır.

**Tablo IV.**
Kaplanmış ve kaplanmamış laminatların *E.coli* ve *S.aureus* bakterilerine karşı antibakteriyel etkinlik sonuçları

| *E.coli* bakterisine karşı yapılan analiz sonuçları | | | |
|---|---|---|---|
| | *E. coli* (koloni sayısı)* | | |
| Örnek | Işınlandırma Süresi 0 saat | Işınlandırma Süresi 1 saat | Işınlandırma Süresi 3 saat |
| TiO₂ Kaplı | 239 | 115 | 8 |
| Kaplamasız | 252 | 253 | 249 |
| Kontrol** | | 255 | |

| *S. aureus* bakterisine karşı yapılan analiz sonuçları | | | |
|---|---|---|---|
| | *S. aureus* (koloni sayısı)* | | |
| Örnek | Işınlandırma Süresi 0 saat | Işınlandırma Süresi 1 saat | Işınlandırma Süresi 3 saat |
| TiO₂ Kaplı | 204 | 177 | 27 |
| Kaplamasız | 211 | 209 | 210 |
| Kontrol** | | 212 | |

\* Bakteri kültürü ekili petri kaplarına yerleştirilen numuneler 1 saat bekletildikten sonra 37ºC'de 24 saat inkübasyona bırakıldı ve oluşan koloniler sayıldı.
\*\*Örnek bulundurmayan bakteri kültürü ekili petri kabı 37ºC'de 24 saat inkübasyona bırakıldı sonrasında oluşan koloniler sayıldı.

Belirlenen inkübasyon süresine göre TiO₂ kaplı ve kaplamasız referans numuneler eş zamanlı olarak hazırlandı. Örnekler otoklavda sterilize edildikten sonra iki gruba ayrıldı. Bir grup herhangi bir ışık kaynağına maruz bırakılmadan doğrudan kapalı bir kaba konuldu ve diğer grup 0, 1 ve 3 saat güneş ışığına maruz bırakıldı. Daha sonra numuneler 100 µl bakteri kültürü ile ekilen petri kabına 1 saat süreyle konuldu. Bekleme süresi dolduktan sonra numuneler çıkarıldı ve kontrol kör numuneleri ile birlikte 37 ºC'de 24 saat inkübe edildi. Periyot sonunda oluşan koloniler sayılarak örneklerin aktiviteleri belirlendi. Analizler üç tekrarlı olarak yapılmış ve sonuçların aritmetik ortalaması alınmıştır. Sonuçlar Tablo 5'te verildi. Analiz sonucunda petri kaplarında oluşan koloniler sayılarak örneklerin aktiviteleri belirlendi. Analizler üç tekrarlı olarak yapılmış ve sonuçların aritmetik ortalaması alınmıştır. Sonuçlar Tablo IV'te verilmiştir.

## IV. SONUÇ VE DEĞERLENDİRME [Conclusion]

Bu araştırma ile katkılı titanyum dioksit nanopartiküllerinin endüstriyel ölçekte kullanılabilen bir sentez yöntemi eldesini sağlamıştır. Çalışmada kendi kendini temizleme özelliğine sahip antibakteriyel etki gösteren laminat parke ürünlerinin üretimi amaçlanmıştır. Bu amaçla, aynı özelliklere sahip nanopartikül solları elde etmek için solvent bazlı ve su bazlı olmak üzere iki farklı sentez yöntemi kullanılmıştır. TiO₂ nanopartikülleri, katkısız TiO₂'nin absorpsiyon davranışını UV bölgesinden ışığın görünür bölgesine kaydırmak ve böylece çok daha iyi fotokatalitik aktivite elde etmek için Sn ve Fe elementlerinin bir kombinasyonu ile katkılanmıştır. Sonuç olarak, ~ 350 nm'de meydana gelen nanopartiküller tarafından ışık radyasyonunun tam absorpsiyonu ~ 430 nm'ye, ~ 390 nm'de meydana gelen% 50 absorpsiyon ~ 480 nm'ye kaymıştır. Katkılı TiO₂ nanopartikül kaplı yüzeylerin farklı kirletici türlerine karşı kendi kendini temizleme özellikleri Rodamin B boyasına karşı% 80,1, Metilen Mavisi boyaya karşı% 89,9 olduğu saptanmıştır. Kaplanmış laminat parke yüzeylerinin, *E.coli* bakteriyel yükünde% 97, *S. aureus* için % 87 azalma ile antibakteriyel etkinlik sağladığı görülmüştür.

***ÇIKAR ÇATIŞMASI** [CONFLICTS OF INTEREST]*

Yazarlar arasında ve ilgili kurumları arasında herhangi çıkar çatışması olmadığını bildirmişlerdir.

***ETİK KURALLARA UYGUNLUK** [RESEARCH AND PUBLICATION ETHICS]*

Yazarlar bu makalenin etik kurul onayı veya herhangi bir özel izin gerektirmediğini beyan ederler.

# KAYNAKLAR [REFERENCES]

[1]https://www.thespruce.com/what-is-laminate-flooring-1821619, last access: 04.03.2021

[2] NALFA Standards Publication LF 01-2003 Published by the North American LaminateFlooring Association © 2003. Product Standards - North American Laminate Floor Association, pp.1-27.

[3] L. Hu, S. Lyu, F. Fu, J. Huang and S. Wang. 2015. "Preparation and properties of multifunctional thermochromic energy-storage wood materials*," Journal of Materials Science,* vol.51, No.5 pp. 2716-2726. https://doi.org/10.1007/s10853-015-9585-9

[4] W. Yingke, L. Yiping, L. Juan, C. Liwei, H. Shilin, and T. Xuelin, 2020. "Fast self-healing superhydrophobic surfaces enabled by biomimetic wax regeneration" Chemical Engineering Journal, vol. 390, pages. 124311. https://doi.org/10.1016/j.cej.2020.124311

[5] C. Jia, Y. Zhang, J. Cui and L. Gan, 2019. "The Antibacterial Properties and Safety of a Nanoparticle-Coated Parquet Floor," *Coatings,* Vol.9, No.6 pp. 403. https://doi.org/10.3390/coatings9060403

[6] R.I. Adams, S. Bhangar, K.C. Dannemiller, J.A. Eisen, N. Fierer, J.A. Gilbert, 2016. "Ten questions concerning the microbiomes of buildings," *Building and Environment,* vol. 109, pp. 224-34.
https://doi.org/10.1016/j.buildenv.2016.09.001

[7] A. Suzuki, Y. Namba, M. Matsuura, A. Horisawa, 1984. "Bacterial contamination of floors and other surfaces in operating rooms: a five-year survey," *International Journal of Hygiene and Environmental Health, vol.* 93, pp. 559-66.
https://doi.org/10.1017/s002217240006513x

[8] W. Whyte, W.M. Whyte, S. Blake, G. Green, 2014. "Dispersion of microbes from floors when walking in ventilated rooms," *International Journal of Ventilation,* vol. 12, pp. 271-84.
https://doi.org/10.1080/14733315.2013.11684022

[9] J.F. Meadow, A.E. Altrichter, S.W. Kembel, J. Kline, G. Mhuireach, M. Moriyama, 2014. "Indoor airborne bacterial communities are influenced by ventilation, occupancy, and outdoor air source," *Indoor Air*, vol. 24, pp. 41-8.
https://doi.org/10.1111/ina.12047

[10] S. Lax, D.P. Smith, 2014. "Longitudinal analysis of microbial interaction between humans and the indoor environment," *Science*, vol. 345, pp. 1048-52. https://doi.org/10.1126/science.1254529

[11] J.A. Bernstein, N. Alexis, H. Bacchus, I.L. Bernstein, P. Fritz, E. Horner, N. Li, S. Mason, A. Nel, J. Oullette, K. Reijula, T. Reponen, J. Seltzer, A. Smith, S.M. Tarlo, 2008. "The health effects of nonindustrial indoor air pollution," *Journal of Allergy and Clinical Immunology,* Vol. 121, pp. 585-591. https://doi.org/10.1016/j.jaci.2007.10.045

[12] EPA's Office of Research and Development's "Total Exposure Assessment Methodology (TEAM) Study" (Volumes I through IV, completed in 1985).

[13] T. Ros-Dosdá, I. Celades, L., Vilalta, P. Fullana-i-Palmer and E. Monfort, 2019. "Environmental comparison of indoor floor coverings," *Science of The Total Environment,* vol.693, pages.
133519. https://doi.org/10.1016/j.scitotenv.2019.07.325

[14] L. Znaidi, R. Seraphimova, J.F. Bocquet, C. Colbeau-Justin, C. Pommier, 2001. "A semi-continuous process for the synthesis of nanosize $TiO_2$ powders and their use as photocatalysts," *Materials Research Bulletin*, vol. 36, no. 5-6, pp. 811-825. https://doi.org/10.1016/S0025-5408(00)00482-7

[15] R. Yuan, B. Zhou, D. Hua, C. Shi, L. Ma, 2014. "Effect of metal-ion doping on the characteristics and photocatalytic activity of $TiO_2$ nanotubes for the removal of toluene from water," *Water Science & Technology,* vol. 69, no.8 pp. 1697-1704.
https://doi.org/10.2166/wst.2014.071

[16] G. Yang, Z. Jiang, H. Shi, T. Xiao, Z. Yan, 2010. "Preparation of highly visible-light active N-doped $TiO_2$ photocatalyst," *Journal of Materials Chemistry,* vol. 20, pp. 5301-5309.
https://doi.org/10.1039/C0JM00376J

[17] J. Schneider, M. Matsuoka, M. Takeuchi, J. Zhang, Y. Horiuchi, M. Anpo, D.W. Bahnemann, 2014. "Understanding $TiO_2$ Photocatalysis: Mechanisms and Materials," *Chemical Reviews,* vol. 114, pp. 9919-9986.
https://doi.org/10.1021/cr5001892

[18] T. Matsunaga, R. Tomoda, T. Nakajima, H. Wake, 1985. "Photoelectrochemical sterilization of microbial cells by semiconductor powders," *Fems Microbiology Letters,* Vol 29, pp. 211-214. https://doi.org/10.1111/j.1574-6968.1985.tb00864.x

[19] A.K. Benabbou, Z. Derriche, C. Felix, P. Lejeune, C. Guillard, 2007. "Photocatalytic inactivation of Escherichia coli: Effect of concentration of $TiO_2$ and microorganism, nature and intensity of UV irradiation," *Applied Catalysis B: Environmental,* Vol 76, pp. 257-263. https://doi.org/10.1016/j.apcatb.2007.05.026

[20] S. Pigeot-Remy, F. Simonet, E. Errazuriz-Cerda, J.C. Lazzaroni, D. Atlan, C. Guillard, 2011. "Photocatalysis and disinfection of water: Identification of potential bacterial targets," *Applied Catalysis B: Environmental,* Vol 104, pp. 390-398 https://doi.org/10.1016/j.apcatb.2011.03.001

# El-Cezeri

Cizre'de dünyaya gelen Cezeri, ismini ise yaşadığı şehir olan Cizre'den almıştır.

Asıl adı *İsmail Ebul İz Bin Rezzaz* olarak bilinen mucit isim, El-Cezeri lakabıyla anılmaya başlanmıştır.

Cezeri, 1136 yılında Cizre'nin Tor mahallesinde doğmuştur. Sibernetik alanın kurucusu kabul edilen, fizikçi, robot ve matrix ustası bilim insanı "İsmail Ebul İz Bin Rezzaz El-Cezeri" 1206'te Cizre'de öldü. Lakabını yaşadığı şehirden alan El Cezeri, öğrenimini Camia Medresesi'nde tamamlayarak, fizik ve mekanik alanlarında yoğunlaştı ve pek çok ilke ve buluşa imza attı. Batı literatüründe M.Ö. 300 yıllarında Yunan matematikçi Archytas tarafından buharla çalışan bir güvercin yapılmış olduğu belirtilse de, robotikle ilgili bilinen en eski yazılı kayıt, Cezeri'ye âittir.

Dünya bilim tarihi açısından bugünkü sibernetik ve robot biliminde çalışmalar yapan ilk bilim insanı olan Cezeri'nin yaptığı otomatik makineler günümüz mekanik ve sibernetik bilimlerinin temel taşlarını oluşturmaktadır.

12. yüzyılın sonları ve 13. yüzyılın başlarında Diyarbakır ve Cizre'de yaşayan bilgin el-Cezeri, büyük miktarlarda suyu yukarı taşımak amacıyla beş düzenek tasarlamıştı. Bu düzeneklerden üçü hayvan gücüyle çalışırken ikisi kendi kendine işler, yani otomatiktir. El-Cezeri bu çalışmaları sırasında krank milini ilk kez kullanmıştı. Dönme hareketini doğrusal harekete dönüştüren krank mili, tarihteki en önemli keşiflerden biri olarak kabul ediliyor. El-Cezeri'nin su gücüyle çalışan pompa düzeneğinde dişli çarklar, bakır pistonlar, emme ve iletme amaçlı borular ve tek yönlü sürgülü vanalar kullanılıyordu. Bu düzenek suyu emerek yaklaşık on iki metre yukarı taşıyabiliyordu.

Cezerî, kitabında 50 aracın tasarımını vermiştir. Bu sebeple bu toprakların medar-ı iftiharlarından biri olmayı hak etmiştir. Bu araçların 6'sı su saati, 4'ü mumlu saat, 1'i kayık su saati, 6'sı ibrik, 7'si eğlence amaçlı kullanılan çeşitli otomatlar, 3'ü abdest almak için kullanılan otomat, 4'ü kan alma teknesi, 6'sı fıskiye, 4'ü kendinden ses çıkaran araç, 5'i suyu yukarı çıkartan araç, 2'si kilit, 1'i açı ölçerdir.

*Kaynak: https://www.hurriyet.com.tr/gundem/cezeri-kimdir-el-cezeri-ne-demek-41332282*